

Figure 2: A Google Earth image showing the location of the study area (in yellow) and the farm names (in white) (Google, 2007).

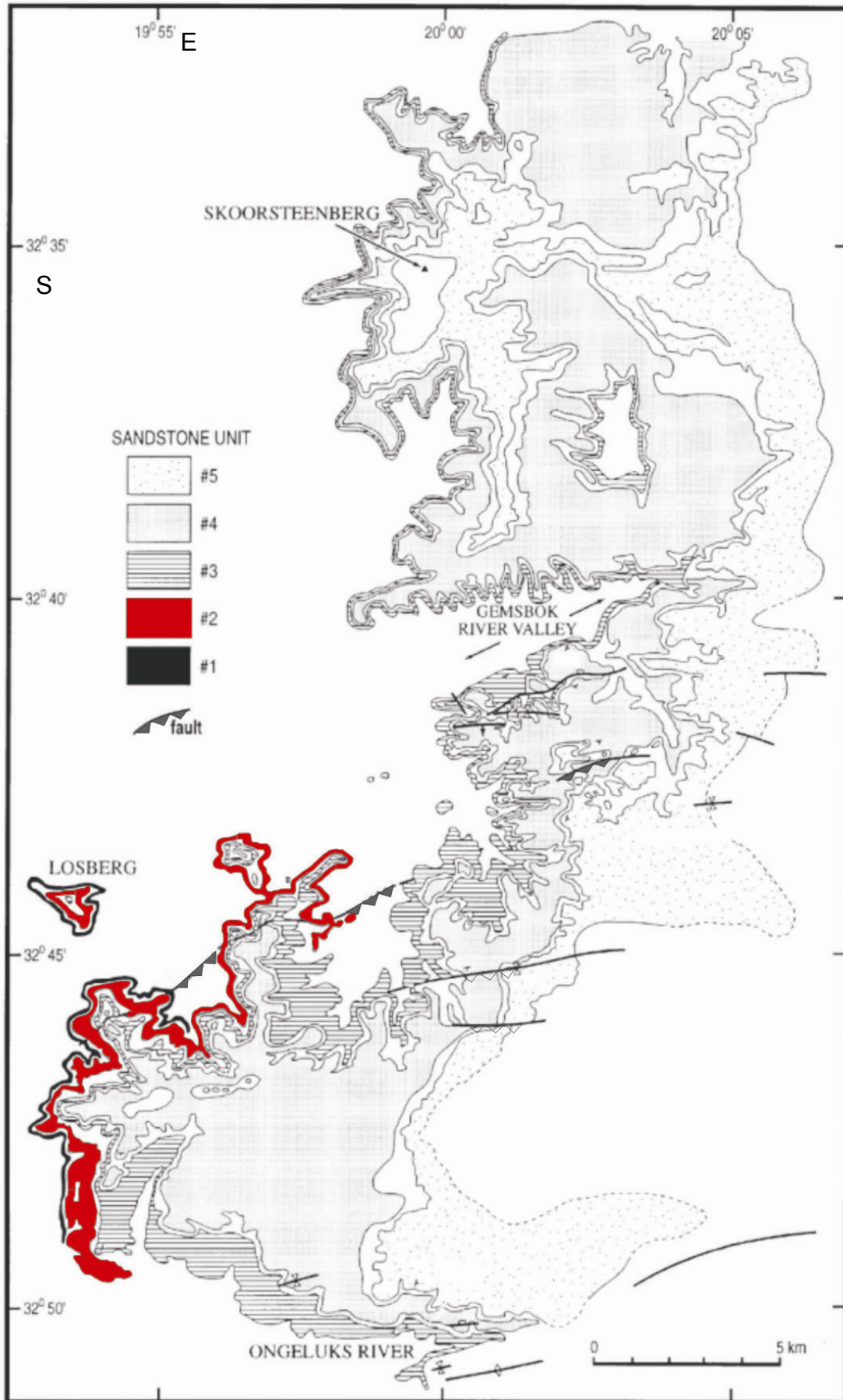


Figure 3: Geological map showing the outcrop distribution of Fans 1 to 5 in relation to each other. Fan 2 is indicated in red (after Wickens & Bouma, 2000).



formed due to accretion tectonics in the late Palaeozoic along Gondwana's southern border (De Wit & Ransome, 1992; Veevers *et al.*, 1994).

The Karoo Basin developed as a retroarc foreland basin with subsidence being the result of loading by the orogenic Cape Fold Belt (CFB) (Johnson, 1991; Visser, 1993; Veevers *et al.*, 1994; Hodgson *et al.*, 2006).

The CFB lies along the southern and south-western border of the Karoo Basin, forming the western Cedarberg branch and the southern Swartberg branch with the syntaxis in the Ceres-Worcester area (De Beer, 1990, 1992; Wickens, 1994; Sixsmith, 2000).

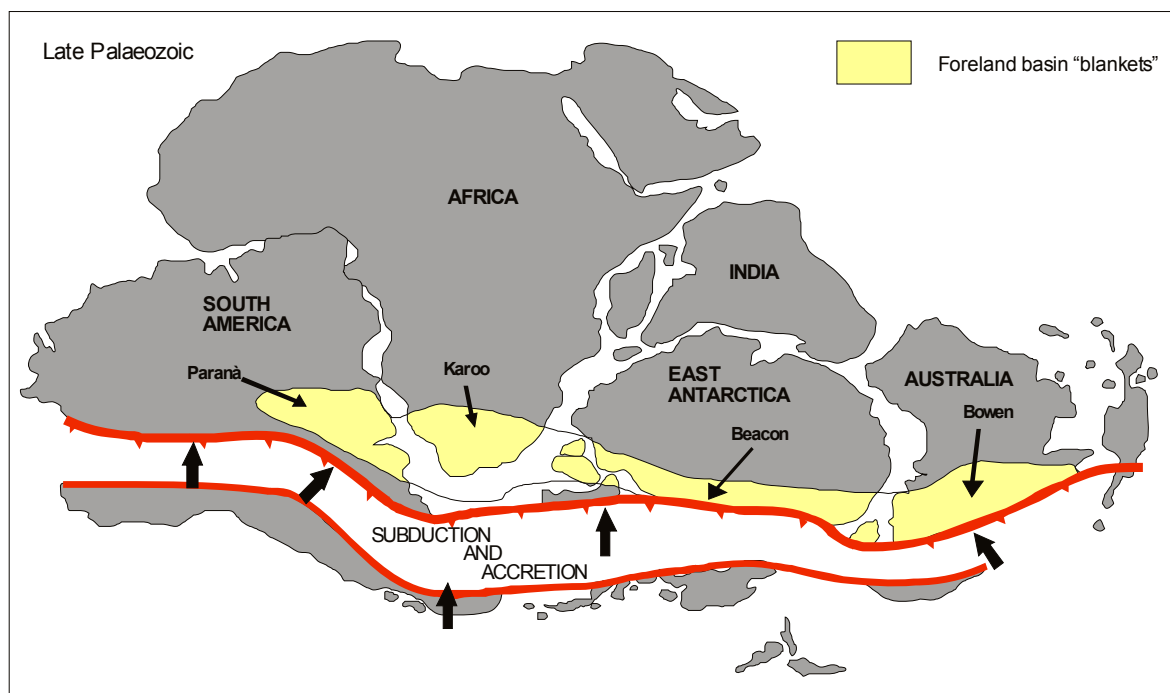


**Figure 8: Karoo, Paraná, Beacon and Bowen Basins in response to accretion tectonics along the southern margin of Gondwana (from De Wit & Ransome, 1992).**

The presence of the CFB along the margin of the Karoo Basin suggests that the basin was formed in an active-margin depositional setting. Despite this, the basin has many characteristics of passive-margin deposition, including an almost negligible amount of tectonic disturbance resulting in a dip of 2 to 4 degrees to the east (Wickens, 1994; Wickens & Bouma, 2000). The

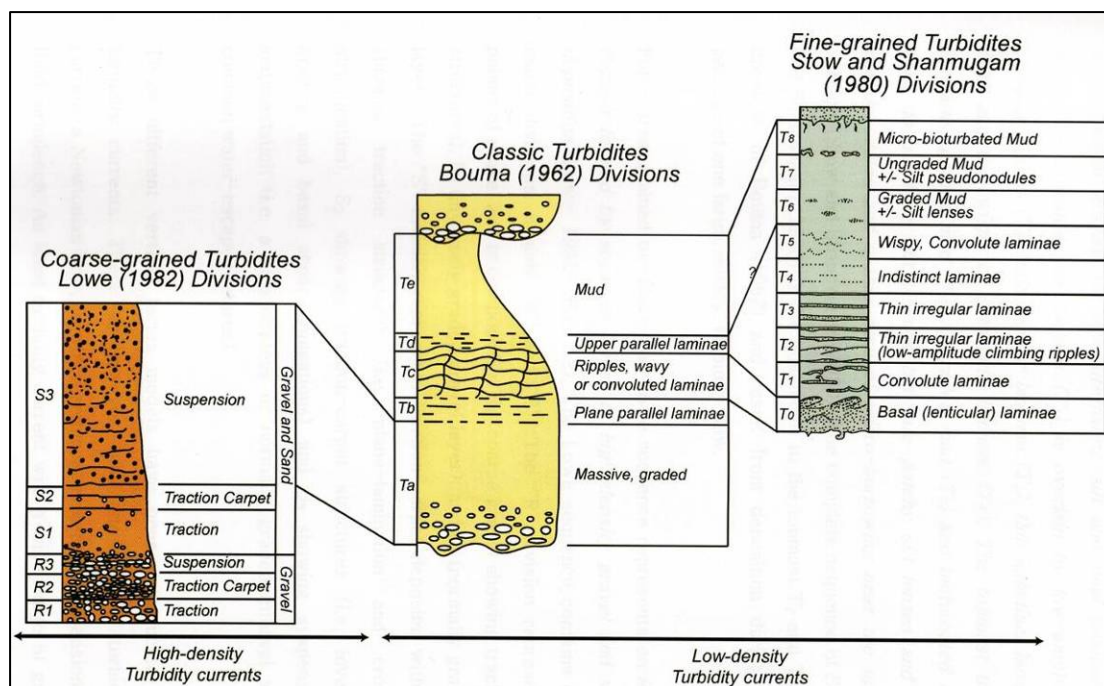


Figure 11: Turbidite divisions as proposed by Lowe, Bouma and Shanmugam (from Shanmugam, 2000).

### 2.1.1.5. Laboratory-generated turbidity currents

Turbidity current events in the natural world are rare, and attempts to monitor them usually result in a loss of equipment (Middleton, 1993). Studies using laboratory experimental results are coming progressively closer to imitating the formation of turbidite fans on a small, reproducible scale. One such study was conducted by Parsons *et al.* (2002) in a 5 x 5 x 1.2 m basin that was created at the Massachusetts Institute of Technology (MIT) Experimental Sedimentology and Geomorphology Laboratory.

The laboratory experiment was conducted on the premise that deep-sea fans differ from subaerial flows, due to the driving force behind the flow. Subaerial flows are driven only by gravitational acceleration, whereas turbidity flows are driven by a reduced gravitational acceleration (due to the effect of the densities of the current and ambient fluid) that is boosted by ignition feedback. Ignition feedback refers to a turbidity flow having the ability to entrain sediment. This increases the density of the turbidity flow, which in turn



order) and lobe complexes or fans (2<sup>nd</sup> order). Finally, fans stack to form fan complexes/turbidite complexes (1<sup>st</sup> order). Stacking patterns and element thickness are used in support of the suggested hierarchy.

Fan 2 is interpreted as a 2<sup>nd</sup> order lobe complex, with Middle Fan 2 classifying as a 3<sup>rd</sup> order lobe. Middle Fan 2 is subdivided into three 4<sup>th</sup> order lobe elements, each of which are further subdivided into 5<sup>th</sup> order bed sets and 6<sup>th</sup> order beds (Figure 21).

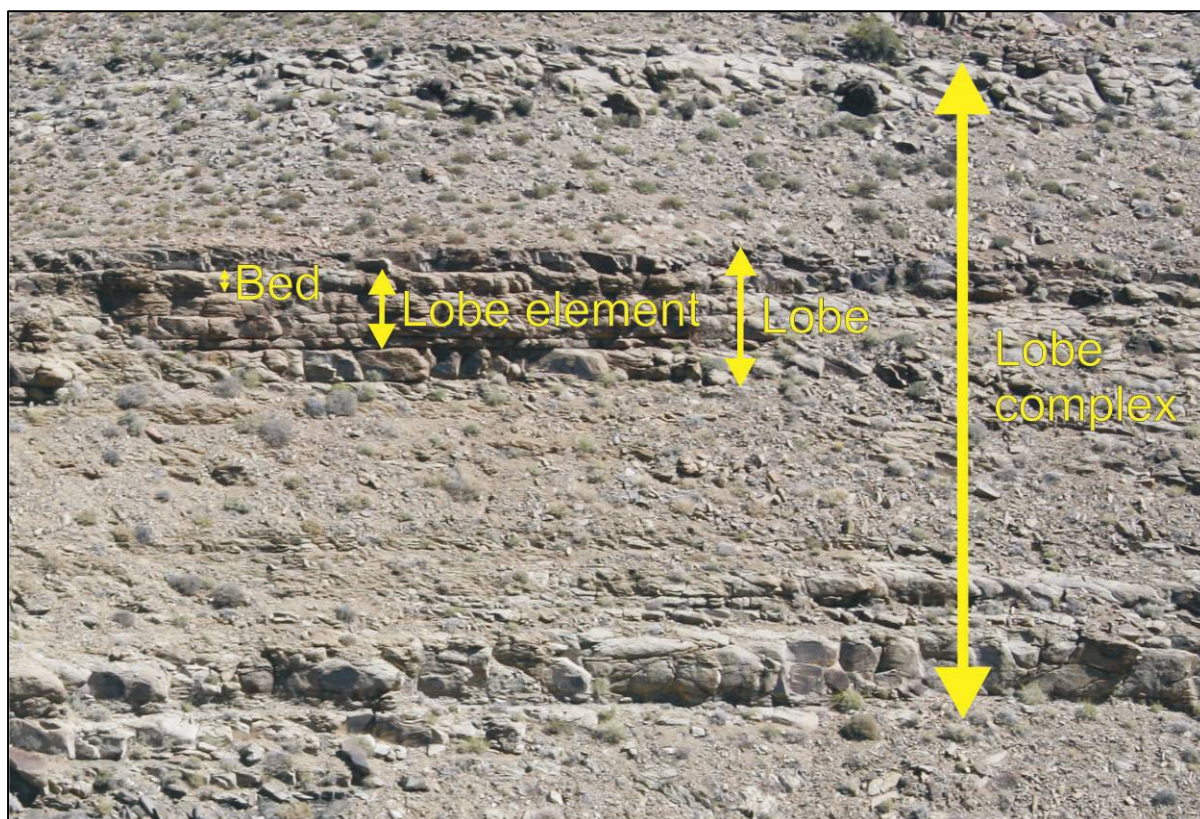


**Figure 21: Hierarchical interpretation of Fan 2 illustrating the lobe complex, lobe, lobe-element and bed (outcrop viewed towards the west; located on the farm Drie Fontein 87, near vertical profile R88, 34H0396579/UTM6367977).**

A comparison of the hierarchies used by Mutti & Normark (1987) and the LOBE project terminology as used by Pr lat *et al.* (in review) can be seen in Figure 22.

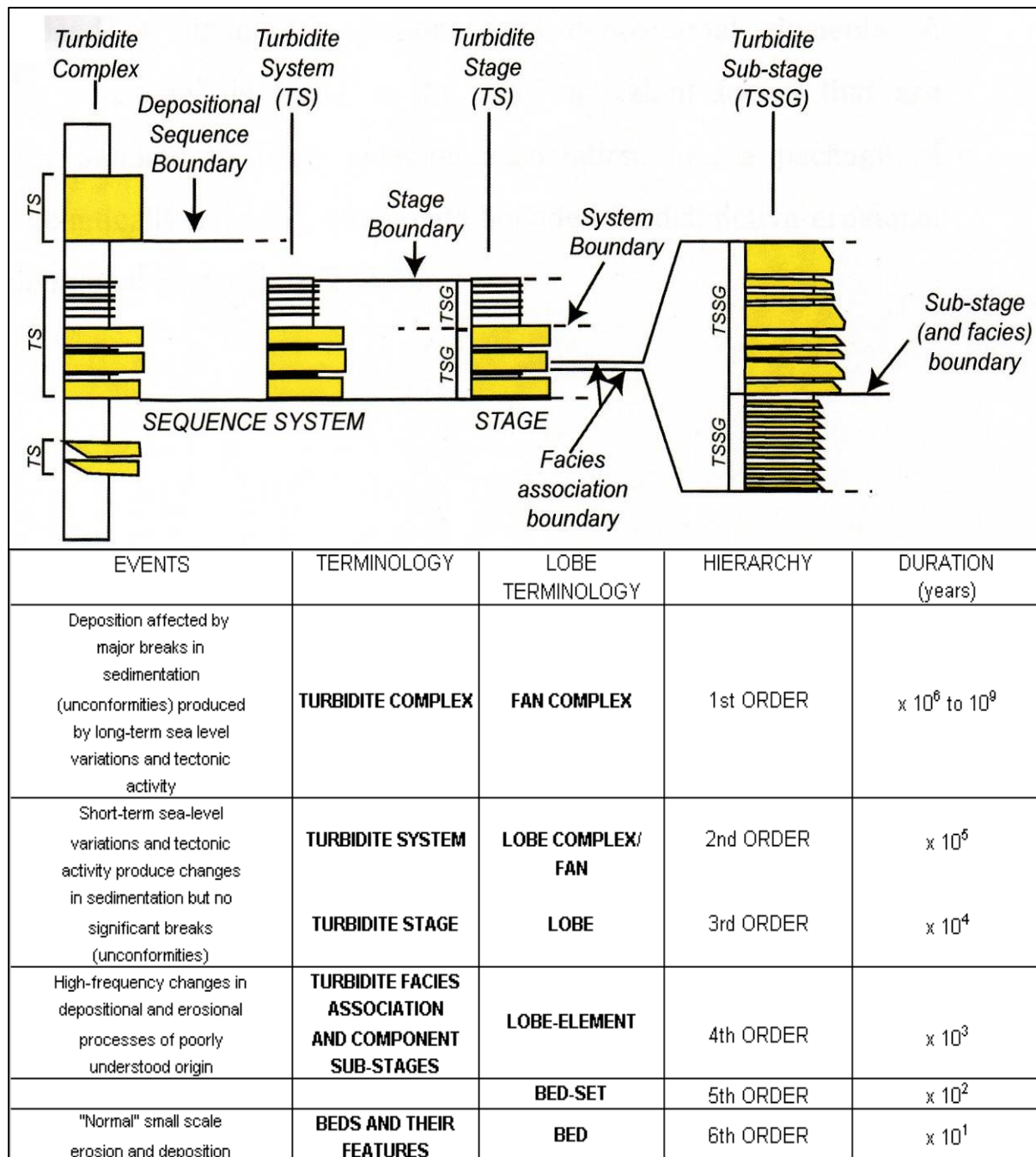


**Figure 22: Hierarchy for turbidite systems (modified after Mutti & Normark, 1987; Pr lat *et al.*, in review).**



Sole marks such as load- (Figure 23) and groove casts (Figure 24) can be found at the bases of several sandstone beds.

Fossilised plant-fragment imprints commonly occur on the top of sandstone beds (Figure 25). Calcareous concretions in the study area are red to dark brown and vary in size from 10 to 70 centimetres in diameter. They are found distributed in massive fine-grained sandstones (Figure 26).

Rip-up clasts (Figure 27) commonly occur in at the base of sandstone beds. They are also scattered in smaller groups or singly throughout the body of some sandstone beds. They vary in size from less than a centimetre in diameter to a maximum of 15 centimetres. Their shapes vary from rounded to angular.

Biogenic structures such as trace fossils are found as sole markings at the base of some of the massive sandstone beds (Figure 28).



**Figure 23: Load casts (arrow) at the base of a massive sandstone bed (1.2 m Jacob's staff for scale, vertical profile R13, 34H0398427/UTM6373891, on the farm Kleine Gemsbok Fontein 72).**





**Figure 24: Groove casts at the base of a massive sandstone bed (head of Jacob's staff for scale, vertical profile R42, 34H0397661/UTM6374647, on the farm Kleine Gemsbok Fontein 72).**



**Figure 25: A plant fragment imprint (arrow) encased in a massive sandstone bed (vertical profile R39, 34H0398211/UTM6374607, on the farm Kleine Gemsbok Fontein 72).**





**Figure 26: Secondary calcareous concretion (arrow) in a massive sandstone bed (vertical profile R01B, 34H0399413/UTM6373810, on the farm Klein Gemsbok Fontein 72).**

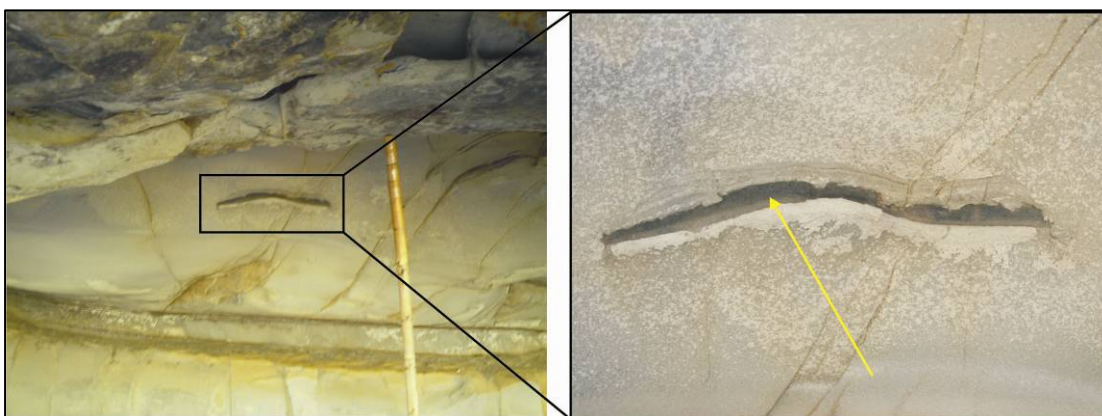


**Figure 27: A claystone rip-up clast (arrow) in a massive sandstone bed (1.2 m Jacob's staff for scale; vertical profile R00C, 34H0399356/UTM6373839, on the farm Klein Gemsbok Fontein 72).**

### **Interpretation**

Massive sandstone (Bouma-T<sub>a</sub> division) forms by rapid fallout from suspension of grains from high-density turbidity currents (Wickens, 1994; Baas, 2004). Amalgamation occurs when the upper fine-grained part of sandy

turbidites or thin siltstone layers are eroded away during deposition of the overlying layer (Stephen *et al.*, 2001).



**Figure 28: Casts of feeding burrows (arrows) in the pelitic top of the underlying turbidite (vertical profile R13, 34H0398427/UTM6373891, on the farm Kleine Gemsbok Fontein 72).**

This results in sand-on-sand contacts and seemingly continuous sandstone units of more than 6 metres thick. This facies is predominantly deposited in the upper flow regime and originates when high-density turbidity currents flow rapidly down a slope (Johnson *et al.*, 2001).

Flute casts are formed by current eddies, and groove casts by objects dragged in the hemipelagic mud prior to being filled in by sand (Boggs, 2006). Load casts are common at the bases of sandy turbidites and form when sand is deposited rapidly on top of a water-saturated mud layer. Differences in density cause loading of the higher-density sandstone, into the underlying lower-density, watery mud, forming irregularly-shaped protuberances (Boggs, 2006).



Rip-up clasts and plant fragments may be present. The very fine-grained sandstones often display a darker weathering pattern, due to a higher organic or rip-up clast content. An example of a sandstone displaying parallel-lamination can be seen in Figure 29, and a sandstone bed with ripple cross lamination along the top half of the sandstone can be seen in Figure 30.

Occasionally, sandstone beds show some indication of ripple cross- or parallel-lamination, but the laminations are not clearly defined in an individual bed. In this study, these beds are defined as structured sandstones to differentiate between it and massive sandstone. Gently deformed parallel-laminated layers that formed due to loading are visible in some of the structured sandstone layers (Figure 31).



**Figure 29: Parallel-laminated sandstone bed (arrow) (vertical profile R05B, 34H0399263/UTM6374071, Kleine Gemsbok Fontein 72).**

### **Interpretation**

Parallel- (Bouma-T<sub>b</sub> division) and ripple cross-lamination (Bouma-T<sub>c</sub> division) are the result of grains transported by traction and deposited grain-by-grain during fall-out from suspension from weakening turbidity currents (Wickens, 1994; Saito & Ito., 2002). Parallel-laminations are formed by

“upper-flow regime transport during turbidity current flow” (Boggs, 2001, p. 95). The initiation of parallel-laminations can be due to changes in the conditions of sedimentation. These changes include variations in grain size; organic, microfossil and clay content; and mineral composition (Boggs, 2006).

Ripple cross-laminations form due to traction as part of the planar bed phase of the lower-flow regime (Johnson *et al.*, 2001). Climbing ripples are produced when migrating ripples are superimposed on top of each other during very rapid deposition.



**Figure 30: Ripple cross-lamination (arrow) found in the upper half of a sandstone bed (vertical profile R13, 34H0398427/UTM6373891, on the farm Kleine Gemsbok Fontein 72).**

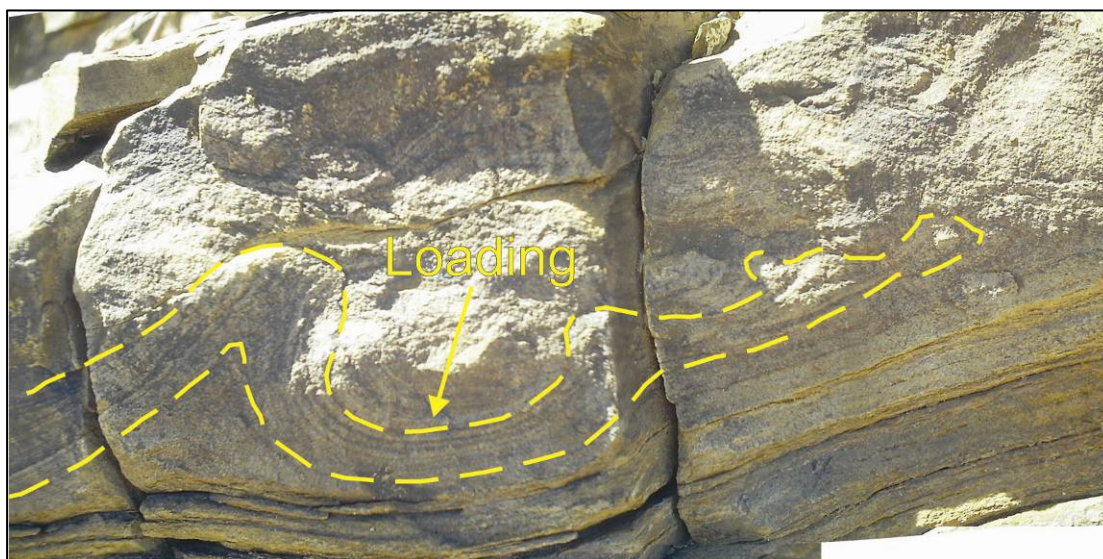


**Figure 31: Soft-sediment deformation due to loading in an area of parallel lamination (vertical profile R85, 34H0398427/UTM6373891, on the farm Kleine Riet Fontein 88).**



## Interpretation

Parallel- and ripple cross-lamination in siltstones form in a similar manner as those found in sandstones. Low-energy turbidity currents form traction structures as fine-silt grains fall out of suspension (Wickens, 1994; Saito & Ito, 2002). Changes in the flow regime (Boggs, 2006; Johnson *et al.*, 2001) and a decline in the fall-out rate translate into a change from parallel-lamination to ripple cross-lamination and can also affect the type of ripple that forms (Wickens, 1994).



**Figure 32: Alternating layers of 1) coarse-grained siltstone, 2) very fine-grained sandstone, 3) sand injection into underlying siltstone, and 4) massive fine-grained siltstone (vertical profile R00C, 34H0399356/UTM6373839, located on the farm Kleine Gemsbok Fontein 72).**





Figure 33: Parallel-laminated coarse-grained siltstone (vertical profile R05B, 34H0399263/UTM6374071, located on the farm Kleine Gemsbok Fontein 72).

### 3.5. Litofacies 5: Organic-rich co-genetic beds

#### Description

Co-genetic beds are composed of dark weathering, coarse “siltstones” with rip-up clasts and plant fragments chaotically distributed in the matrix, and an underlying massive sandstone. Black carbonaceous material and mica flakes are common. They occasionally display internal parallel-lamination (Figure 34). Carbonaceous material and mica flakes are commonly present. The beds are approximately 10 – 15 metres in length and commonly limited in extent, due to lateral pinching.

#### Interpretation

Debrites are the non-turbulent deposits from slow-moving laminar debris flows, and the flow is supported by a matrix. The debrites may be linked to underlying massive sandstone beds and are co-genetically deposited as

cohesive slurry associated with the top part of the turbidite sandstone bed. This is then termed a co-genetic bed (see Chapter 2.1.3 on co-genetic debrites) (Johnson *et al.*, 2001; Haughton *et al.*, 2003; Talling *et al.*, 2004).



**Figure 34: Co-genetic bed composed of underlying massive sandstone and an overlying dark-weathering organic-rich siltstone (arrow, 1.2 m Jacob's staff for scale; vertical profile R00A, 34H0399360/UTM6373789, located on the farm Kleine Gemsbok Fontein 72).**

### **3.6. Lithofacies 6: Massive claystone**

#### **Description**

Blue-weathering silt-rich claystone can be seen at the base and top of Middle Fan 2 in areas where it has not yet been weathered. The layers often display parallel-lamination and are very fine-grained (Figure 35).

#### **Interpretation**

Claystone is classified as shale that has a composition of more than two thirds clay particles that are smaller than 0.06 mm (Boggs, 2006). The claystone can be deposited in three ways. Pelagic settling involves "vertical settling under the influence of gravity" (Stow *et al.*, 2001, p. 491). Hemipelagic



deposition involves “vertical settling and slow lateral advection through the water column” (Stow *et al.*, 2001, p. 491). Hemiturbiditic sedimentation involves “upward dispersion from a dilute turbidity current ... mixes with any background pelagic or hemipelagic material and deposits slowly by vertical settling” (Stow *et al.*, 2001, p. 491). Each of these depositional processes occurs in a water depth of greater than 200 metres (Stow *et al.*, 2001). This facies makes up the interfan successions of the Skoorsteen Formation and represents periods of slow but continuous background deposition (Wickens, 1994; Johnson *et al.*, 2001).



**Figure 35: Blue-weathering silt-rich claystone (1.2 m Jacob's staff marked in 10 cm increments for scale; vertical profile R13, 34H0398427/UTM6373891, located on the farm Kleine Gemsbok Fontein 72).**



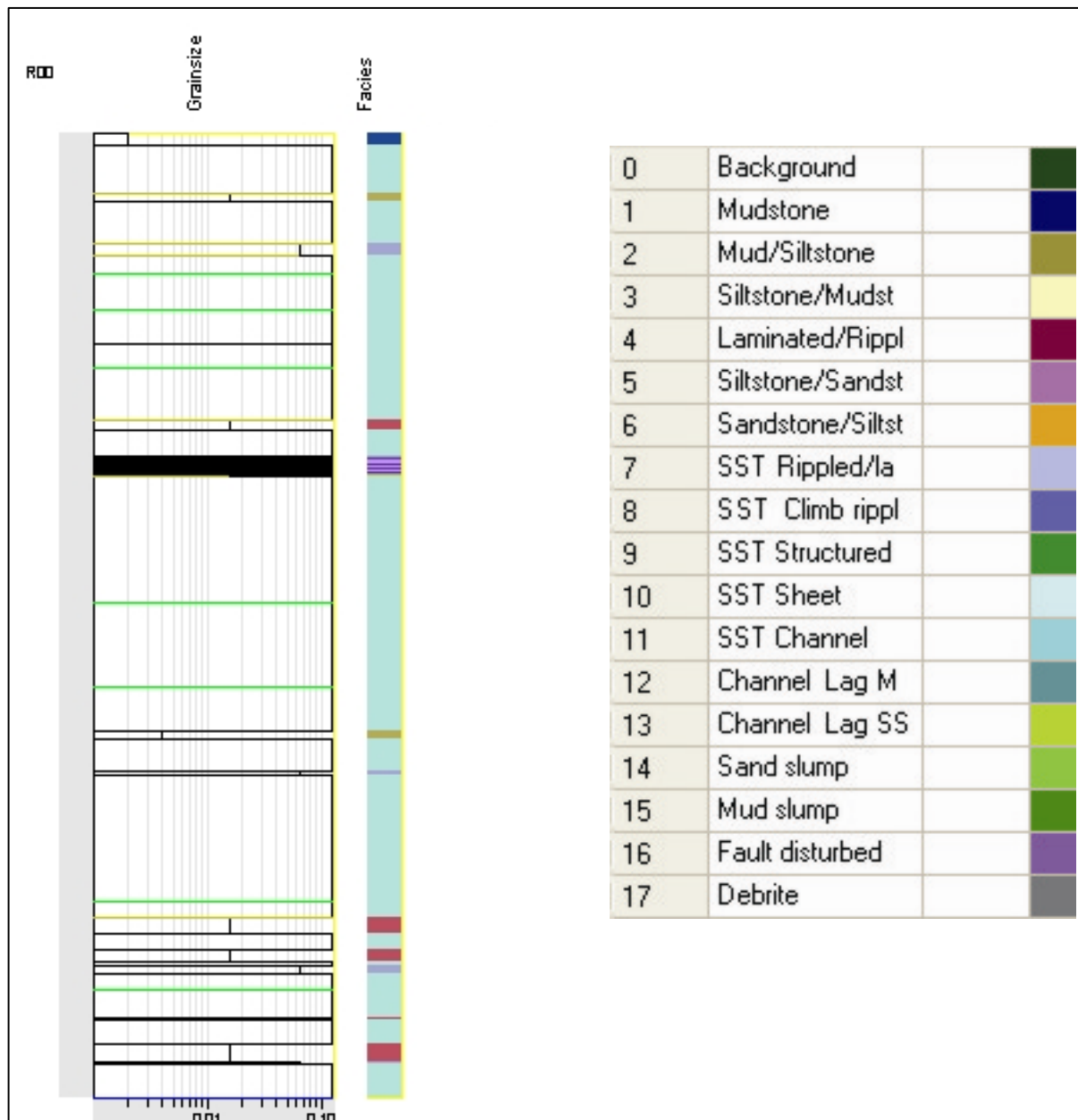


Figure 39: Vertical profile R00A (34H0399360/UTM6373789) compiled in DSL format showing the representation of facies used in the legend on the right.

A tabular representation of the different facies as used for the lithofacies descriptions in Chapter 3, and the DSL and Petrel facies in Chapter 0 can be seen in Figure 40. DSL colour codes the different facies and it is possible to choose the type of base (amalgamated, erosive, transitional, sharp, loaded and faulted) and grain size (very fine sand, fine sand, coarse silt, fine silt, clay and no exposure). The facies data were imported from DSL into Petrel,

allowing for the facies to be incorporated into correlation panels and modelled in 3-D.

Lithofacies description	DSL facies	Petrel facies
1) Massive sandstone	1) Structureless sandstone	1) Massive sandstone
2) Ripple cross- and parallel-laminated sandstone	2) Structured sandstone 3) Sandstone - ripples/planar lamination	2) Structure-bearing sandstone
3) Siltstone	4) Siltstone/sandstone (>50% silt)	3) Siltstone
4) Ripple cross- and parallel-laminated siltstone	5) Sandstone/siltstone (>50% sand) 6) Laminated/rippled siltstone	
5) Organic-rich co-genetic beds	7) Debrite (dominant sandstone with organics)	4) Other
6) Claystone	8) Mudstone 9) Mudstone/siltstone (>50% mud)	5) Background

Figure 40: Tabular representation of Virtual Reality Geological Studio (DSL) facies.

Petrel seismic-to-simulation software, Version 2007.1.2, is a 3-D modelling software package developed by Schlumberger. It was used to create surfaces, to construct isopach maps, to develop correlation panels, to build simple 3-D static model grids and to generate facies models using the digitised profile outcrop data. The Petrel help file was used extensively to describe the various algorithms and methods used for the modelling. Figure 41 shows wells that were generated using Petrel with the DSL input data on the left (a), the reduced Petrel facies in the middle (b), and the model-generated facies up-scaled into the grid on the right (c). DSL differentiates between 17 facies (d), of which 9 were used for this study. The facies were reduced to 4 for the purposes of up-scaling in Petrel (e). This is done in Petrel using the “calculator” and simple word equations.

### 4.3.2. Aims

The primary concern, when considering the use of Petrel, was whether the detailed scale used during the measuring of the vertical profiles in outcrop could be effectively imported and modelled in Petrel. This is directly influenced by the processing power of the available computers used to run the Petrel program. Thus, a key aim of this work was to obtain insight into the using of Petrel. Once the efficacy of the data was determined, the primary aim for using Petrel was to build a 3-D model of lobe-element distribution. It was used to represent the outcrop in an attempt to illustrate the internal variation in the



Middle Fan 2 lobe, including variation in facies. It was also useful in visualising the depositional model (Chapter 7).

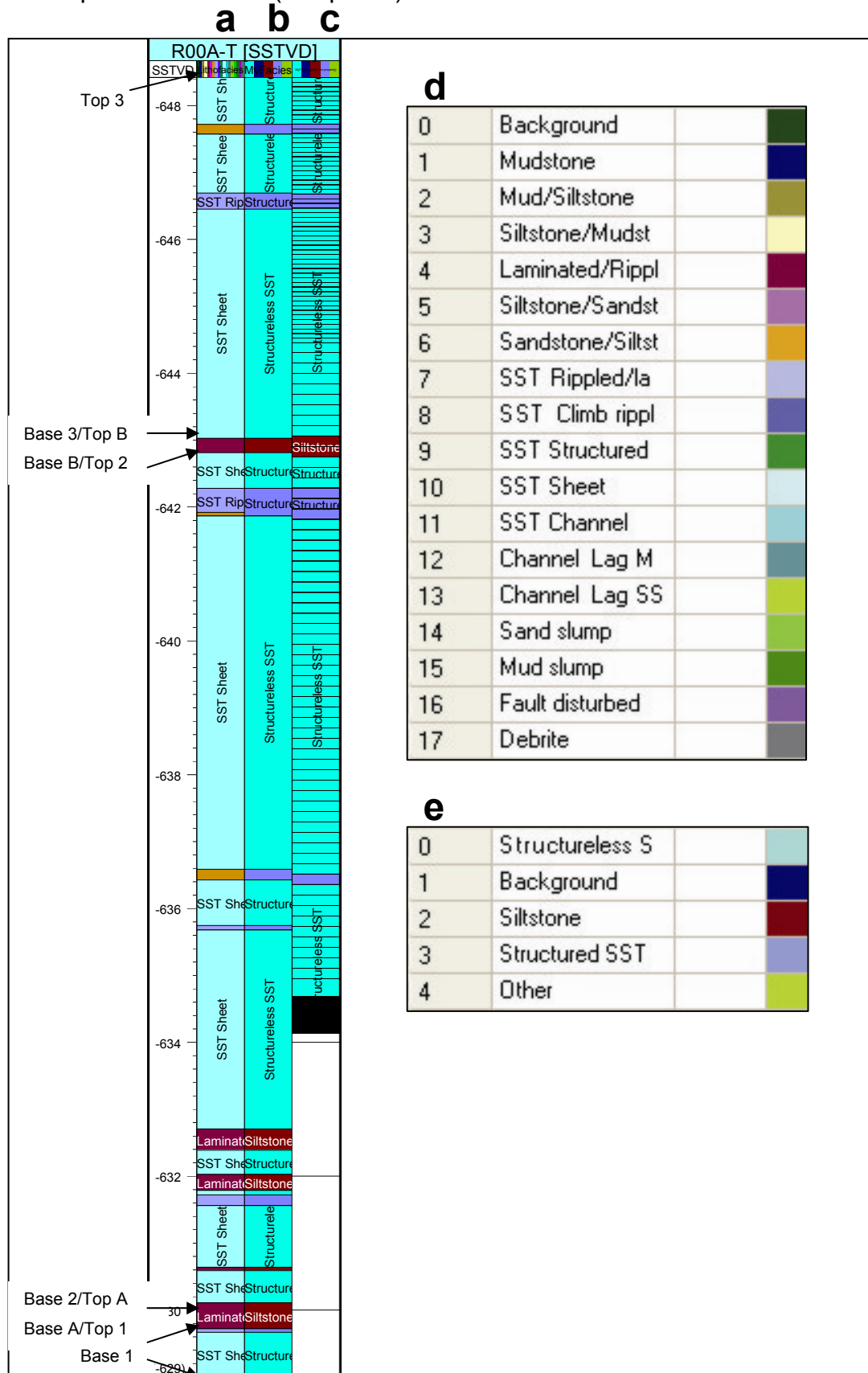


Figure 41: Petrel-generated image of profile R00A (34H0399360/UTM6373789) showing the DSL input data (a), Petrel facies (b), the model-generated facies up-scaled into the grid (c), the DSL facies legend (d) and the Petrel facies legend (e).

### 4.3.3. Model size

Analogue data collected in the field for the 12000 x 7000 x 25 metre study area were imported into Petrel in the form of 91 DSL profiles, GPS coordinates, and thickness-calculations of the various lobes and lobe elements to give as accurate a depiction of the internal structure of Middle Fan 2 as possible. Each of the profiles are seen as “wells” in Petrel and they are oriented according to their top X, Y and Z GPS coordinates to allow for some indication of the topography of the study area. As most of the profiles were measured in the backs of gullies the base GPS coordinates (Z) were commonly too inaccurate to be useful, thus the base GPS was calculated using the top GPS and the measured thickness of the profiles. The margin of error of the Z-readings varied from 0.5 m at the top to 33 m at the base of vertical profiles. The study area was constrained to the region surrounding the measured profiles using a broader polygon (A, ~1000 metres from data points) for the first two static model grids and a narrower polygon (B, ~400 metres from data points) for the third static model grid. The polygon size was reduced in order to minimise the amount of extrapolation by Petrel where no data points are available. Despite this, there were still some anomalous results in areas more than 100 metres from the nearest profile. The location of the vertical profile data points and the two polygons can be seen in Figure 42.

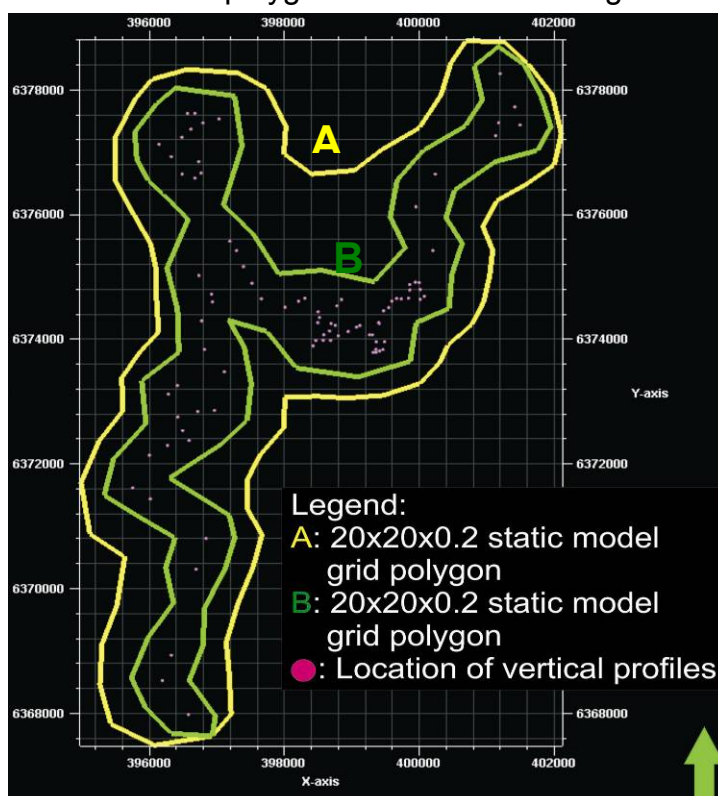


Figure 42: Location of data points (pink dots) and polygons A (yellow) and B (green).



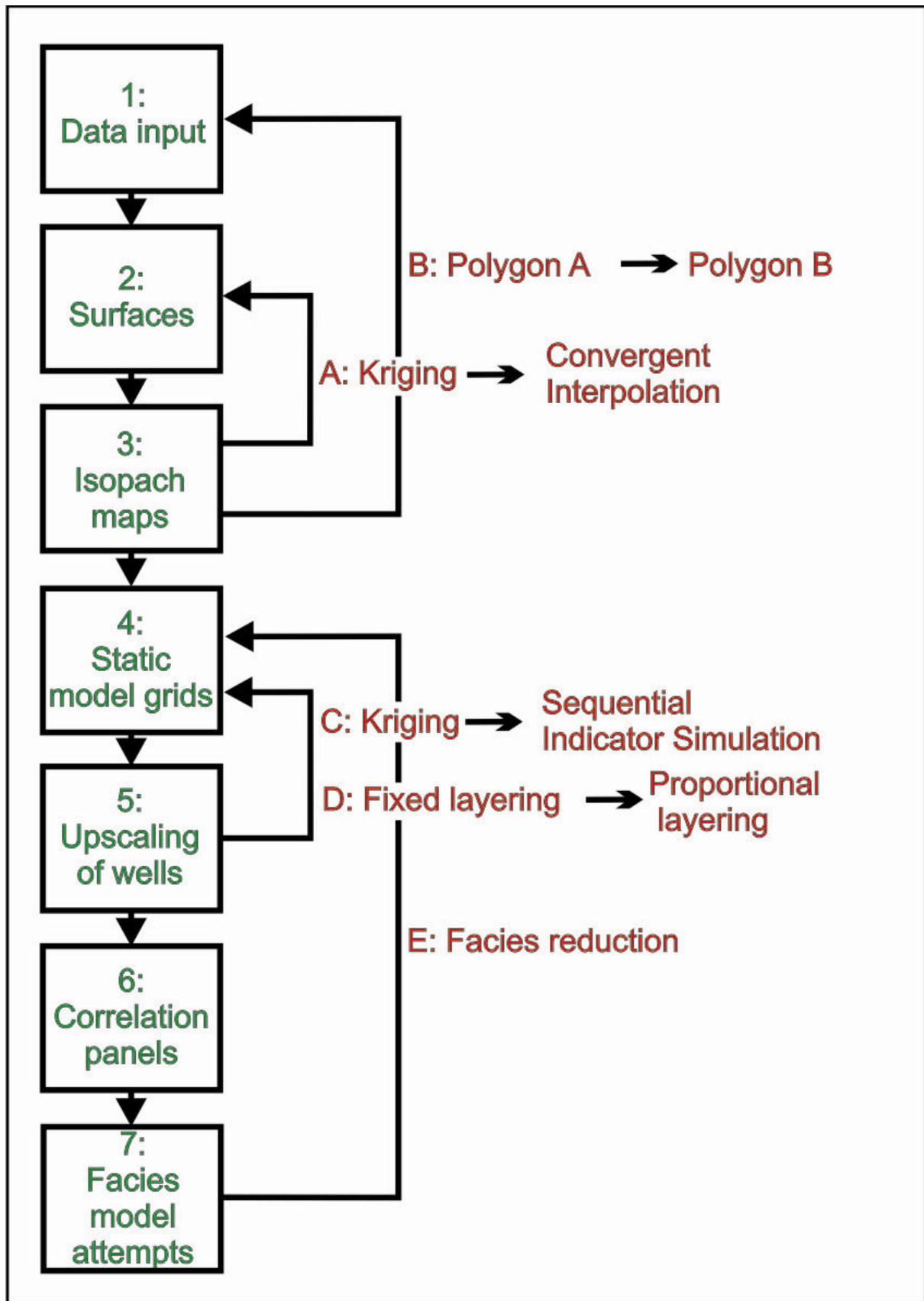


Figure 43: Petrel workflow diagram.

	R00A			
Surfaces	X	Y	Z	
Top 3	-32.7692	19.92548	649	<b>Rochelle Steyn:</b> Top measured GPS coordinates
	0.7			
	0.1			
	0.02			
	0.6			
	0.17			
	0.28			
	0.53			
	0.5			
	0.34			
	0.76			
Base 3/Top B	<b>0.15</b>	4	645	<b>Rochelle Steyn:</b> Measured thickness (m) of sandstone lobe element
Base B/Top 2	0.38	0.15	644.85	
	0.25			
	0.1			
	0.4			
	1.85			
	1.22			
	0.65			
	0.11			
	0.48			
	0.05			
	1.85			
	0.24			
	0.23			
	0.25			
	0.17			
	0.05			
	0.11			
	0.25			
	0.4			
	0.04			
Base 2/Top A	0.34	9.42	635.43	<b>Rochelle Steyn:</b> Calculated GPS Z coordinate for surface Base 2/Top A
Base A/Top 1	<b>0.27</b>	0.27	635.16	<b>Rochelle Steyn:</b> Bottom calculated GPS coordinate
	0.04			
	0.47	0.51	634.65	
Base 1				

Figure 44: Thickness and GPS coordinate data (m) for measured vertical profile R00A (34H0399360/UTM6373789).



	X	Y	Z	Z - Thickness	Base 3/Top B	Thickness	Z - Thickness	Base B/Top 2	Thickness	Z - Thickness	Base 2/Top A	Thickness
R00A-T	399360	6373789	649	645	Base 3/Top B	4	644.85	Base B/Top 2	0.15	635.43	Base 2/Top A	9.42
R00B-T	399319	6373788	646	641.38	Base 3/Top B	4.62	641.31	Base B/Top 2	0.07	633.19	Base 2/Top A	8.12
R00C-T	399356	6373839	663	658.42	Base 3/Top B	4.58	658.04	Base B/Top 2	0.38	649.62	Base 2/Top A	8.42
R01A-T	399461	6373834	641	637.26	Base 3/Top B	3.74	636.55	Base B/Top 2	0.71	629.59	Base 2/Top A	6.96
R01B-T	399413	6373810	643	637.95	Base 3/Top B	5.05	637.63	Base B/Top 2	0.32	629.81	Base 2/Top A	7.82
R02-T	399363	6373957	645	640.62	Base 3/Top B	4.38	639.97	Base B/Top 2	0.65	632.26	Base 2/Top A	7.71
R03-T	399485	6373960	645	639.68	Base 3/Top B	5.32	639.21	Base B/Top 2	0.47	636.11	Base 2/Top A	3.1
R04-T	399406	6374250	665	659.16	Base 3/Top B	5.84	658.56	Base B/Top 2	0.6	655.23	Base 2/Top A	3.33
R05A-T	399305	6374070	656	651.69	Base 3/Top B	4.31	651.16	Base B/Top 2	0.53	643.33	Base 2/Top A	7.83
R05B-T	399263	6374071	649	643.78	Base 3/Top B	5.22	643.7	Base B/Top 2	0.08	637.98	Base 2/Top A	5.72
R06-T	399398	6374267	671	665.18	Base 3/Top B	5.82	665.16	Base B/Top 2	0.02	661.01	Base 2/Top A	4.15
R07-T	399120	6374219	656	649.38	Base 3/Top B	6.62	649.2	Base B/Top 2	0.18	644.24	Base 2/Top A	4.96
R08-T	399071	6374194	668	661.56	Base 3/Top B	6.44	661.52	Base B/Top 2	0.04	657.07	Base 2/Top A	4.45
R09-T	398945	6374123	660	653.4	Base 3/Top B	6.6	653.34	Base B/Top 2	0.06	650.24	Base 2/Top A	3.1
R10-T	398799	6374055	663	656.84	Base 3/Top B	6.16	656.77	Base B/Top 2	0.07	653.88	Base 2/Top A	2.89
R11-T	398687	6373980	665	658.66	Base 3/Top B	6.34	658.58	Base B/Top 2	0.08	655.79	Base 2/Top A	2.79
R12-T	398577	6373981	667	661.53	Base 3/Top B	5.47	661.49	Base B/Top 2	0.04	658.51	Base 2/Top A	2.98
R13-T	398427	6373891	675	669.51	Base 3/Top B	5.49	669.47	Base B/Top 2	0.04	665.68	Base 2/Top A	3.79
R14-T	398468	6373977	673	667.695	Base 3/Top B	5.305	667.675	Base B/Top 2	0.02	662.395	Base 2/Top A	5.28
R15-T	398587	6374072	666	660.26	Base 3/Top B	5.74	660.22	Base B/Top 2	0.04	657.04	Base 2/Top A	3.18
R16-T	398670	6374131	658	651.32	Base 3/Top B	6.68	651.28	Base B/Top 2	0.04	648.43	Base 2/Top A	2.85
R17-T	398755	6374221	667	662.53	Base 3/Top B	4.47	662.49	Base B/Top 2	0.04	660	Base 2/Top A	2.49
R18-T	398692	6374249	662	658.48	Base 3/Top B	3.52	658.36	Base B/Top 2	0.12	655.79	Base 2/Top A	2.57
R19-T	398497	6374265	666	660.74	Base 3/Top B	5.26	660.69	Base B/Top 2	0.05	656.82	Base 2/Top A	3.87
R20-T	398521	6374348	669	664.6	Base 3/Top B	4.4	664.56	Base B/Top 2	0.04	659.79	Base 2/Top A	4.77
R21-T	398500	6374440	670	665.28	Base 3/Top B	4.72	665.21	Base B/Top 2	0.07	661.24	Base 2/Top A	3.97
R22-T	398780	6374535	680	675.26	Base 3/Top B	4.74	675.16	Base B/Top 2	0.1	671.23	Base 2/Top A	3.93
R23-T	398846	6374635	669	664.49	Base 3/Top B	4.51	664.43	Base B/Top 2	0.06	660.34	Base 2/Top A	4.09
R24-T	399472	6374454	660	654.61	Base 3/Top B	5.39	654.49	Base B/Top 2	0.12	650.15	Base 2/Top A	4.34
R25-T	399547	6374507	657	652.28	Base 3/Top B	4.72	651.99	Base B/Top 2	0.29	647.54	Base 2/Top A	4.45
R26-T	399593	6374607	653	647.87	Base 3/Top B	5.13	647.79	Base B/Top 2	0.08	643.99	Base 2/Top A	3.8
R27-T	399666	6374653	653	648.8	Base 3/Top B	4.2	648.52	Base B/Top 2	0.28	644.45	Base 2/Top A	4.07

**Figure 45: An Excel spreadsheet containing GPS and thickness data for profiles R00A to R27 and surfaces Base 3/Top B, Base B/Top 2 and Base 2/Top A.**

Each of the Excel datasets had to be saved as text documents and then imported separately into Petrel as well tops, containing the colourless columns and the Z coordinates and names of the surfaces from either the yellow, blue or orange columns. An example of the imported data can be seen in Figure 46. The “well” names, X, Y and Z coordinates and the names of the well tops are listed in the first 5 columns. The last column of data is the calculated thickness of the lobe-element, but it is not needed to generate a well top in Petrel.

**Import petrel well tops: base2topagft.txt**

Column #	1	2	3	4	5
Attribute	Well	X	Y	Z	Surface
Attribute name	Well	X	Y	Z	Surface
Attribute type	Text	Continuou	Continuou	Continuou	Text
Unit		meter	meter	meter	

Connect to trace: R00A-T Number of header lines:

Well name: base2topagft.txt Undefined value:

Depth

Negate Z values

Time

Negate time values

Date

Use current window's settings
  Custom date format:

Header info (first 30 lines):

Line 1:	X	Y			
Line 2:	R00A-T	399360	6373789	635.43	Base 2/Top A 9.42
Line 3:	R00B-T	399319	6373788	633.19	Base 2/Top A 8.12
Line 4:	R00C-T	399356	6373839	649.62	Base 2/Top A 8.42
Line 5:	R01A-T	399461	6373834	629.59	Base 2/Top A 6.96
Line 6:	R01B-T	399413	6373810	629.81	Base 2/Top A 7.82
Line 7:	R02-T	399363	6373957	632.26	Base 2/Top A 7.71
Line 8:	R03-T	399485	6373960	636.11	Base 2/Top A 3.1
Line 9:	R04-T	399406	6374250	655.23	Base 2/Top A 3.33
Line 10:	R05A-T	399305	6374070	643.33	Base 2/Top A 7.83
Line 11:	R05B-T	399263	6374071	637.98	Base 2/Top A 5.72
Line 12:	R06-T	399398	6374267	661.01	Base 2/Top A 4.15
Line 13:	R07-T	399120	6374219	644.24	Base 2/Top A 4.96
Line 14:	R08-T	399071	6374194	657.07	Base 2/Top A 4.45
Line 15:	R09-T	398945	6374123	650.24	Base 2/Top A 3.1
Line 16:	R10-T	398799	6374055	653.88	Base 2/Top A 2.89
Line 17:	R11-T	398687	6373980	655.79	Base 2/Top A 2.79
Line 18:	R12-T	398577	6373981	658.51	Base 2/Top A 2.98
Line 19:	R13-T	398427	6373891	665.68	Base 2/Top A 3.79
Line 20:	R14-T	398468	6373977	662.395	Base 2/Top A 5.28
Line 21:	R15-T	398587	6374072	657.04	Base 2/Top A 3.18

Figure 46: Data for surface Base 2/Top A imported from a text file into Petrel.



### 4.3.4.2. Surfaces

Two different arithmetic equations were used to generate the surfaces in Petrel, namely the Kriging and convergent interpolation algorithms. These two algorithms were chosen as their descriptions in the Petrel help file indicated that they would be the most effective for use with this kind of outcrop data.

Middle Fan 2 is interpreted as a lobe, subdivided into three sandstone-lobe elements and two siltstone inter-lobe elements. Each of these five elements can be classified as a zone in Petrel, with bounding surfaces at top and bottom (Figure 47). Surfaces were generated for each of the elements, though only the lobe-element 2 surfaces are shown in the following section.

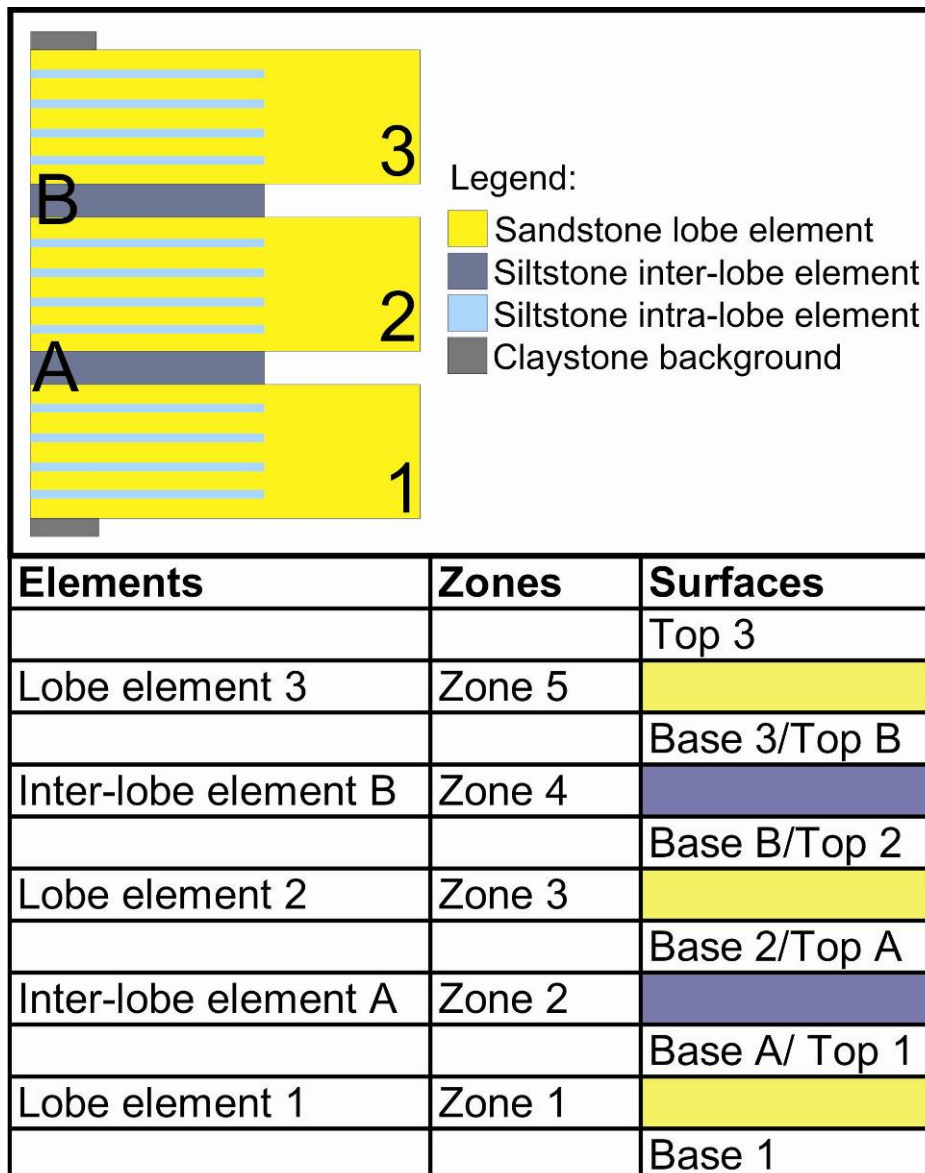


Figure 47: Line diagram illustrating elements, zones and surfaces used in Petrel.

### Vintage attempt 1:

The Kriging algorithm only uses the X, Y and Z data that are within its equation's variogram range, resulting in anomalous extrapolation beyond the variogram range, and the algorithm will not exceed the minimum or maximum values of the data. All default settings were retained. The range was adjusted to 2000 for both the major and minor direction to honour the well data as closely as possible. The default grid size of 50 x 50 metres was used, and polygon A was used as a boundary constraint. The resultant surface (Figure 48) is highly contoured, but does not honour the vertical well data, generating artificial highs and lows, but not with enough variation to honour the actual outcrop topography.

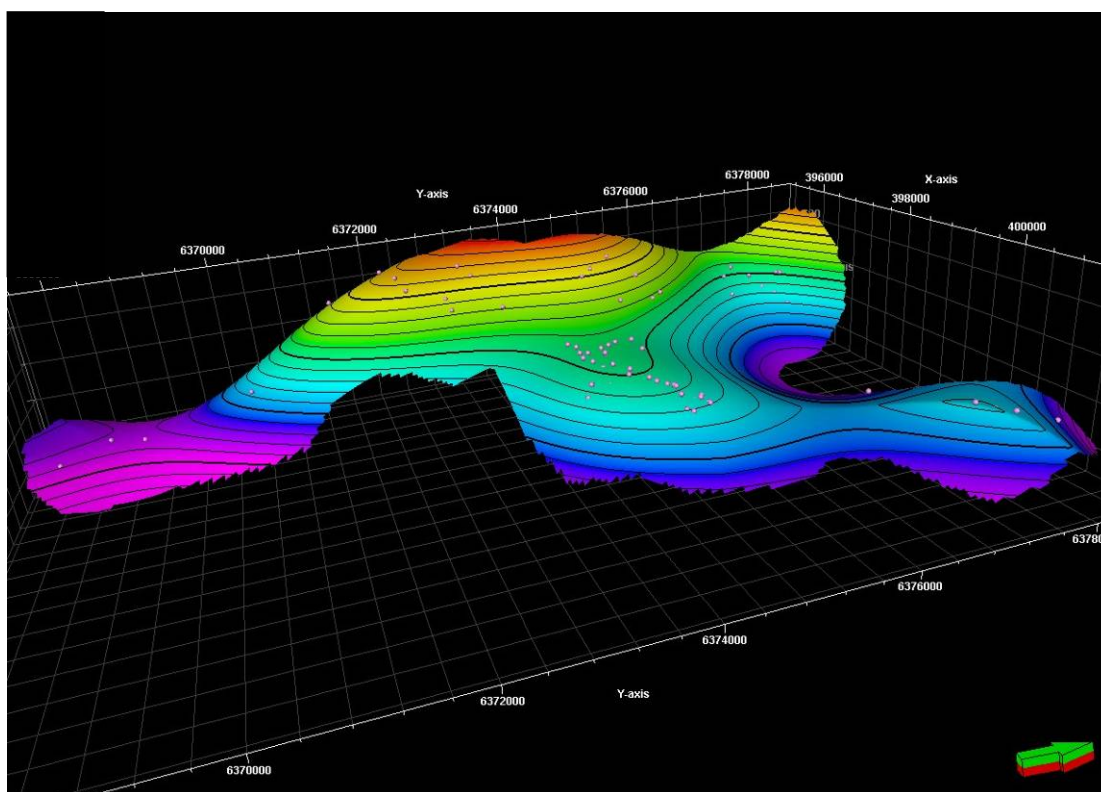


Figure 48: Surface of lobe-element 2 done using the Kriging algorithm.

### Iterative step A:

As the Kriging algorithm did not honour the topographic outcrop data sufficiently, it was decided to attempt to create a surface using the convergent interpolation algorithm. It is important to honour the topography as closely as



followed on top of each other in the correct horizontal sequence without crossing in order to create accurate isopach maps.

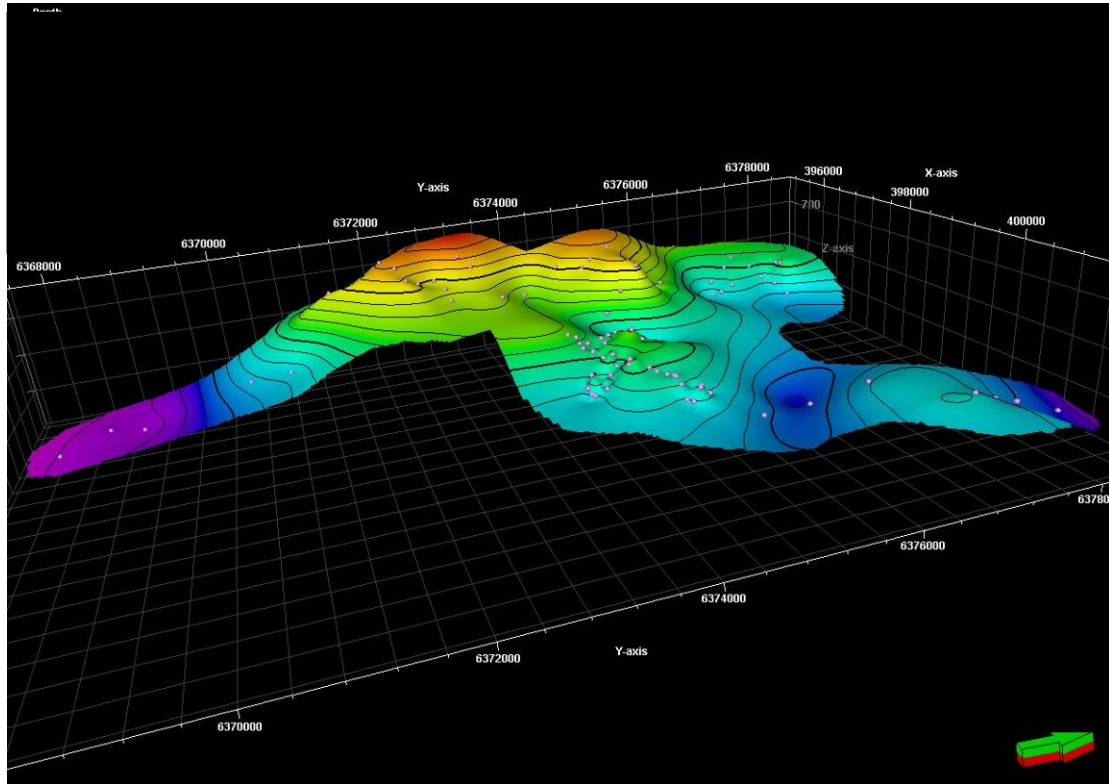


Figure 49: Surface of lobe-element 2 done using convergent interpolation and polygon A.

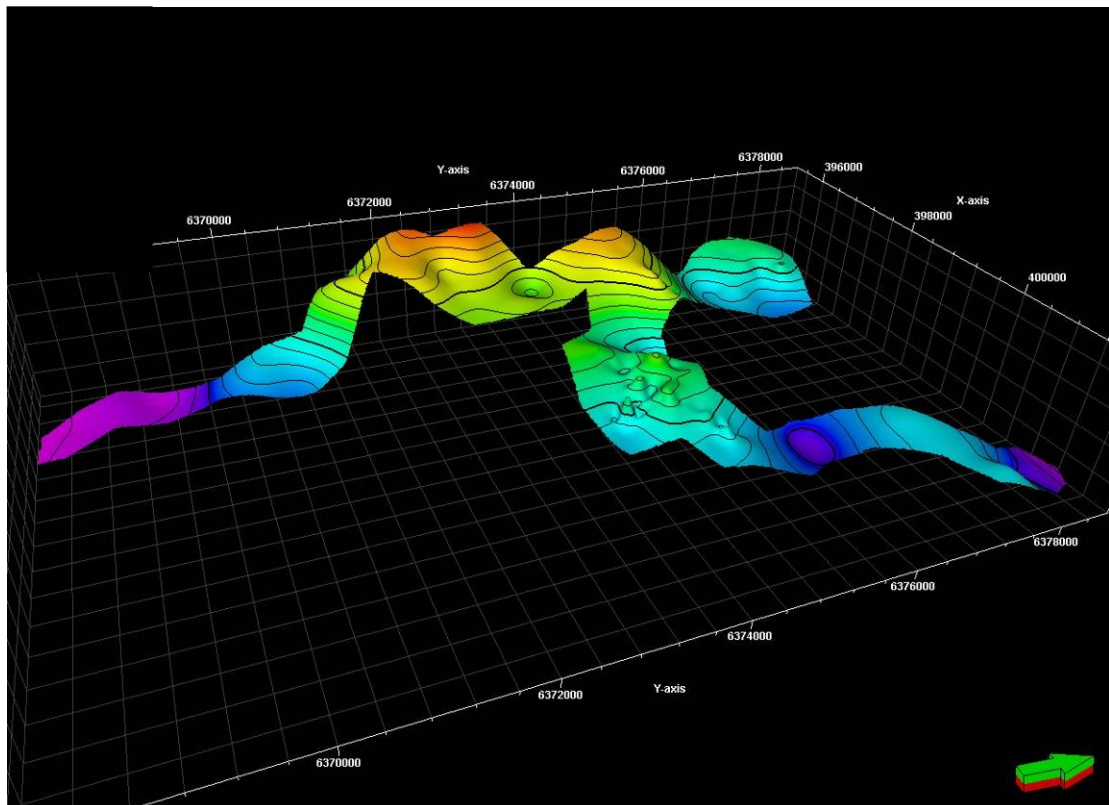


Figure 50: Surface of lobe-element 2 done using convergent interpolation and polygon B.

### 4.3.4.3. Isopach (thickness) maps

Petrel isopach maps were generated by subtracting the Z-values of one surface from another to illustrate the variation in thickness between two surfaces, for each of the lobe and inter-lobe elements, using both polygons A and B (Appendix C). Only the isopachs generated for sandstone-lobe element 1 and siltstone inter-lobe element A are shown in the following section. The scale was set at 0 – 10 metres for the sandstone maps, and at 0 – 1 metres for the siltstone maps. Rose diagrams illustrating the palaeocurrent orientations are superimposed on each of the isopach maps. Amalgamation between sandstone-lobe elements means siltstone inter-lobe elements are often absent, resulting in anomalous maps. Warm colours indicate a minimum thickness and cold colours a maximum thickness, with the scale on each of the isopach maps indicated in depth (thickness).

#### Vintage attempt 1:

The first isopach maps of sandstone-lobe element 1 (Figure 51) and siltstone inter-lobe element A (Figure 52) were generated using the Kriging algorithm and polygon A with the default grid size of 50 x 50 metres.

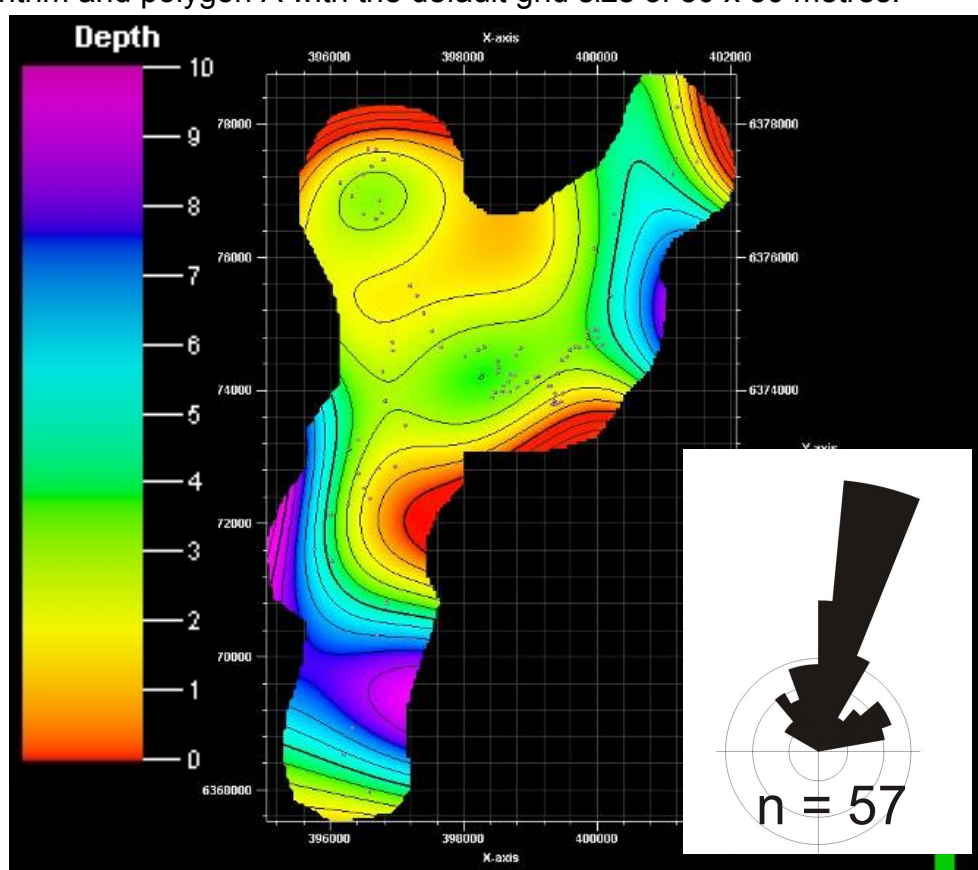
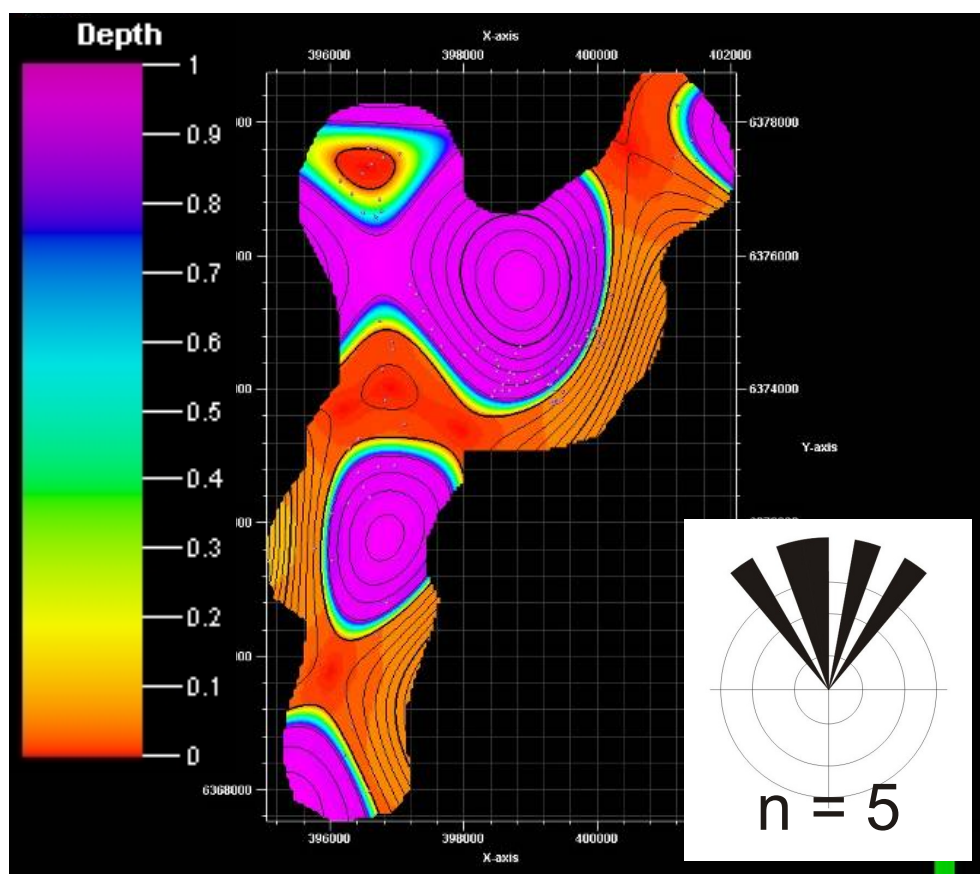


Figure 51: Isopach map for sandstone-lobe element 1 calculated from surfaces generated using Kriging interpolation and polygon A.





**Figure 52: Isopach map for siltstone inter-lobe element A calculated from surfaces generated using Kriging interpolation and polygon A.**

### **Iterative step A:**

The isopach maps calculated from surfaces generated using the using the Kriging algorithm shows anomalous thickening (indicated in purple) and thinning (indicated in red) of the lobe and inter-lobe elements, which does not honour the outcrop data. The isopach maps also appear artificially smoothed with no local highs or lows. The convergent interpolation algorithm was used in an attempt to honour the outcrop thicknesses more accurately.

### **Vintage attempt 2:**

A second isopach map of sandstone-lobe element 1 (Figure 53) was calculated from surfaces generated using the convergent interpolation algorithm and polygon A with the default grid size of 50 x 50 metres. An isopach map of siltstone inter-lobe element A (Figure 54) was also generated.

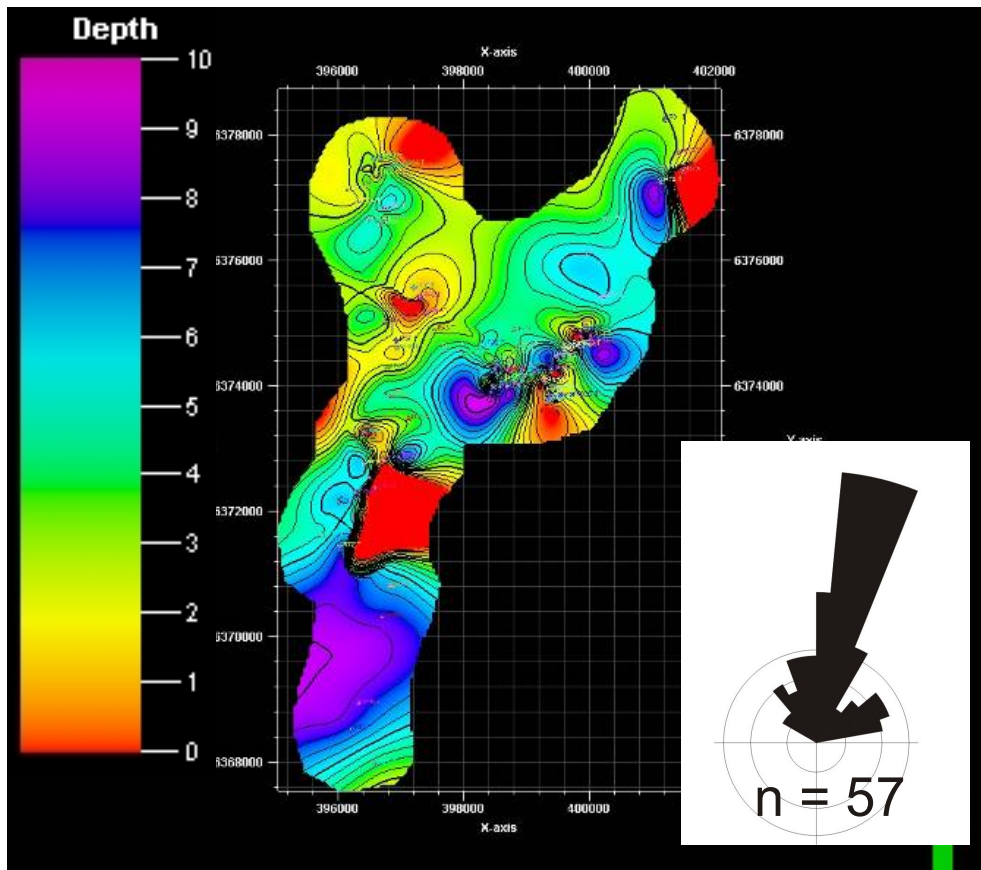


Figure 53: Isopach map for sandstone-lobe element 1 calculated from surfaces generated using convergent interpolation and polygon A.

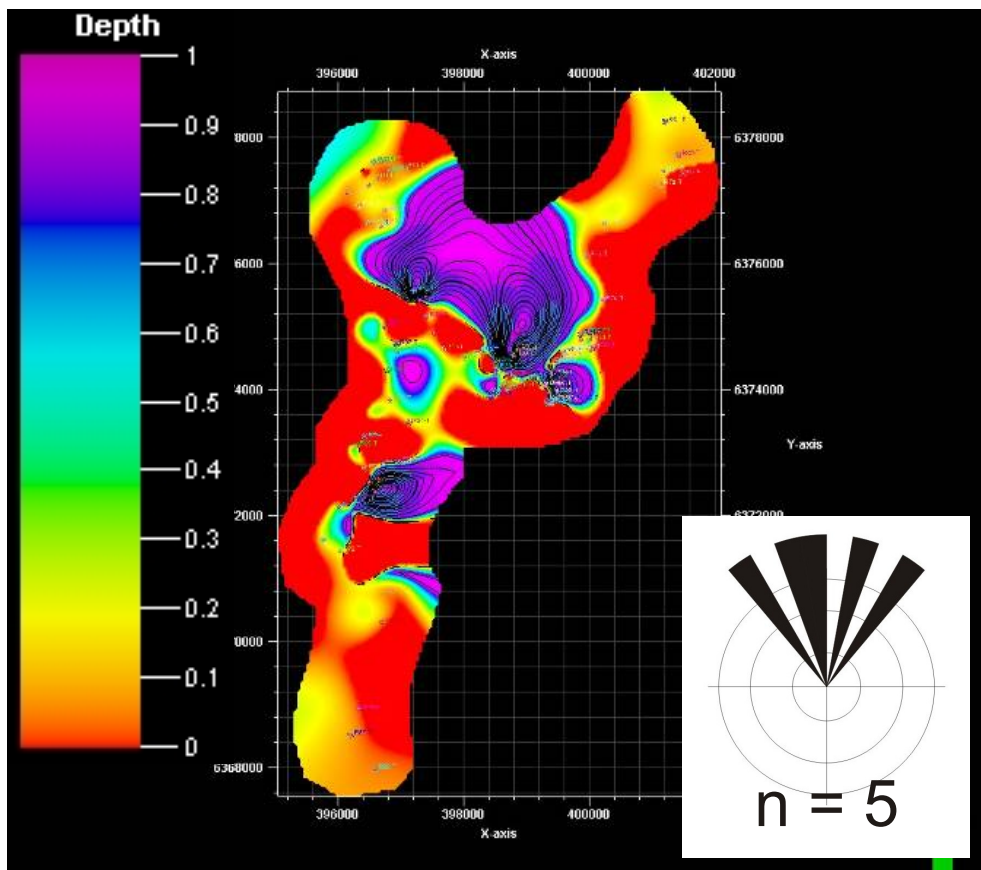


Figure 54: Isopach map for siltstone inter-lobe element A calculated from surfaces generated using convergent interpolation and polygon A.

### Iterative step B:

The isopachs calculated from surfaces generated using the convergent interpolation algorithm show a closer approximation to the outcrop data than those generated using the Kriging algorithm, but there are still areas outside of the data points that show some anomalous extrapolation. In an attempt to decrease the amount of extrapolation in areas where there are little or no data, isopachs were calculated again from surfaces generated using convergent interpolation and polygon B.

### Vintage attempt 3:

Isopach maps were calculated using surfaces generated for sandstone-lobe element 1 (Figure 55) and siltstone inter-lobe element A (Figure 56) using convergent interpolation and polygon B at the default Petrel range of 50 x 50 metres. Much less anomalous extrapolation in the form of red and purple are visible in the thickness maps.

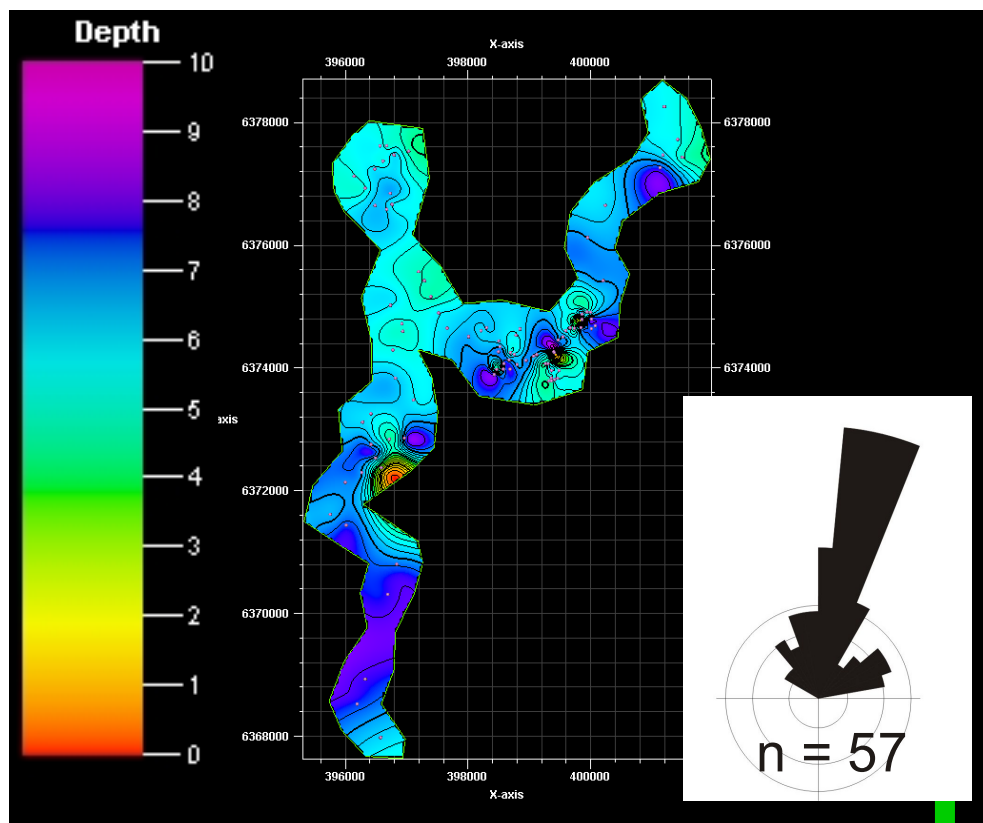
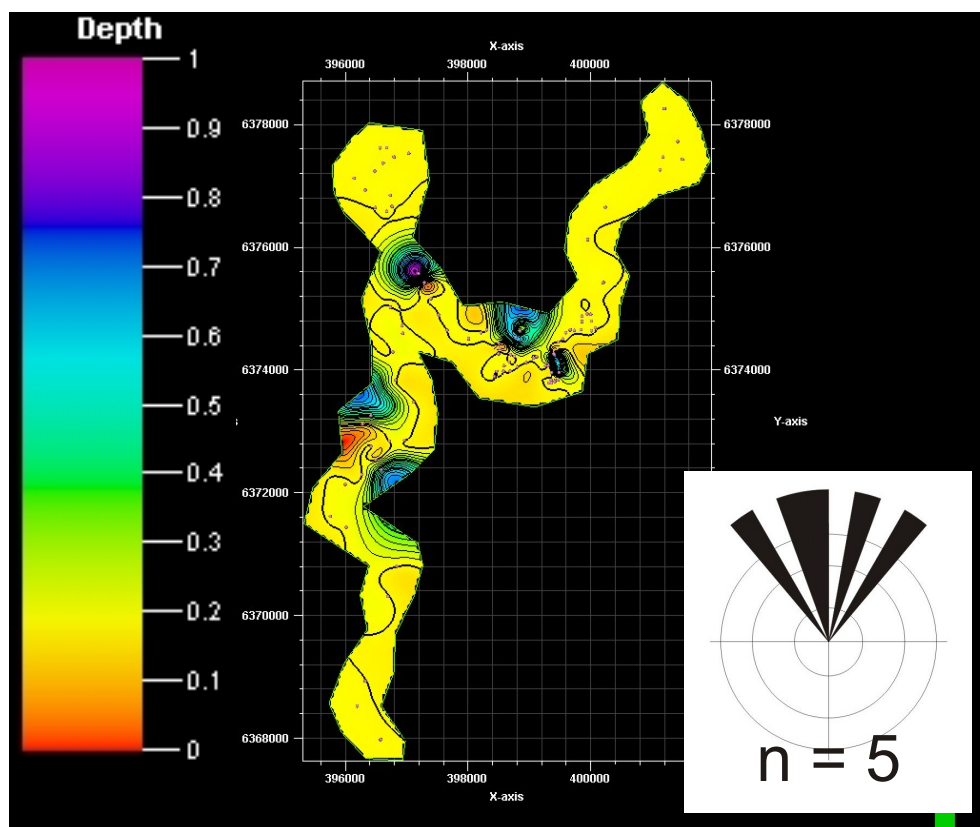


Figure 55: Isopach map for sandstone-lobe element 1 using convergent interpolation and polygon B at a range of 50 metres.





**Figure 56: Isopach map for siltstone inter-lobe element A using convergent interpolation and polygon B at a range of 50 metres.**

#### **Final attempt 4:**

The final isopach maps for sandstone-lobe element 1 (Figure 57) and siltstone inter-lobe element A (Figure 58) were calculated using the convergent interpolation-generated surfaces constrained by polygon B. The grid size was reduced to 5 x 5 metres and proved to be the most accurately generated isopach map for the sandstone-lobe element.

The only anomalously generated thickness data (in red) can be seen in areas where there is no outcrop available. The siltstone isopach map still indicates large areas of anomalous thickness data (in red and purple). This may be accurate as a large area of the outcrop does not contain siltstone inter-lobe element A as it is often amalgamated, eroded or weathered.

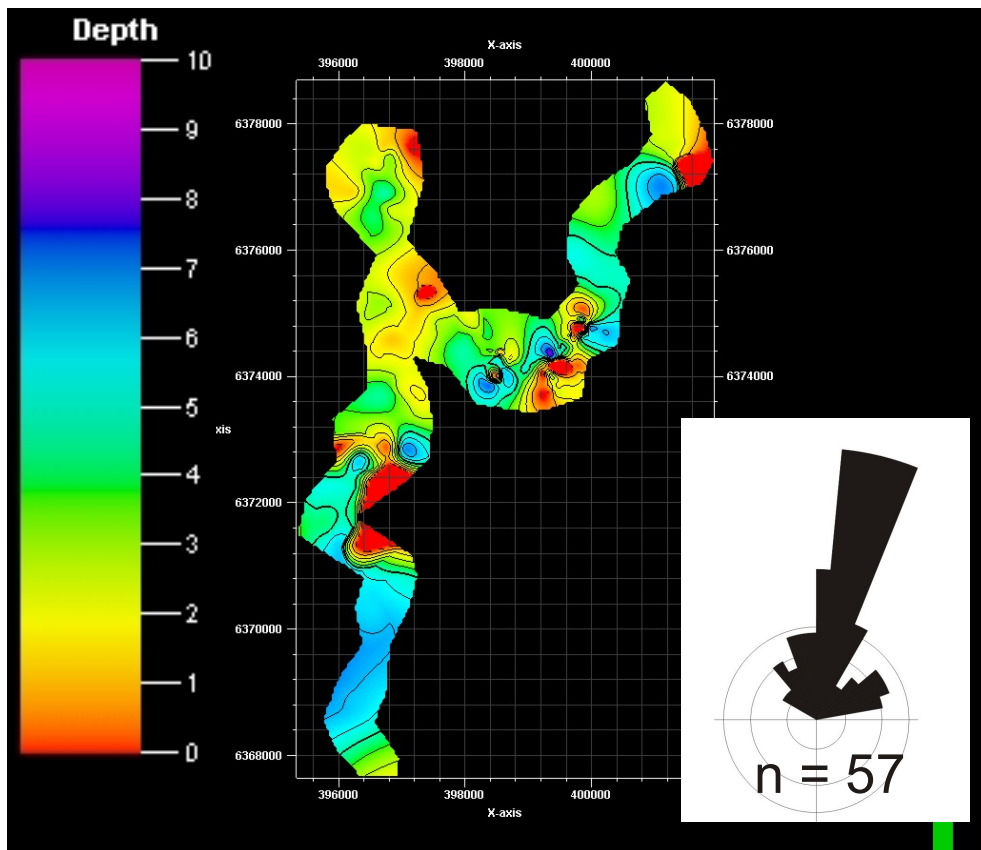


Figure 57: Isopach map for sandstone-lobe element 1 calculated from surfaces generated using convergent interpolation and polygon B at a range of 5 metres.

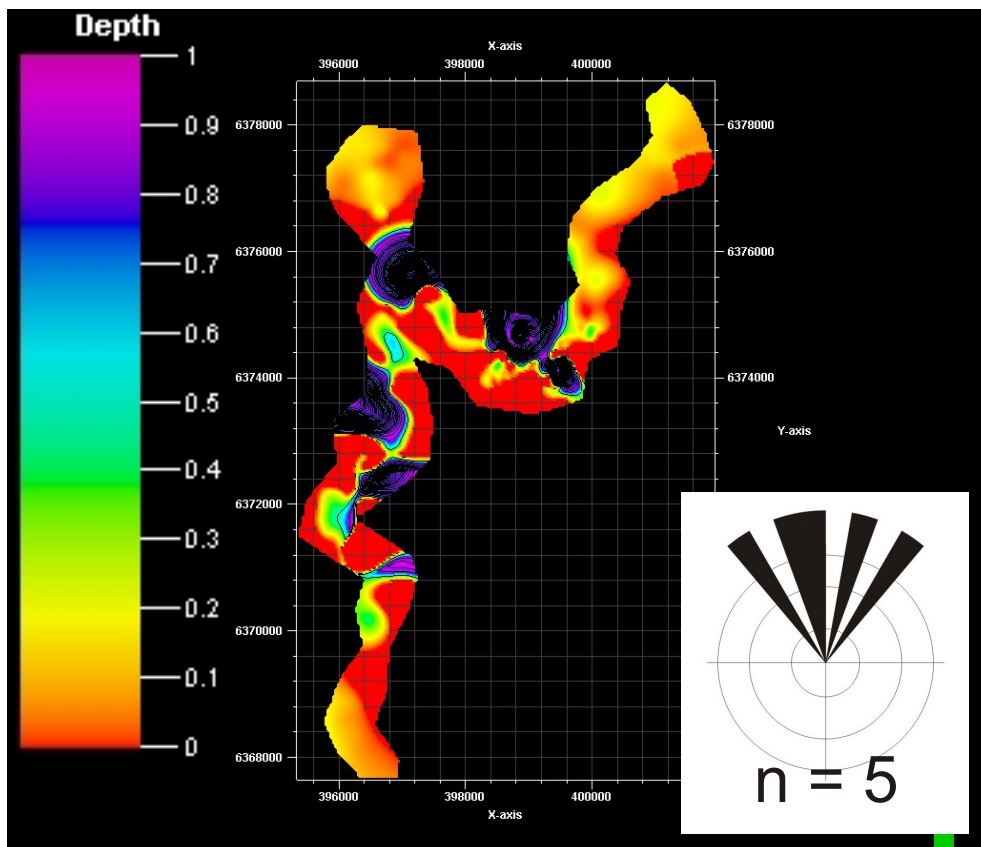


Figure 58: Isopach map for siltstone inter-lobe element A calculated from surfaces generated using convergent interpolation and polygon B at a range of 5 metres.

#### 4.3.4.4. Static model grids

A grid with cell-dimensions of 20 x 20 x 0.2 m was defined using the created surfaces. The algorithms used include the Kriging algorithm and the sequential indicator simulation. The facies data imported from DSL and the thickness data of the lobe elements and inter-lobe elements were imported into the model to allow the programme to build up the elements in Middle Fan 2 layer by layer. Grids produced using surfaces generated by vintage attempts resulted in anomalous truncations and pinch-outs. The grid produced using the final surfaces resulted in a more accurate representation of the elements in Middle Fan 2.

#### 4.3.4.5. Upscaling of facies

Layering defines the vertical scale of the cells as it subdivides each of the five zones generated in the static model grid into discrete layers. The zones correspond to the sandstone-lobe elements and siltstone inter-lobe elements.

##### Vintage attempts 1 and 2:

Layers with a thickness of 20 cm were assigned to each of the five zones using the “follow top” command (Figure 59). This causes each of the underlying layers to follow parallel to the layer created above and shows a top-lap truncation. The “follow top” command was chosen as each of the vertical profiles or “wells” used the top GPS coordinates as a datum. The layering was then used for the upscaling of the facies using the Kriging algorithm in the first attempt and sequential indicator simulation in the second attempt.

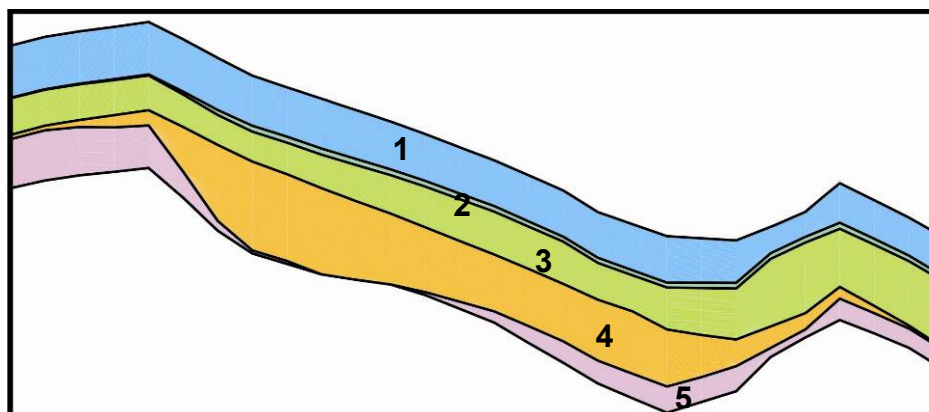


Figure 59: Zones 1 - 5 representing each of the elements subdivided into fixed layers.



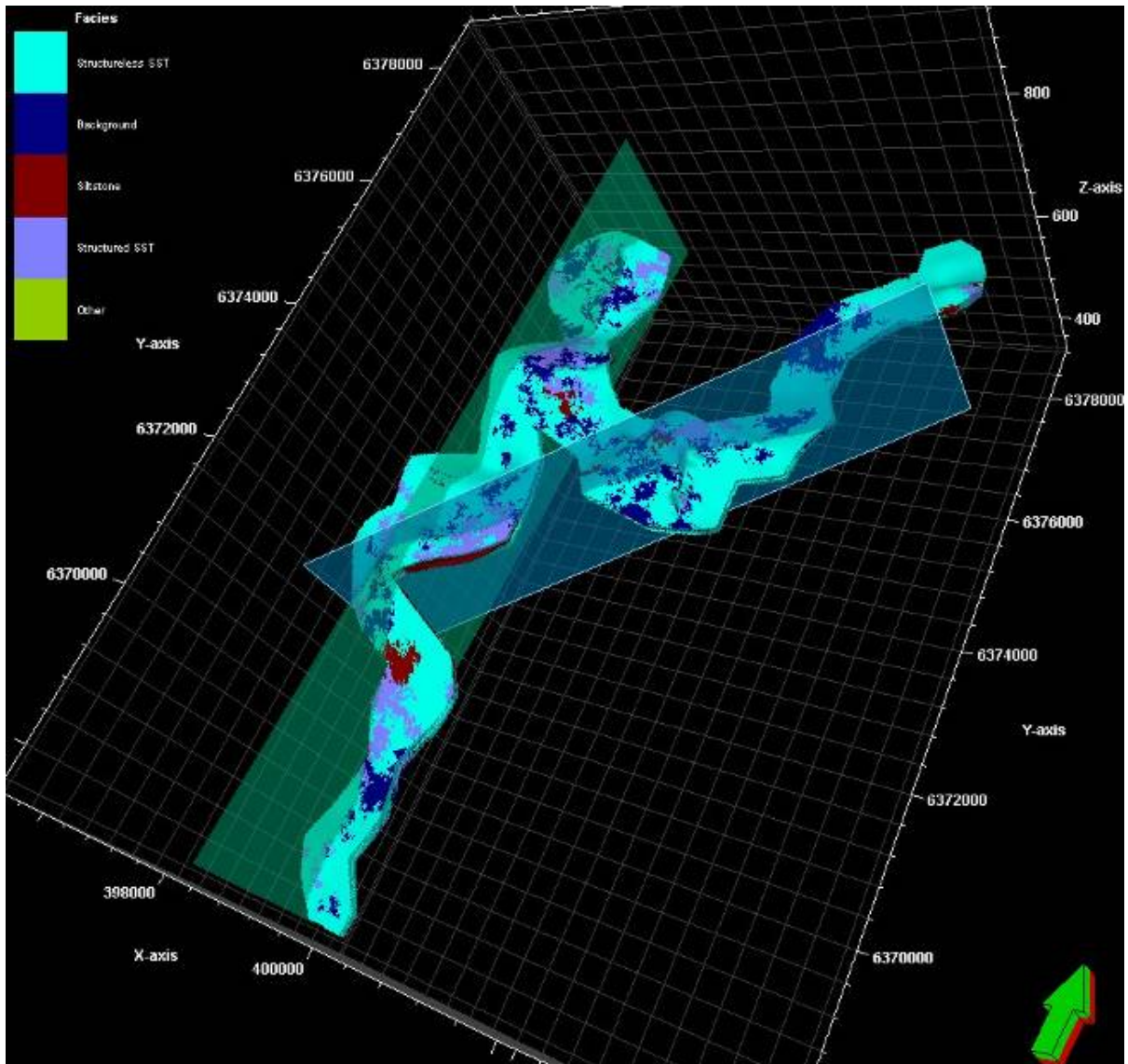
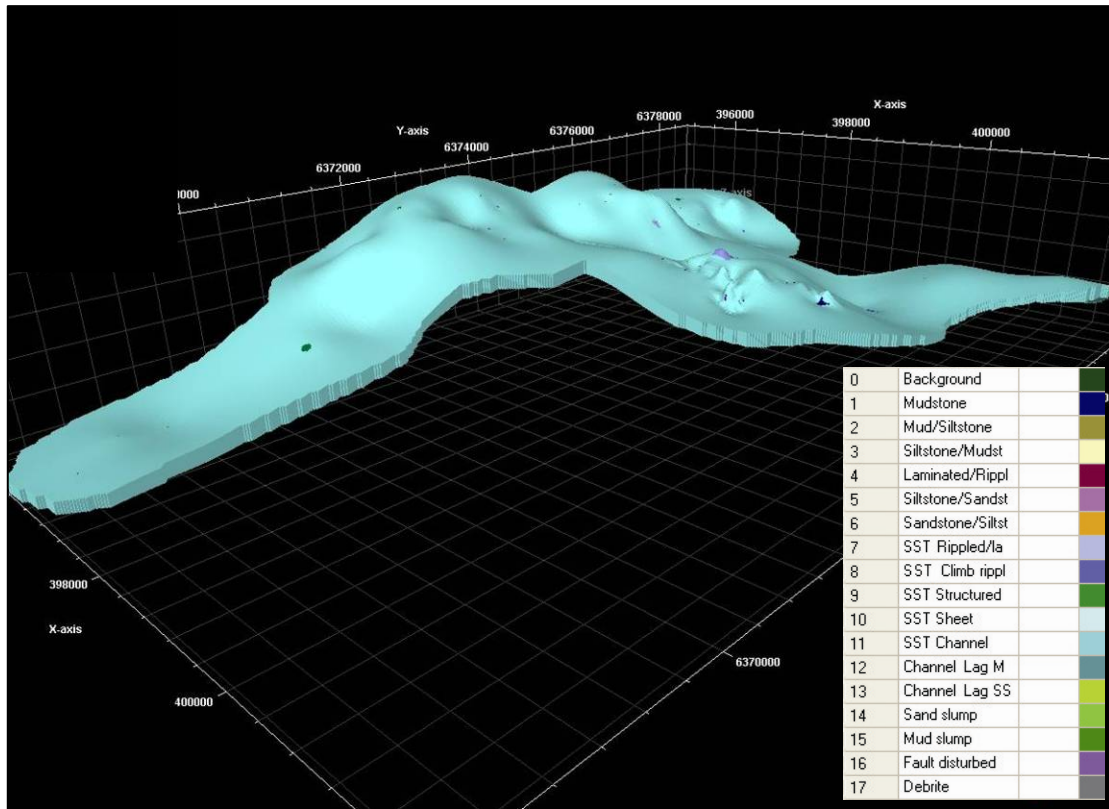


Figure 62: Locations of strike (green) and dip (blue) correlation panels.

increased from 1000 metres to 2000 metres, when using the sequential indicator simulation in an attempt to rectify this problem.



**Figure 65: Facies-model attempt 1 using the Kriging algorithm and polygon A shown at 10 x VE.**

A horizontal intersection was made through the Kriging algorithm facies model to illustrate the internal structure of the demarcated zones. No discrete internal layering can be seen for the first facies model. The location of the horizontal intersection and its close-up for the Kriging algorithm facies model illustrates the lack of visible facies (Figure 66).

### **Iterative step C:**

The Kriging algorithm was replaced by the sequential indicator simulation in an attempt to generate zones with more discrete internal layering indicating extrapolated facies to capture the internal heterogeneity of Middle Fan 2.

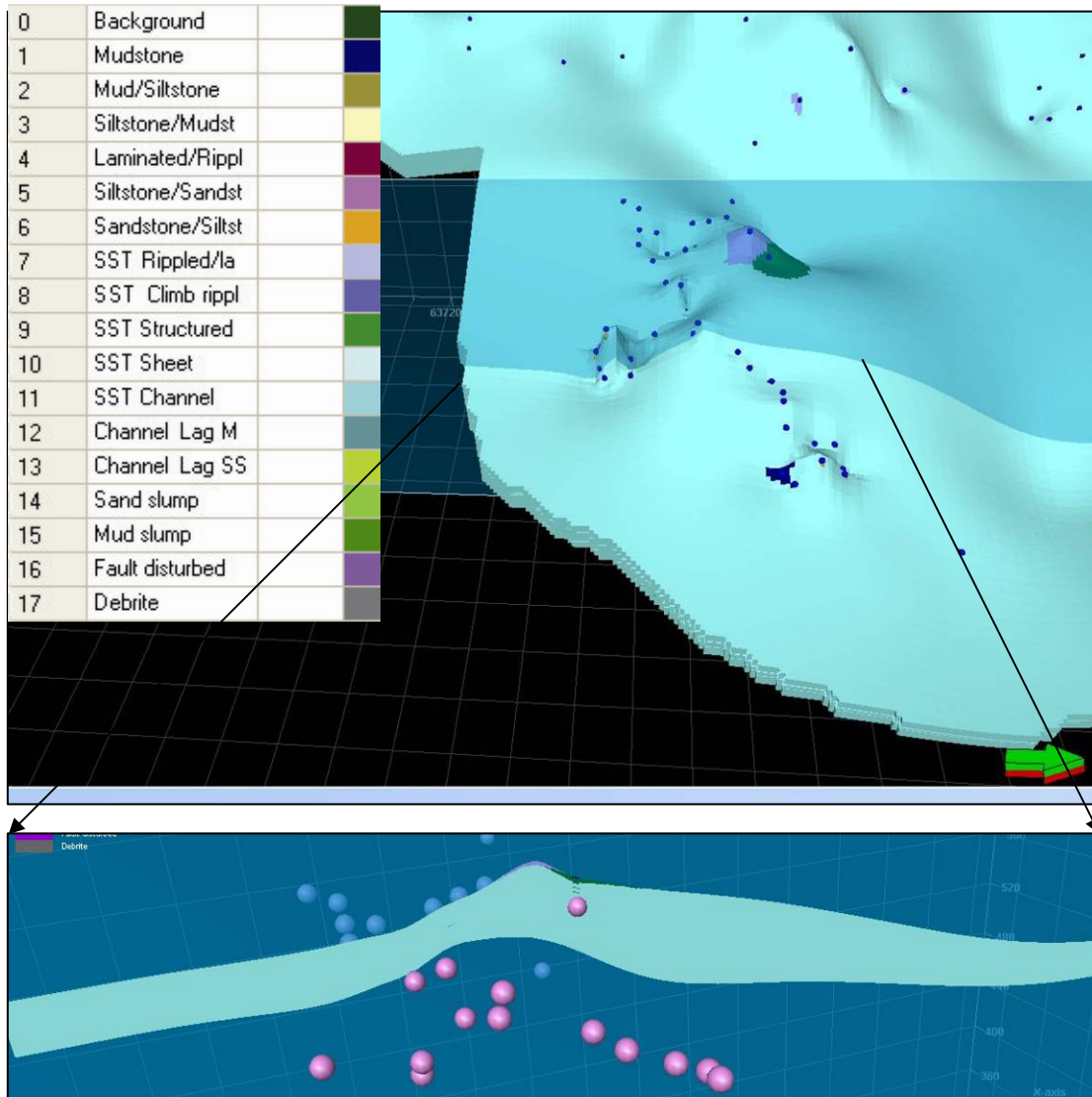


**Figure 66: Close-up of an intersection (in darker blue) through the Kriging algorithm facies model confined to polygon A.**

### **Vintage attempt 2:**

The sequential indicator simulation applies stochastic modelling using the input upscaled well log data, distributions, variograms and trends. The algorithm generates a more accurate model than the Kriging algorithm when the shapes of any of the facies bodies are unknown or uncertain. The result is a closer representation of the facies found in the study area.

The second facies model was generated using the sequential indicator simulation confined to polygon A (Figure 67). As the layering of the zones is



extrapolated by the Petrel program, pinch-outs are not uncommon, where there are in actuality no pinch-outs in the measured outcrop.

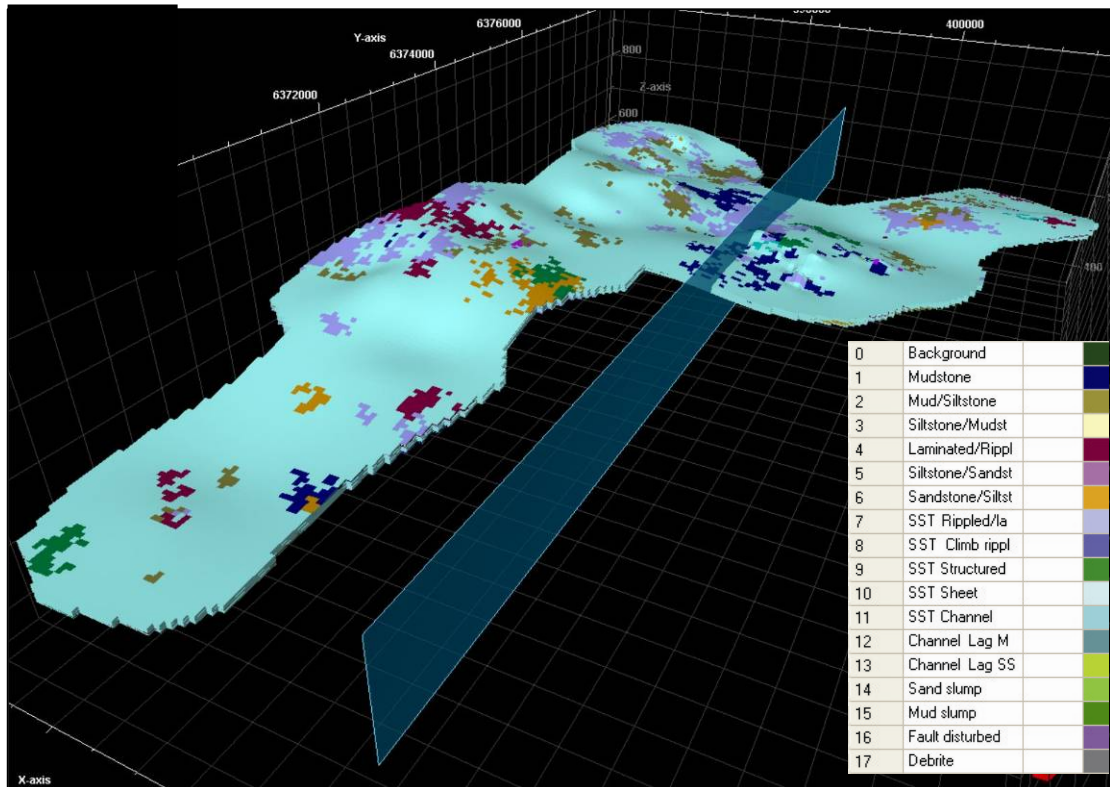


**Figure 67: Facies-model attempt 2 using sequential-indicator simulation and polygon A at 10 x VE.**

A horizontal intersection through the sequential indicator simulation facies model (Figure 68) shows that some connectivity is visible between the facies. The facies can however not be effectively subdivided into discrete sandstone and siltstone units as there is not enough detail available. This indicates that the area of influence is still not large enough, resulting in the facies appearing patchy rather than layered as they are not extrapolated far enough laterally.

#### **Iterative step D:**

Another grid was created with a size of 20 x 20 metres, but instead of assigning a thickness of 20 cm to each layer as was previously done, proportional layering was used. Sixty layers were assigned to each of the zones that represent sandstone-lobe elements 1, 2 and 3, and one layer was assigned to each of the two siltstone inter-lobe elements. The area was constrained to polygon B (also used in iterative step B) in an attempt to limit

the extrapolation of data outside of the constraints of the polygon and the study area.

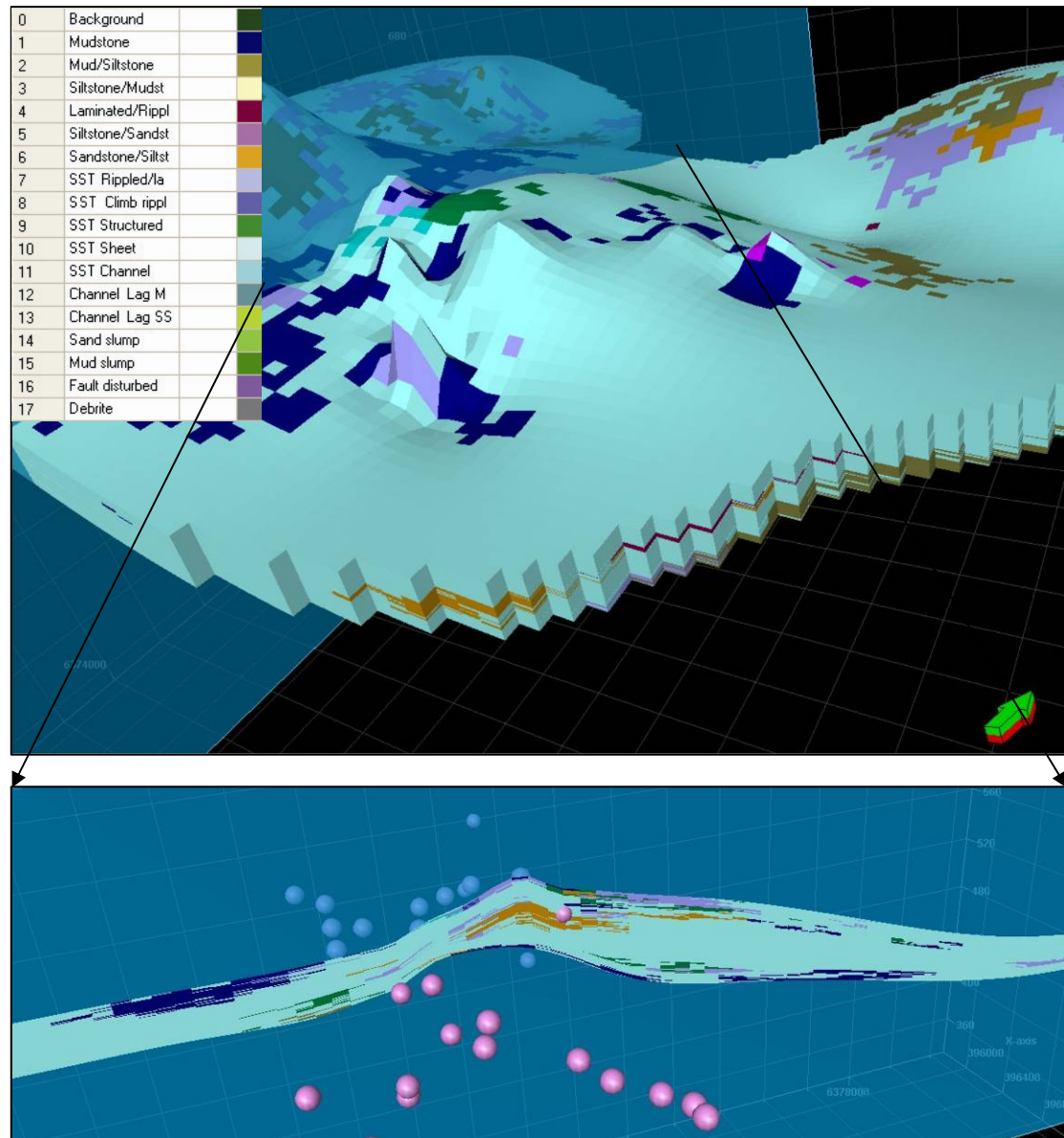


**Figure 68: Close-up of an intersection (in darker blue) through the sequential-indicator simulation facies model confined to polygon A.**

### **Iterative step E:**

The number of facies was decreased from the 19 original DSL facies to the five facies generated for Petrel to create a less cluttered facies model and to simulate the conditions found in outcrop.

### Final attempt 3: “Success case”

The final and most successful facies model attempt was generated with the following characteristics:

1. Sequential indicator simulation algorithm;
2. Study area confined to polygon B;
3. Static model grid size of 20 x 20 m;
4. Proportional layering assigning 60 layers to each sandstone zone and 1 layer to each siltstone zone;
5. Facies reduced from 19 to 5.

In the final facies model (Figure 69) the different facies can be more clearly defined across the study area. The internal layering of the sandstone-lobe elements and siltstone inter-lobe elements can also be more clearly defined (Figure 70).

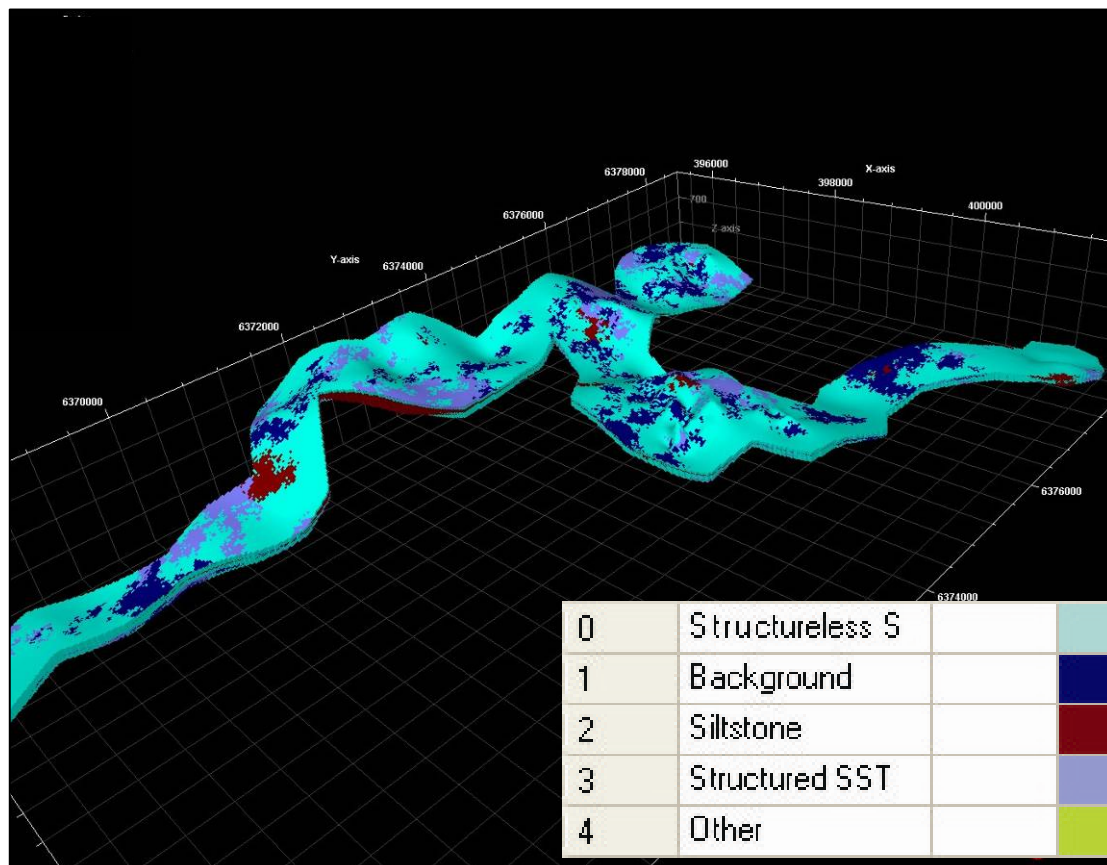
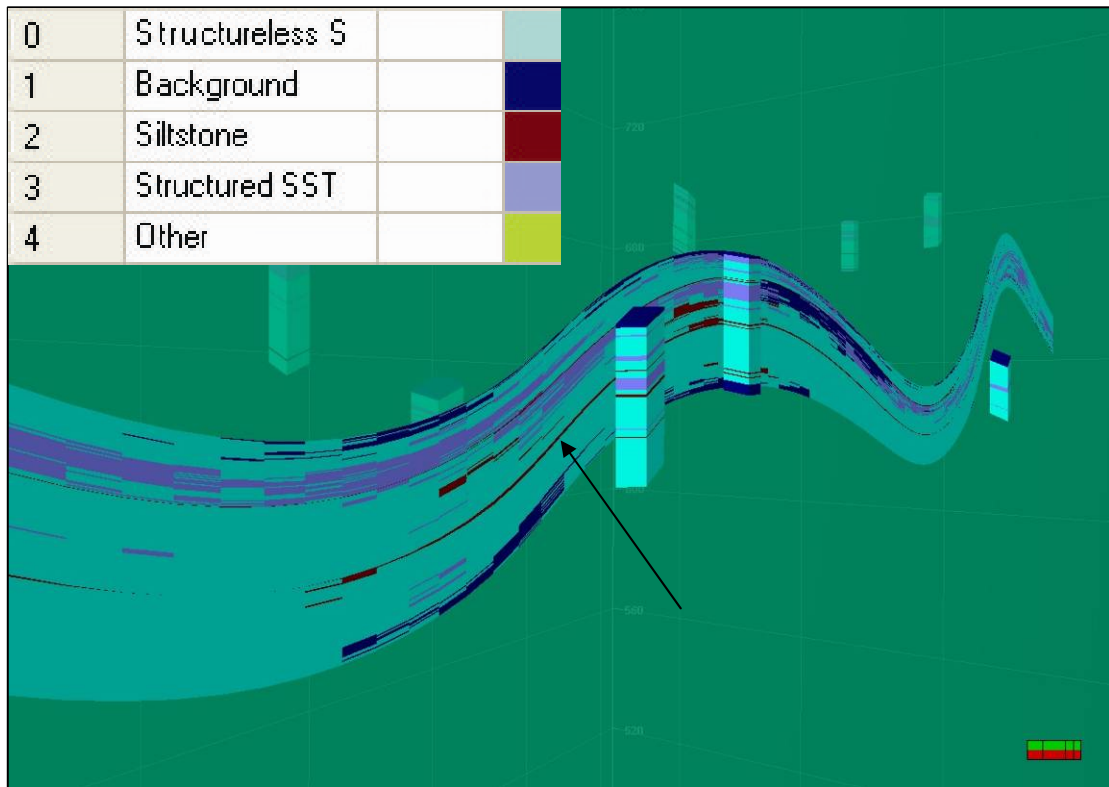


Figure 69: Final facies model attempt using sequential-indicator simulation and polygon B at 10 x VE.





**Figure 70: Close-up of a section through some of the study area showing up-scaled well logs and the siltstone inter-lobe elements clearly defined as a discrete layer (arrow).**

Also shown is an intersection through an area with a good indication of layering, although there is still an abnormally thickened siltstone towards the right of the intersection (Figure 71).

This abnormality is attributed to the siltstone thickness being anomalously extrapolated due to a lack of well data in that specific area. The input of dummy wells into sections of the study area, where there are little or no outcrop data available, will limit the amount of extrapolation. This will in turn result in a more accurate facies model.

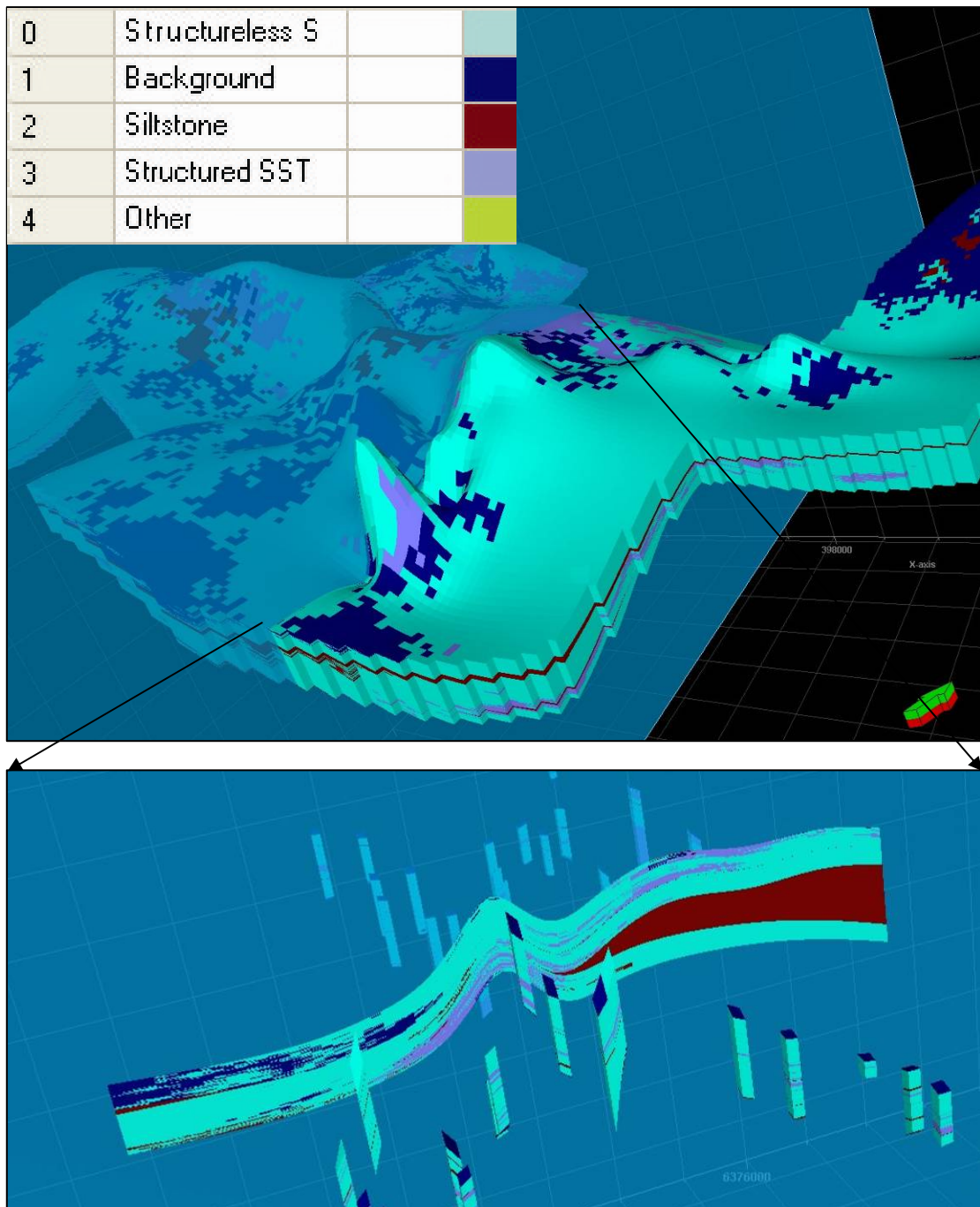
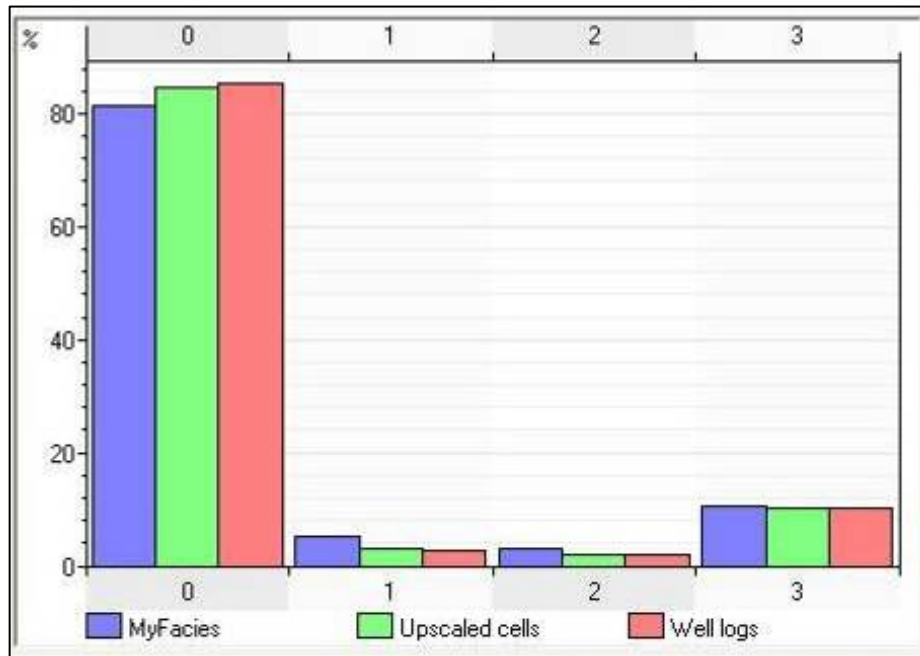


Figure 71: Close-up of an intersection (in darker blue) through the sequential-indicator simulation facies model confined to polygon B.

#### 4.3.5. Results and discussion

After the sequential indicator simulation was used to generate the final attempt at a facies model, a histogram was created (Figure 72). This histogram shows the correlation between the facies associations created for the 3-D Petrel grid (“MyFacies”, in blue), the upscaled or (“Upscaled cells”, in green), and the input facies created by DSL (“Well logs”, in pink). The

numbers 0, 1, 2 and 3 correspond to the dominant facies associations that were used in the final facies model, namely massive sandstone, background deposition, siltstone and structured sandstone.



**Figure 72: Histogram showing the correlation between “MyFacies”, “Upscaled cells” and “Well logs”. The number 0 refers to massive sandstone, 1 to background deposition, 2 to siltstone and 3 to structured sandstone.**

The histogram indicates that the input facies (“Well logs”), upscaled wells (“Upscaled cells”) and the Petrel facies associations (“MyFacies”) retain approximately the same percentage throughout, proving that a minimal amount of data was lost during each of the processes. This indicates that the 3-D percentage of the facies is equivalent to the input well data.

This is a function of the good 3-D control provided by the outcrop data, resulting in the high-quality input facies generating high-quality output facies. This also reiterates the importance of the iterative process and doing careful quality control of the field data. This ensures that surfaces and well tops generated using the field data are as accurate as possible.



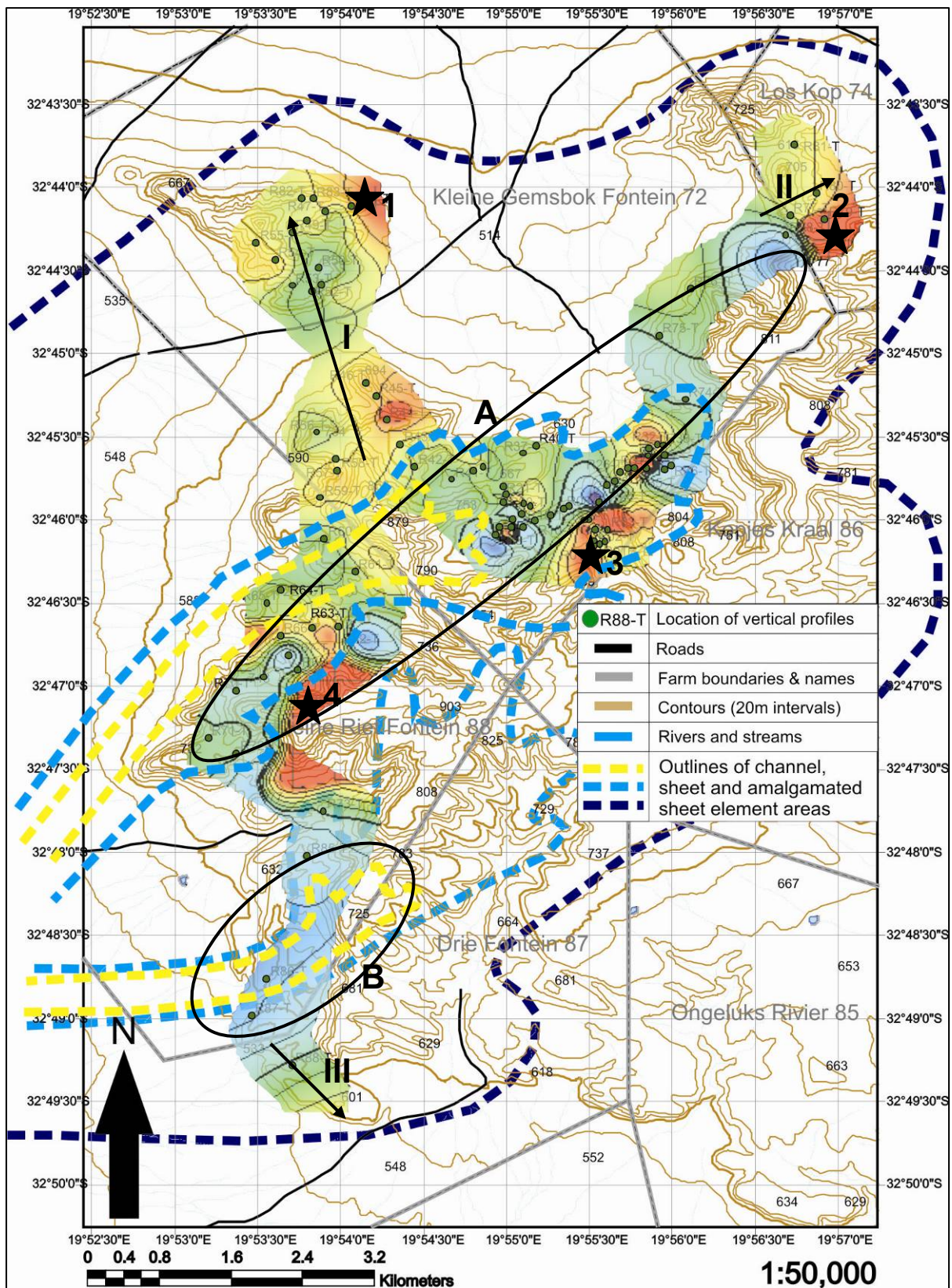


Figure 74: Depositional model superimposed on isopach map of lobe-element 1.



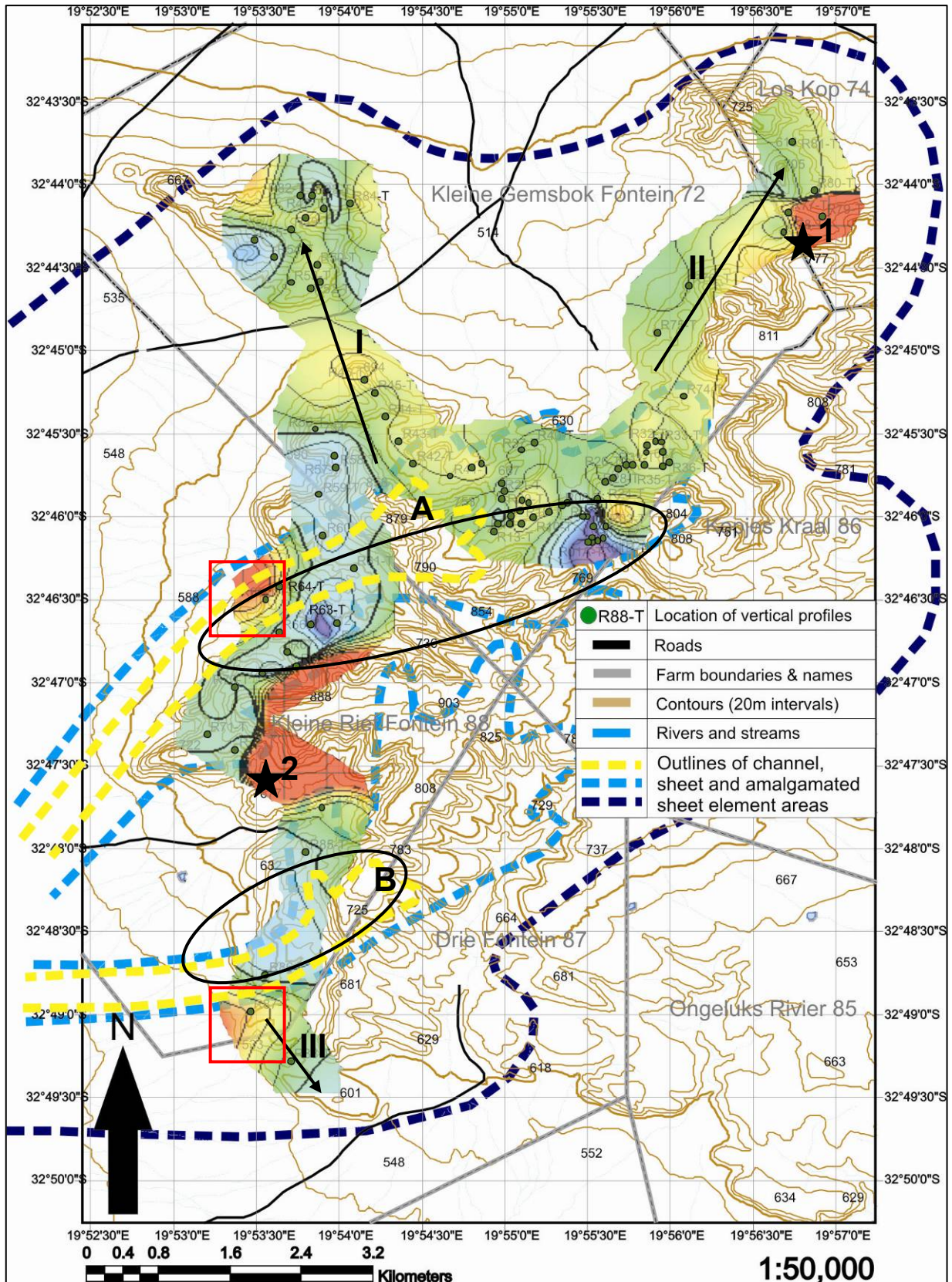


Figure 75: Depositional model superimposed on isopach map of lobe-element 2.



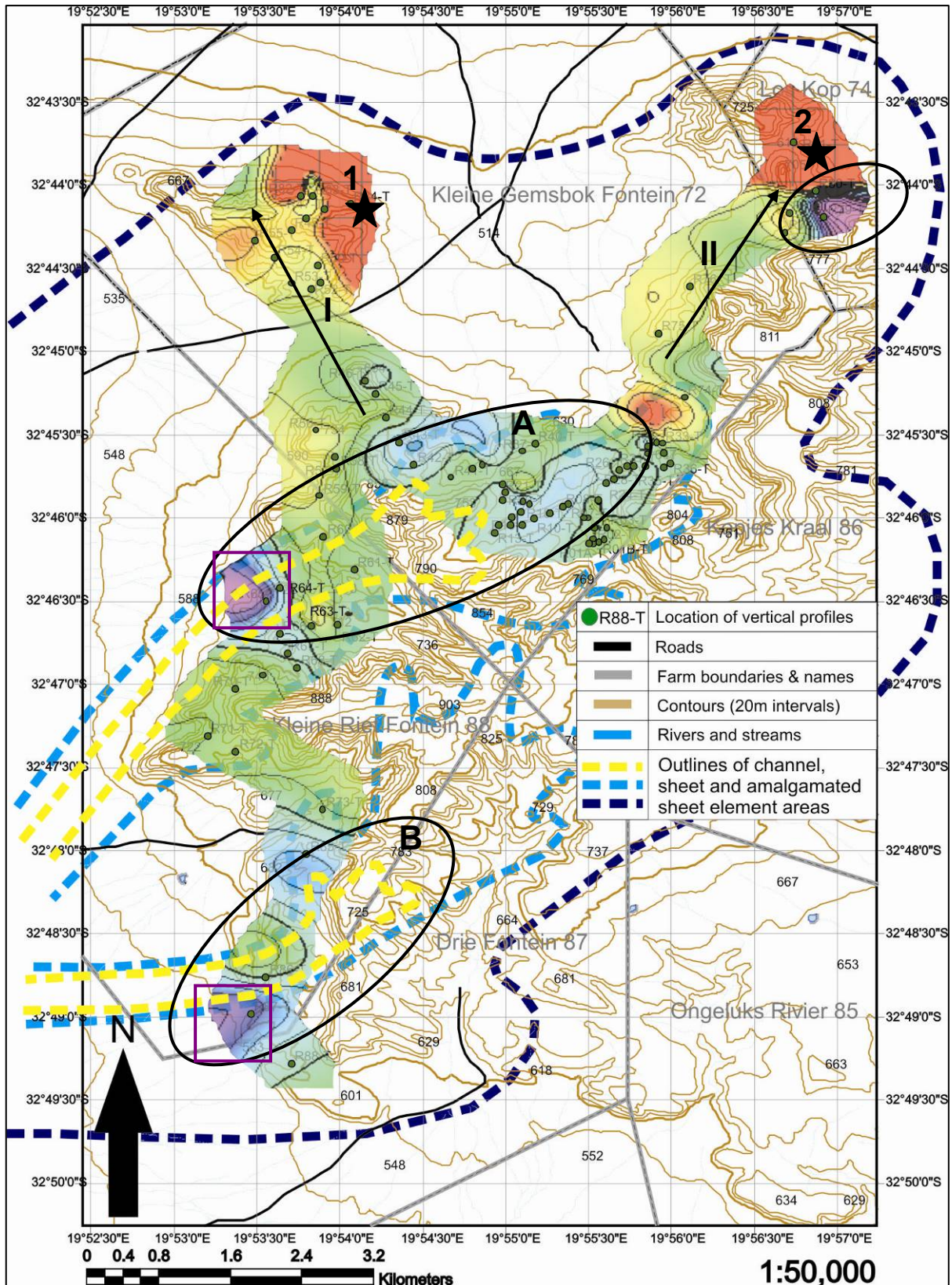


Figure 76: Depositional model superimposed on isopach map of lobe-element 3.



## 5. Stratigraphy and architectural elements

### 5.1. Stratigraphy

To simplify the lateral correlation of the vertical profiles, Middle Fan 2 was subdivided into three sandstone-lobe elements (designated 1, 2 and 3 from base to top) and two siltstone inter-lobe elements (designated A and B from base to top, Figure 77). There are also numerous siltstone intra-lobe elements found within the sandstone-lobe elements. They vary in thickness from less than a centimetre, thus a lamina, to 25 centimetres, thus a medium bed (Boggs, 2006), and are occasionally thicker than the siltstone inter-lobe elements, but not as laterally extensive.

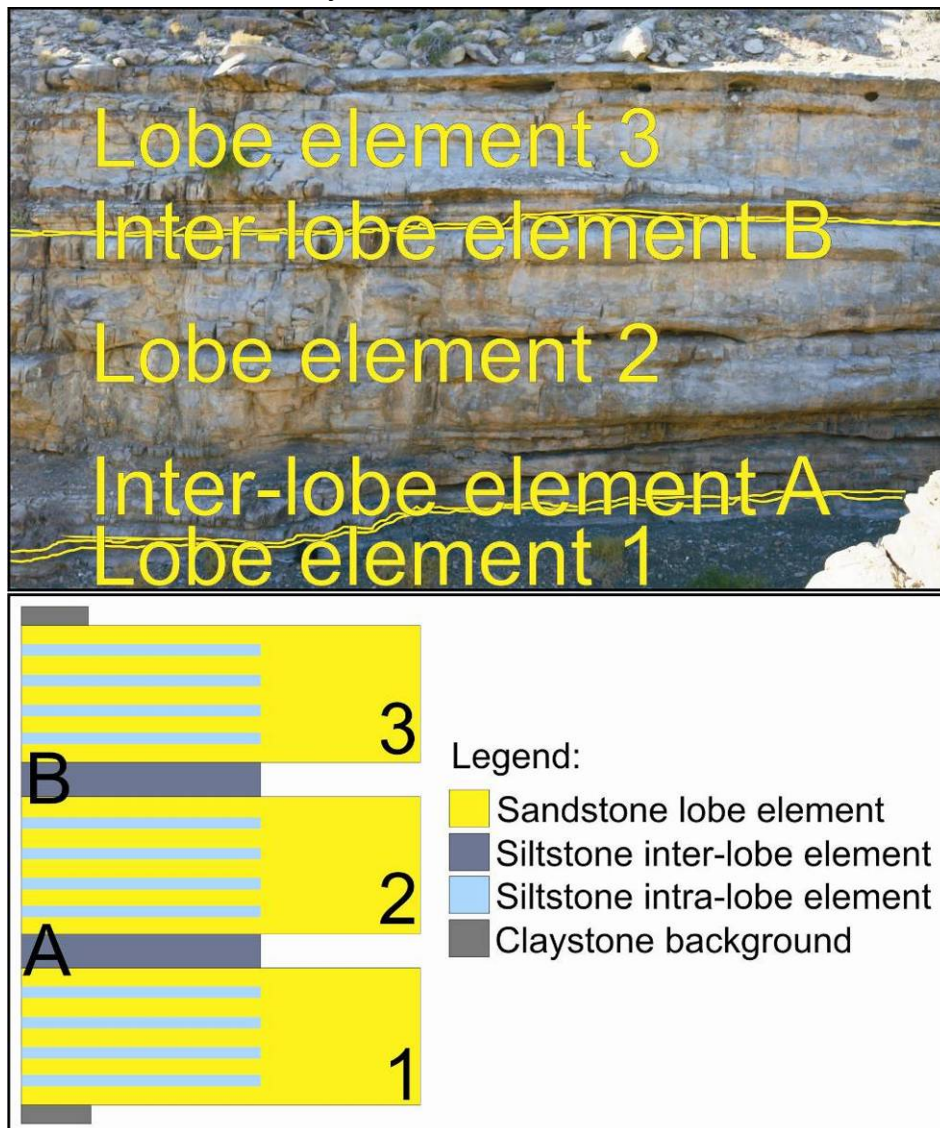


Figure 77: Diagram illustrating the internal stratigraphy of Middle Fan 2; photo location in the vicinity of vertical profile R00A (34H0399360/UTM6373789, on the farm Kleine Gemsbok Fontein 72).

## 5.2. Architectural elements

Only two types of architectural elements were recognised in the Middle Fan 2 outcrop, namely channel elements and sheet elements, making them the focus of this chapter. The outcrop data are represented as vertical profiles using CorelDraw (Figure 78).

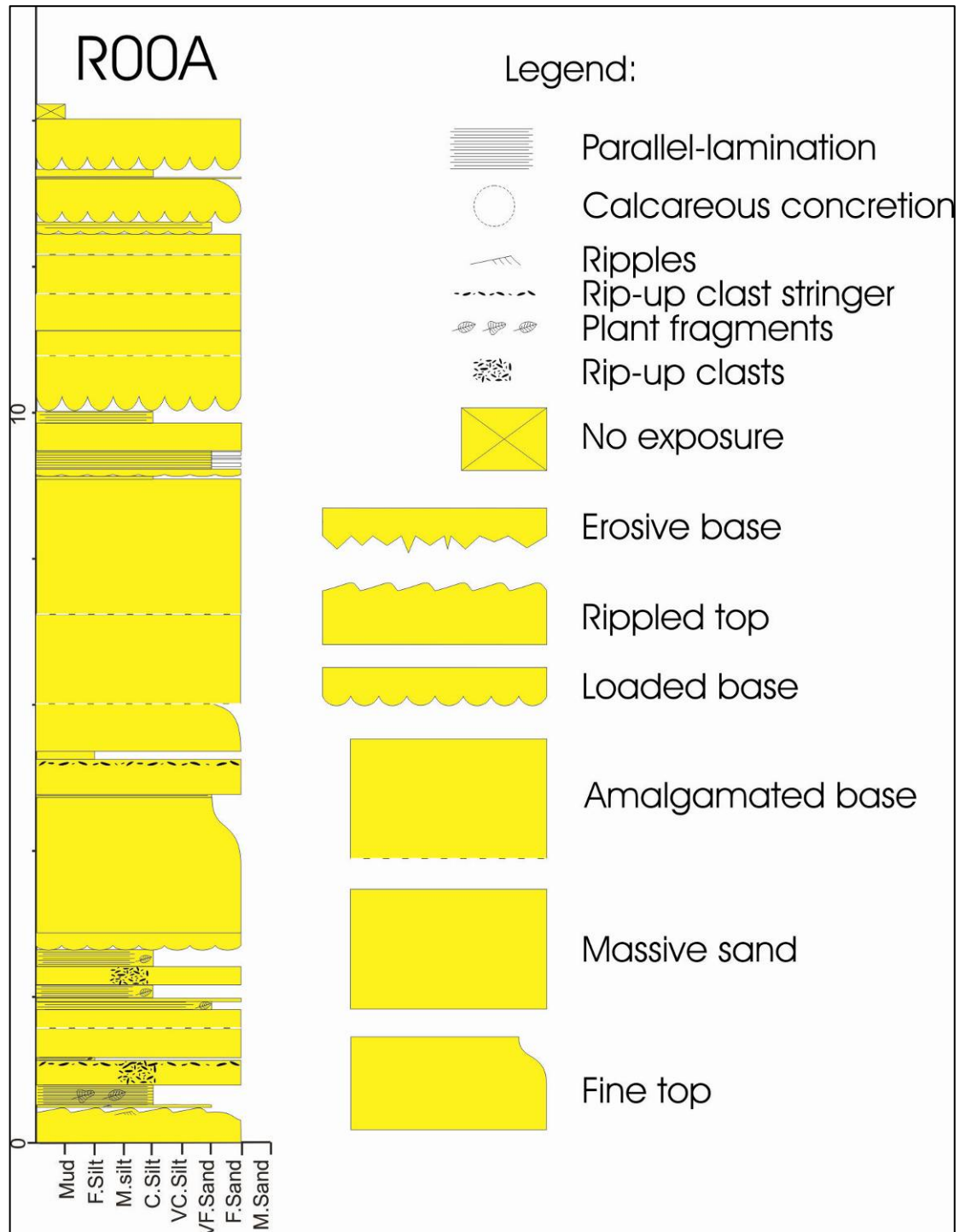


Figure 78: Profile R00A (34H0399360/UTM6373789) compiled in CorelDraw showing lithofacies and measured sedimentological features and a legend that includes all features that were used when creating the CorelDraw profiles.



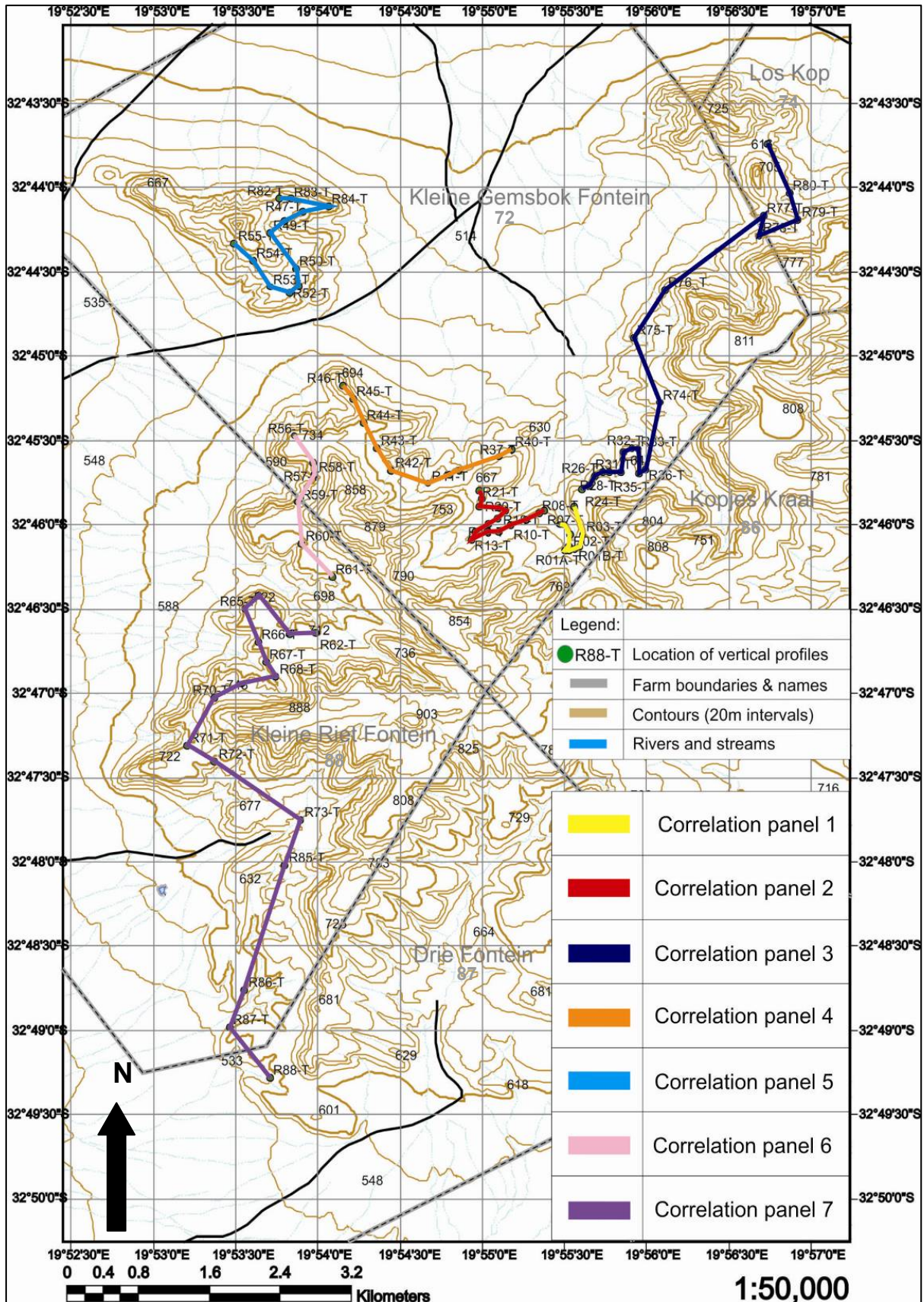


Figure 81: ArcView map of study area showing location of correlation panels 1 – 7.



Avulsion of distributive channels up-dip of the study area towards the north-west can also have an influence on the stacking of lobes and lobe elements (Prélat *et al.*, in review).

Lobe-element 1 (indicated in yellow) is the lowermost and oldest of the lobe elements. It pinches out first, both to the north-east on the farm Los Kop 74 (Figure 92, Image A), and the south-southwest on the farm Drie Fontein 87 (Figure 92, Image B). The base of lobe-element 1 is often obscured by scree, making it difficult to trace out in outcrop. Lobe-element 2 (indicated in orange) is stacked on top of lobe-element 1, but is slightly offset to the east. It pinches out between 200 and 400 metres further east than lobe-element 1. Lobe-element 3 (indicated in red) is stacked on top of lobe-element 2 and is also offset to the east. It pinches out approximately 300 metres further east than lobe-element 2.

Vertical profiles were not measured in the areas represented by Figure 92 as the lobe elements were commonly only visible in outline, if at all. The thickness of the lobe elements rarely exceeds half a metre, and they are generally obscured by scree or are highly weathered.

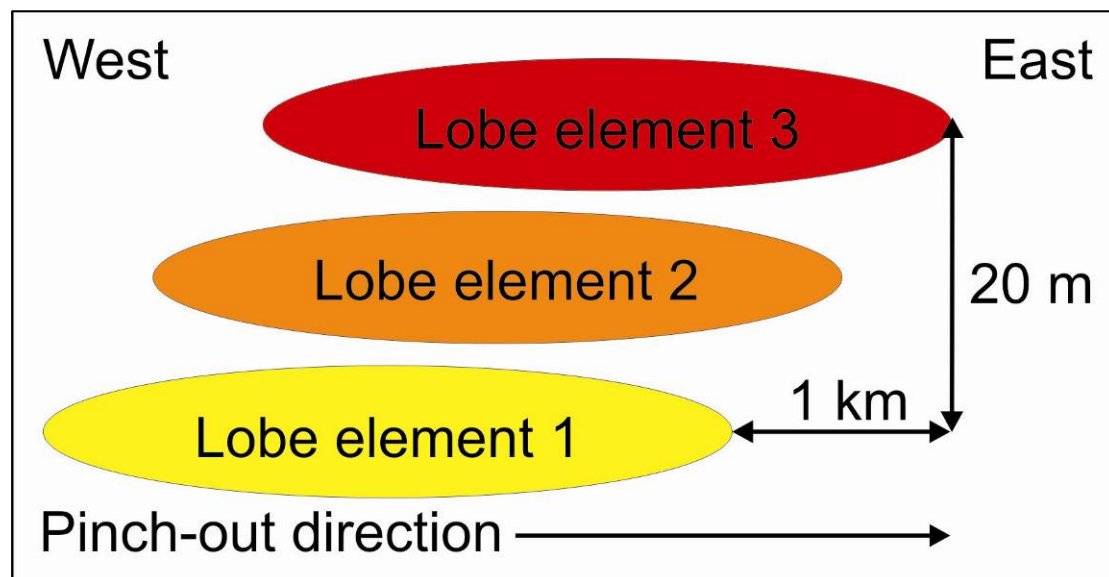


Figure 90: Stacking of sandstone-lobe elements 1, 2 and 3 in relation to each other.

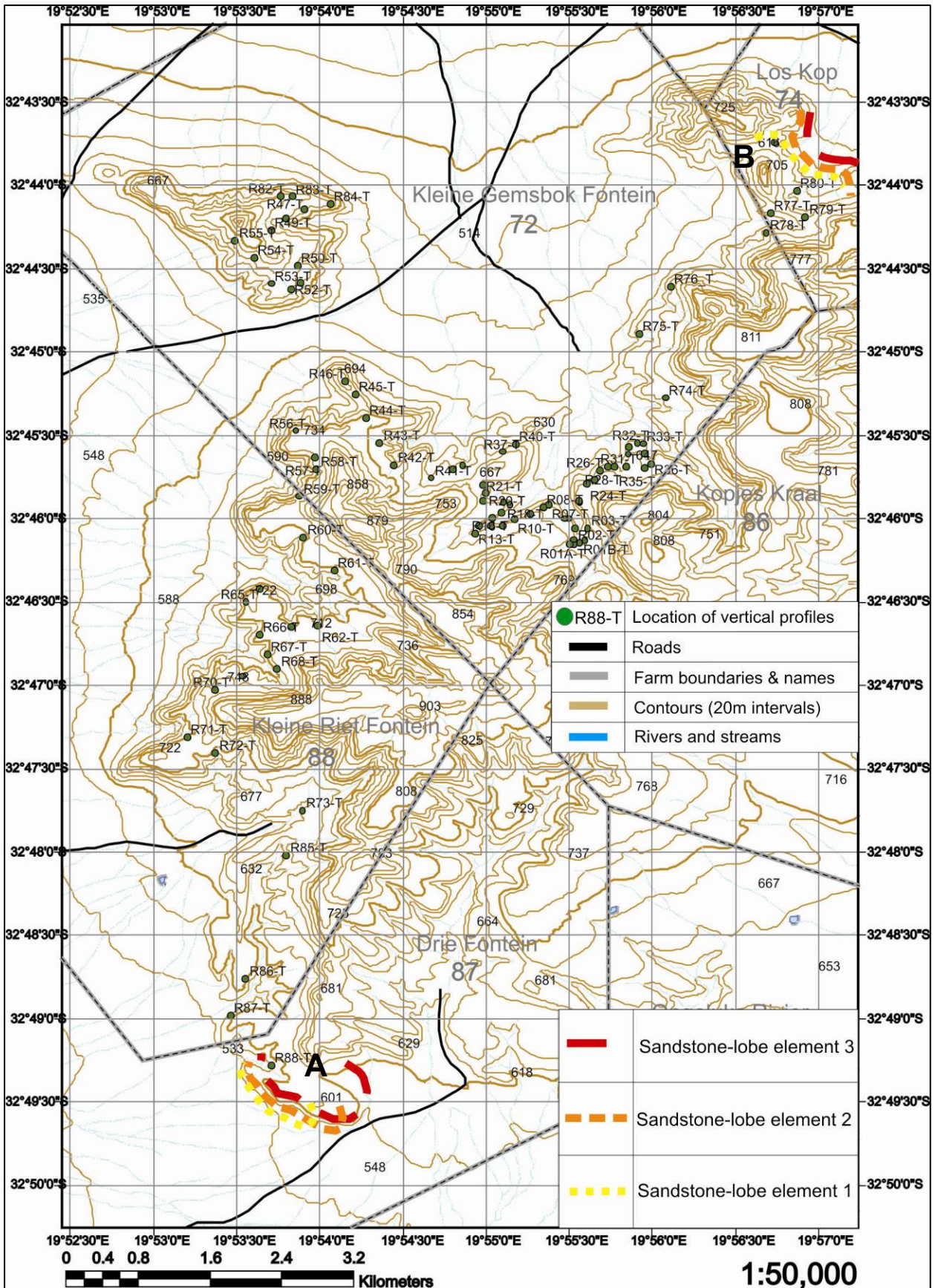


Figure 91: ArcView map showing the location of the up-dip (A) and down-dip (B) pinch out of lobe-element 1 (yellow), 2 (orange) and 3 (red) in relation to the study area.



highstand systems tracts to high-frequency sequences” (Johnson *et al.*, 2001, p. 1007). In the study area, the change from an underlying Type 2 horizon to overlying sandstone is interpreted as a sequence boundary (SB).

However, a different interpretation invokes autocyclic control of deposition as a result of intrabasinal aspects such as channel meander, avulsion, and the underlying topography during deposition. According to this interpretation, the fine-grained deposition between lobes represents the lateral fringes of extra lobes that lie to the east or west of the studied outcrop, with avulsion of these lobes occurring at a scale of more than 10 km (Prélat *et al.*, in review).

The siltstone inter-lobe elements are found between the sandstone-lobe elements. They can be described as Type 3 condensed intervals that represent thin-bedded, commonly amalgamated siltstones with a thickness of less than 30 centimetres. They are found throughout the outcrop area and are interpreted to represent allocyclic switching within the fans that is caused by “very high-frequency, parasequence-scale, shelf-flooding events” (Johnson *et al.*, 2001, p. 1007). The application of sequence stratigraphy to Middle Fan 2 can be seen in Figure 93.

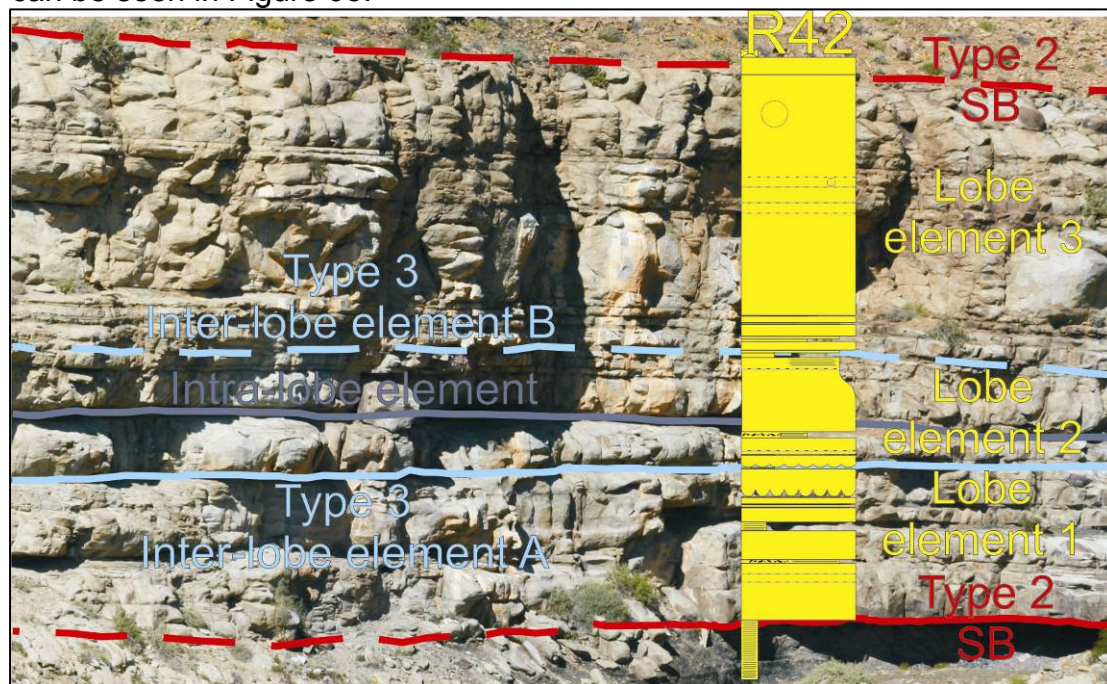


Figure 93: Photomontage of profile R42 (34H0397661/UTM6374647) illustrating the position of Type 2 horizons (sequence boundaries, in red), Type 3 horizons (siltstone inter-lobe elements, in light blue), lobe elements 1, 2 and 3 (in yellow, separated by the Type 3 boundaries) and a prominent siltstone intra-lobe element (in dark blue).



### 6.3. Groove casts

Groove casts (Figure 24 & Figure 94) are also common on the bases of turbidite beds. They are ridges created when a furrow, formed by an object being dragged across unconsolidated mud by a turbidity current, is filled up when a layer of sand is deposited in the furrow. They are also used as palaeocurrent indicators, but only indicate the orientation of the flow (Boggs, 2006), and are thus ambiguous, as the flow is from one of two opposing directions. The measured palaeocurrent direction was selected to coincide with the overall palaeocurrent direction determined by Rozman (2000).



Figure 94: Groove casts at the base of a massive sandstone bed (R34, 34H0400014/UTM6374796, Klein Gemsbok Fontein).

### 6.4. Ripple cross-lamination (“Rib and furrow”)

The ripple cross-lamination in the sand- and siltstones resulted from migrating linguoid ripples with amplitude of no more than 5 centimetres. The ripples form parallel to the general direction of flow of the water mass due to traction of the sand grains and development of foreset beds (Allen, 1966; Pettijohn *et al.*, 1987) (Figure 95), and they are thus formed by unimodal currents.



**Figure 95: Ripple cross-lamination seen from above (arrow) (near vertical profile R01B, 34H0399413/UTM6373810, Klein Gemsbok Fontein).**

## Results

Rose diagrams were compiled for Middle Fan 2, incorporating all the measurements taken in the study area (Figure 96), and separately for each of the lobe and inter-lobe elements (Figure 97). The diagrams were created using the computer program EZ-ROSE, Version 1.0 created by J.H. Baas of the Department of Earth Sciences, University of Leeds (Baas, 2000). No mean vector calculations were undertaken for the palaeocurrent orientations.

The general trend for Middle Fan 2 is to the north north-east, with a second smaller peak to the north. In the individually-generated rose diagrams, lobe elements 2 and 3 have a general trend to the north-east, and lobe-element 1 to the north-northeast. However, some variation can be seen between 0 and 90 degrees.

Few palaeocurrent measurements were taken for inter-lobe elements A and B, as the siltstones are mostly badly weathered, making it difficult to take accurate readings.

the relatively low-energy origins of the deposits in the study area. The higher the available energy, the more channelised areas would be created.

A variation on the first depositional model was created using a facies map developed from Fan 3 (Figure 99, Strat Group, 2008). This lithofacies model (Figure 100) defines the axis, off-axis and fringe zones. These zones are comparable to the channel, amalgamated sheet and sheet zones defined for the first depositional model (Figure 98), and zones depicting the debrite-prone fringe were also added.

The finger-like shapes of the facies map (Figure 99) and the Fan 2 depositional model (Figure 98) shows great similarity, although the measured outcrop data are less symmetrical than those of the theoretical model. Unlike the cartoon, the depositional model does not include a distal fringe, as the pinch-out ends abruptly with fringe deposits. The debrite-prone fringe seen in the depositional model also originates out of the axis deposits, instead of the off-axis deposits as represented by the cartoon.

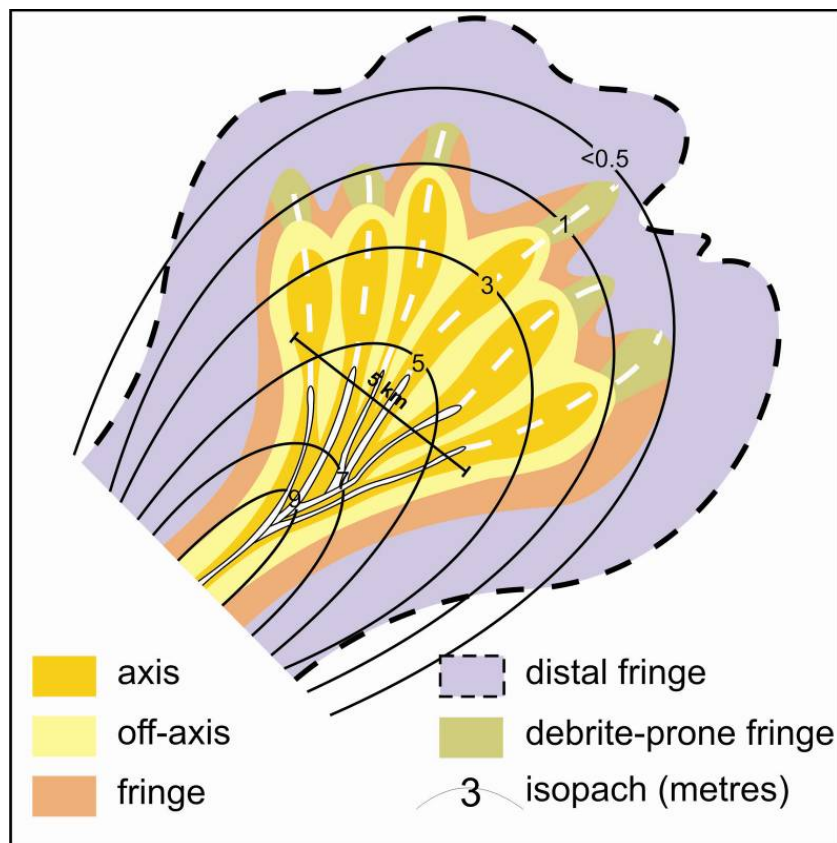


**Figure 99: Facies distributions in a lobe developed from observations in Fan 3 (Strat Group, 2008).**



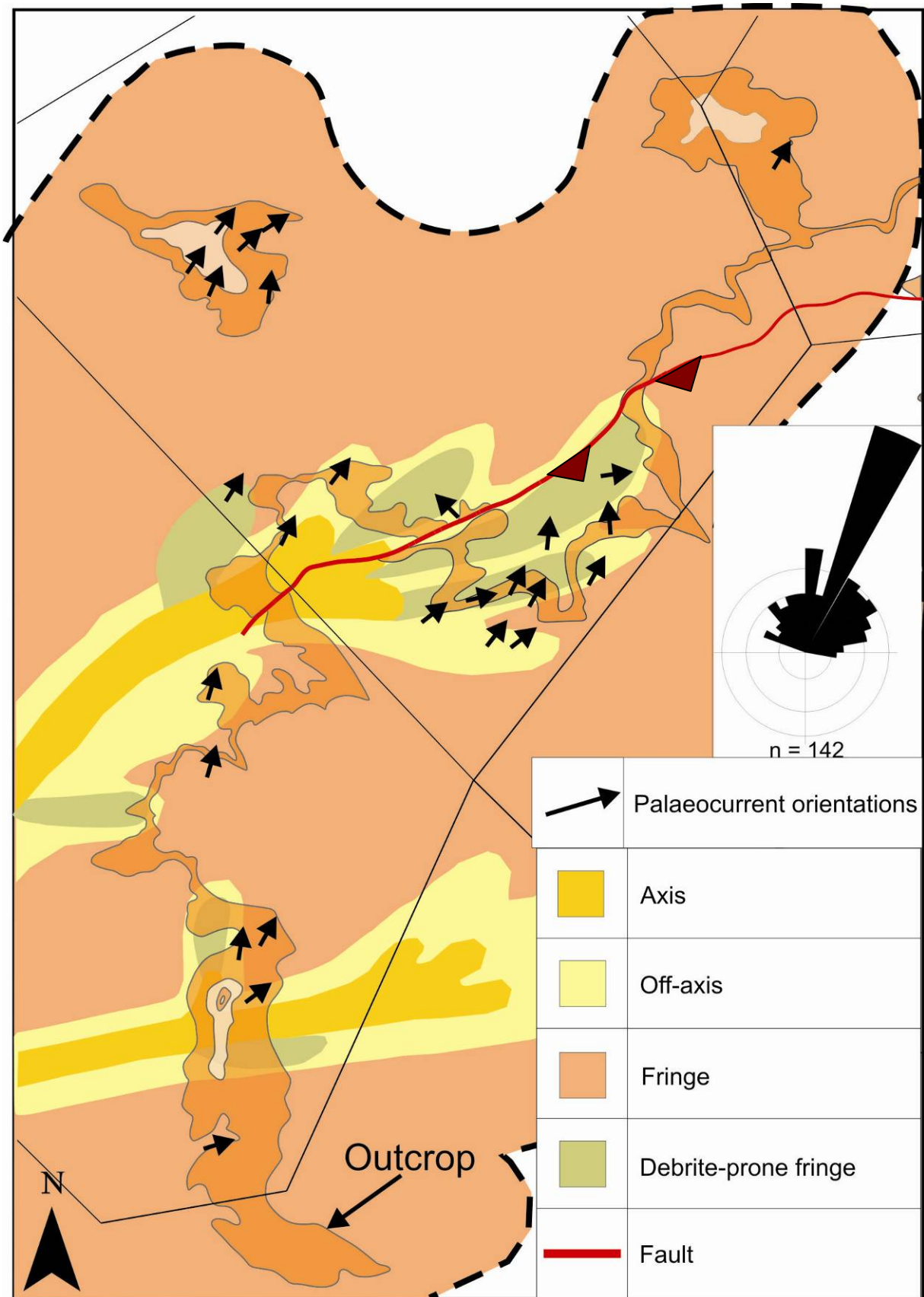


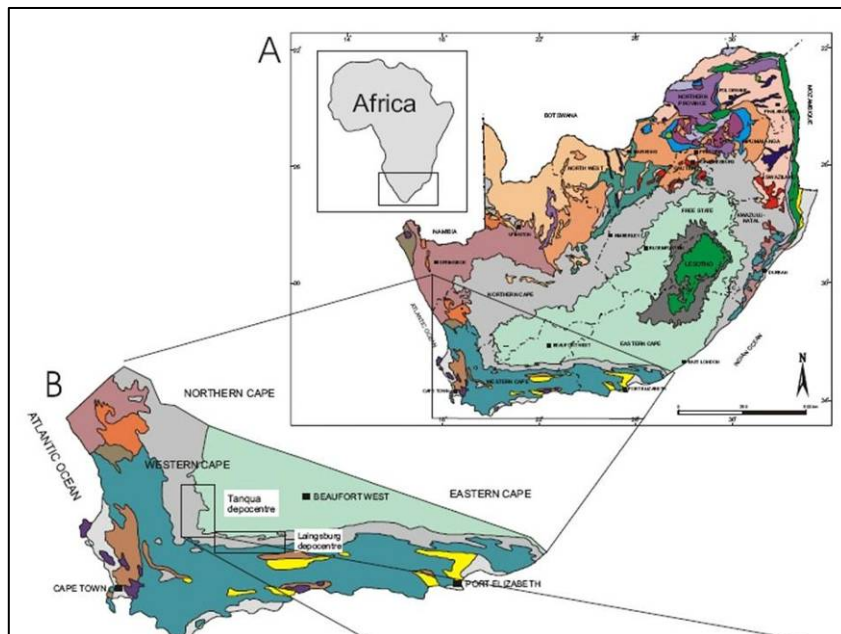
Figure 100: Depositional model illustrating axis and fringe zones of Middle Fan 2.

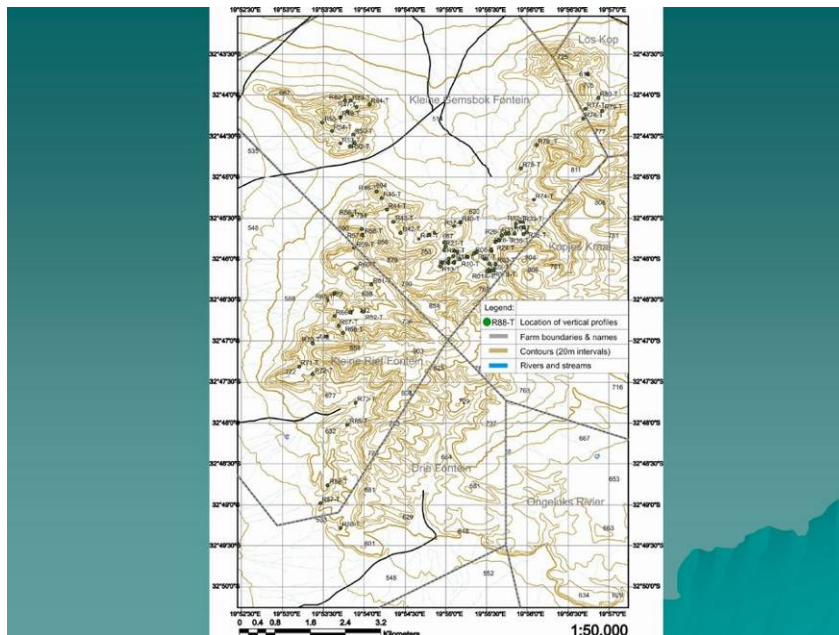
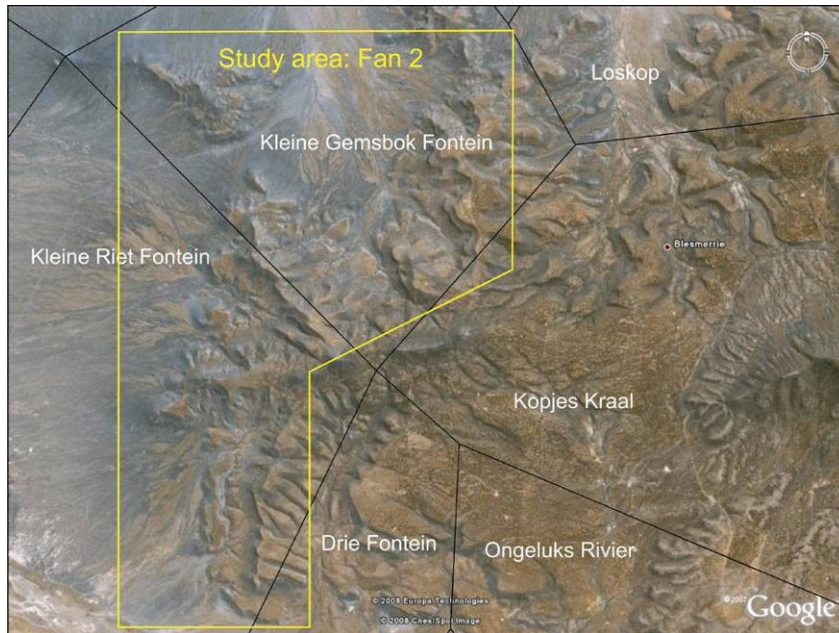
## Appendix B

PowerPoint presentation given at PetroSA on 18 June 2008.

# Modelling the architecture of distal sand-rich lobe deposits: an example from Fan 2, Skoorsteenberg Formation, Tanqua Karoo, South Africa

Rochelle Steyn



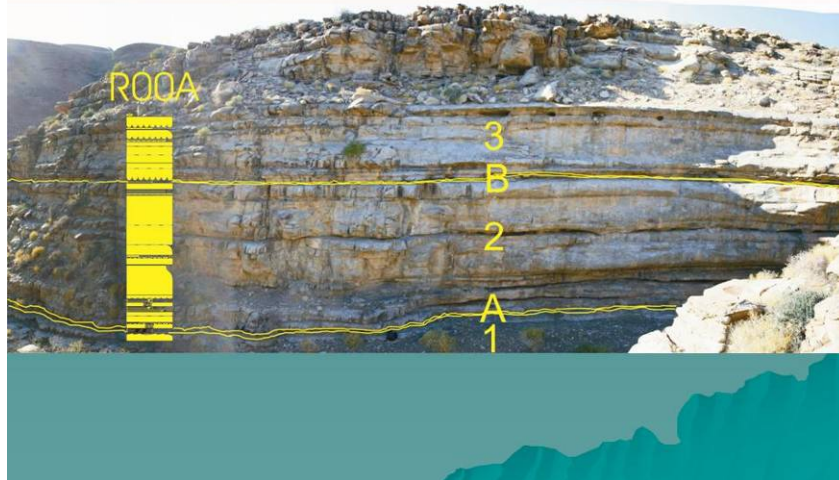


## Aims

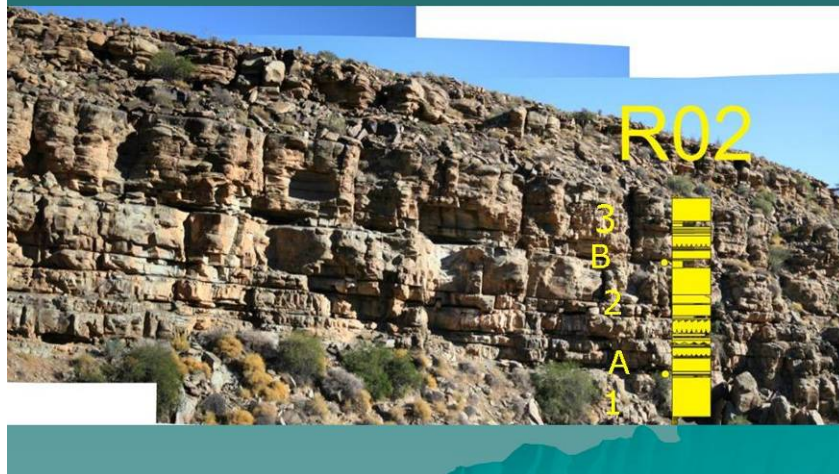
- ◆ Detailed vertical profiling in Middle Fan 2
- ◆ Detailed breakdown of lobe elements in Middle Fan 2
- ◆ Facies associations between distal turbidity current deposits and lateral pinchouts
- ◆ Dimensions of linked debrites
- ◆ Petrel data manipulation



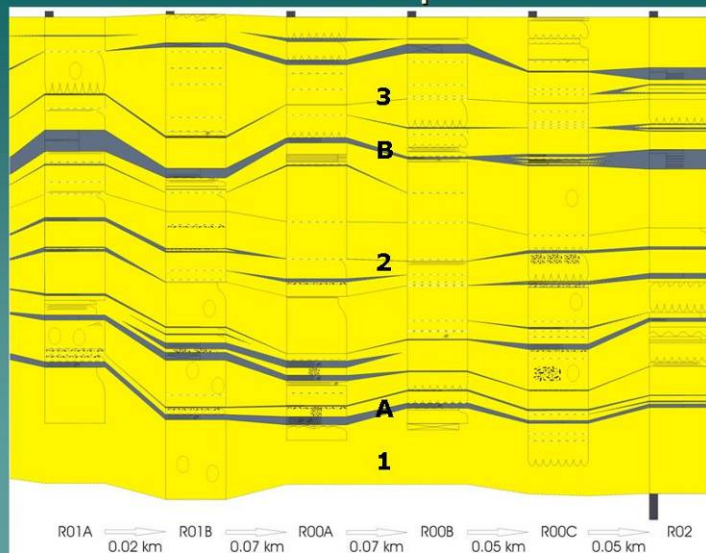
## Outcrop and lobe elements: R00A



## R02



## Correlation panels

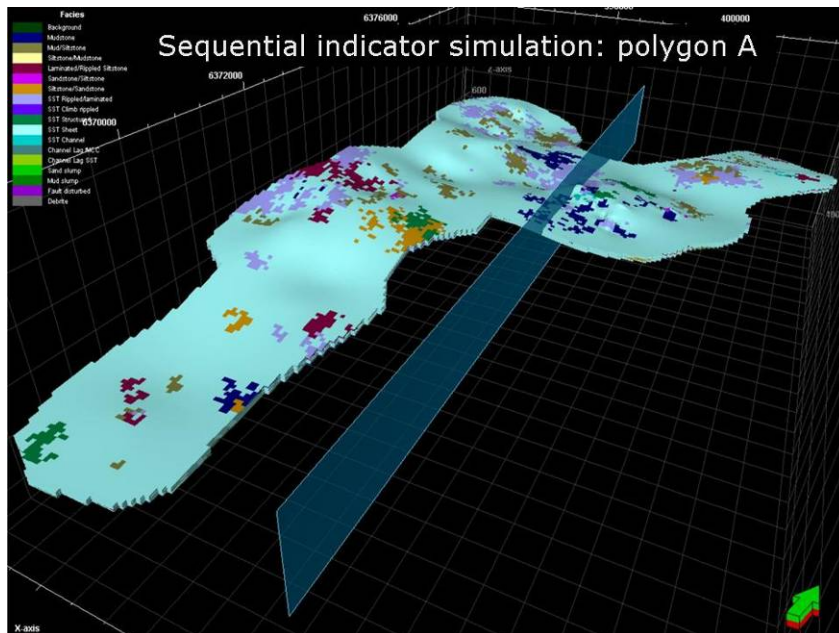
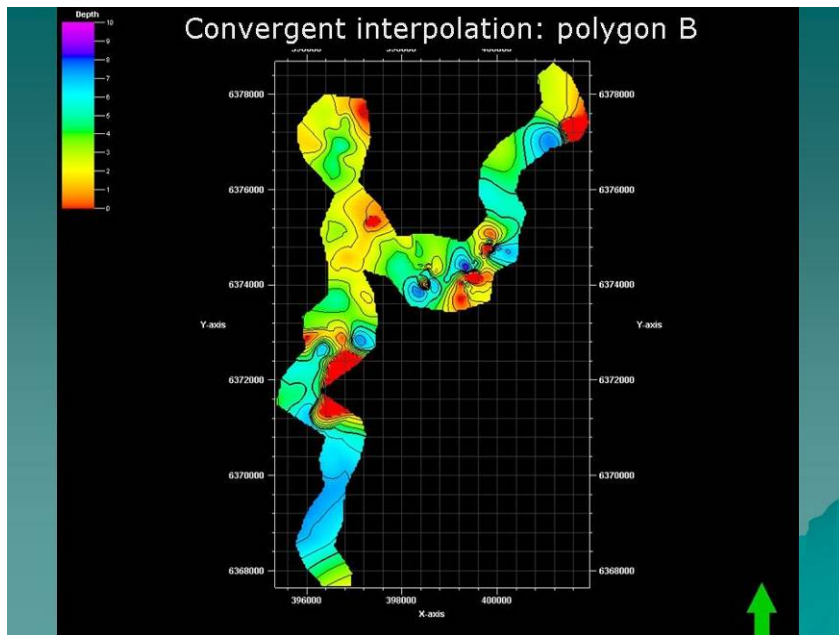
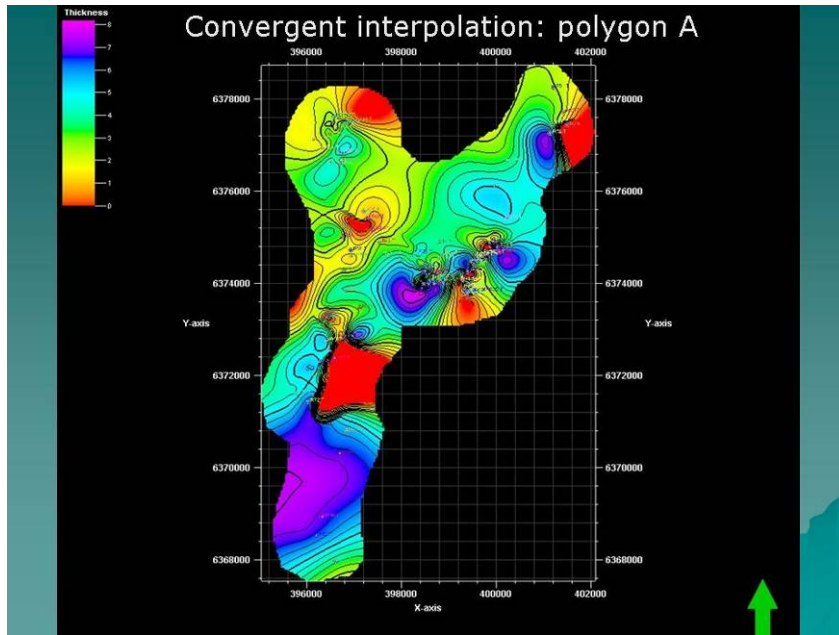


Chapter 3	Chapter 7.3.1	Chapter 7.3.6
Lithofacies description	DSL facies	Petrel facies associations
1) Massive sandstone	1) Structureless sandstone	1) Structureless sandstone
2) Ripple cross- and parallel-laminated sandstone	2) Structured sandstone	2) Structured sandstone
3) Siltstone	3) Sandstone - ripples/planar lamination	3) Siltstone
4) Ripple cross- and parallel-laminated siltstone	4) Siltstone/sandstone (>50% silt)	
5) Organic-rich debrite	5) Sandstone/siltstone (>50% sand)	4) Other
6) Claystone	6) Laminated/rippled siltstone	
	7) Debrite (dominant sandstone with organics)	5) Background
	8) Mudstone	
	9) Mudstone/siltstone (>50% mud)	

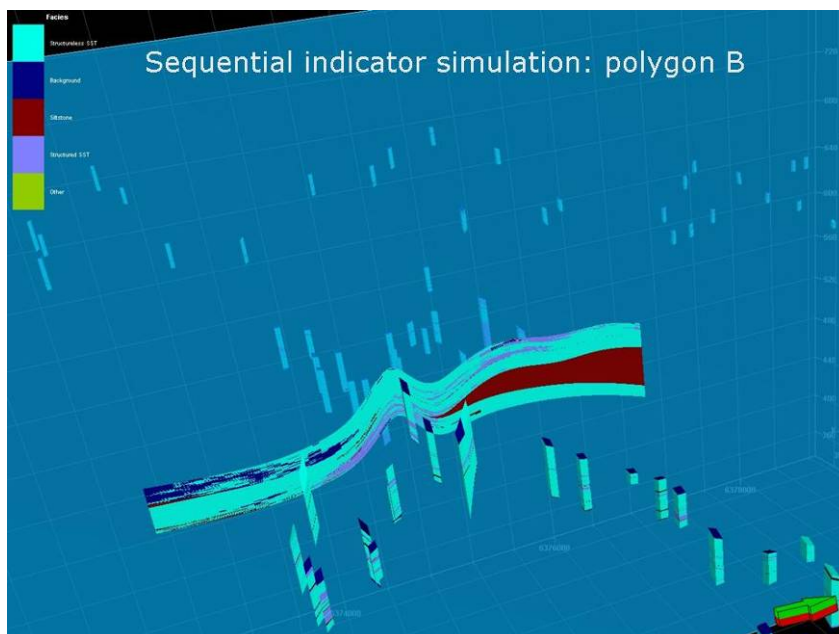
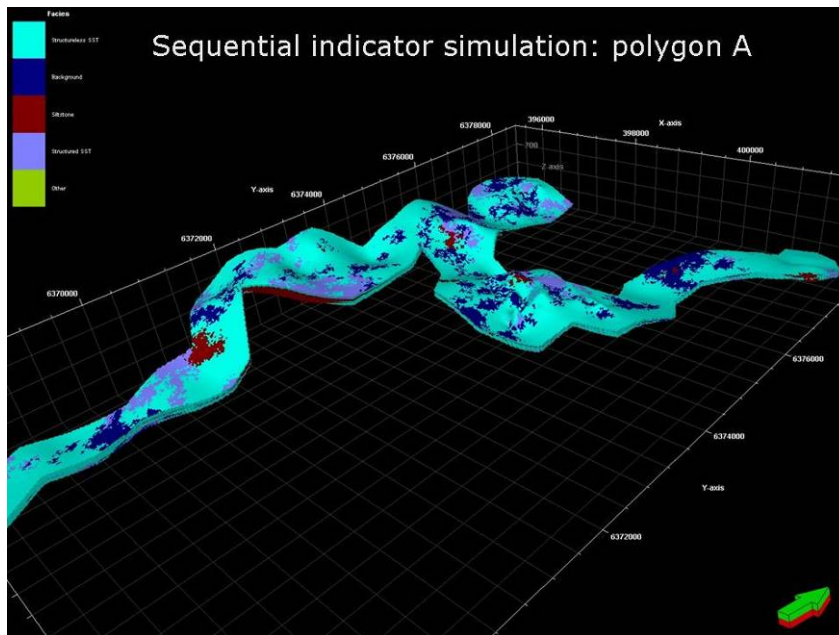
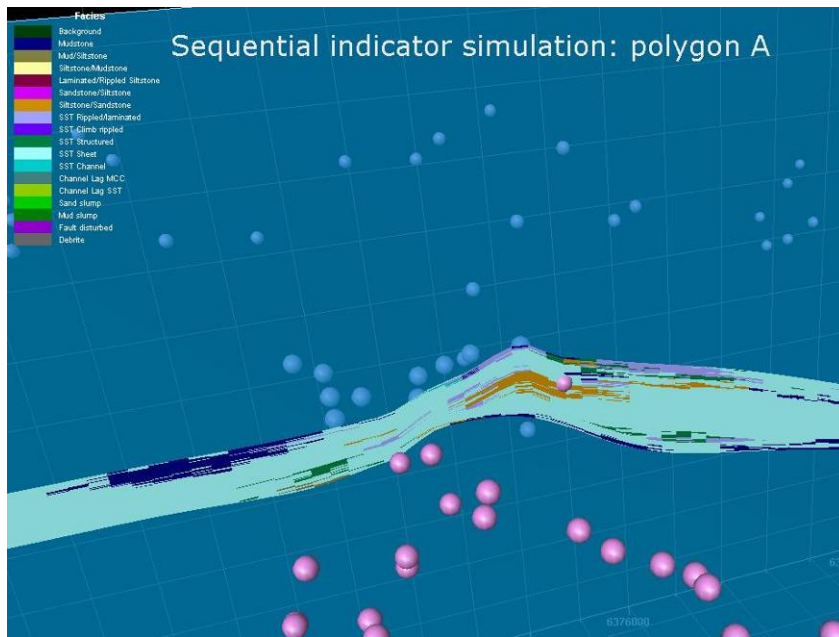
Surfaces	X	Y	Z	
Top 3	-32.7692	19.92548	649	Rochelle Steyn: Top measured GPS coordinates
	0.7			
	0.1			
	0.02			
	0.6			
	0.17			
	0.28			
	0.53			
	0.5			
	0.34			
Base 3/Top B	0.76			
	0.15			
Base B/Top 2	0.38			
	0.25			
	0.1			
	0.4			
	1.85			
	1.22			
	0.65			
	0.11			
	0.48			
	0.05			
	1.85			
	0.24			
	0.23			
	0.25			
	0.17			
	0.05			
	0.11			
	0.25			
	0.4			
Base 2/Top A	0.04			
	0.34	9.42	635.43	Rochelle Steyn: Calculated GPS Z coordinate for surface Base 2/Top A
	0.15	0.27	635.16	Rochelle Steyn: Bottom calculated GPS coordinate
Base A/Top 1	0.04			
	0.47	0.51	634.65	
Base 1				

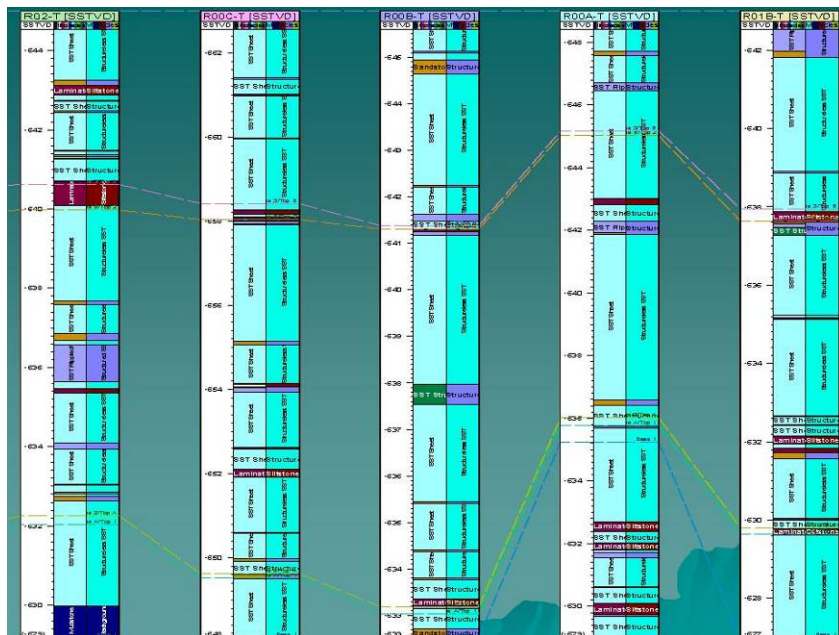
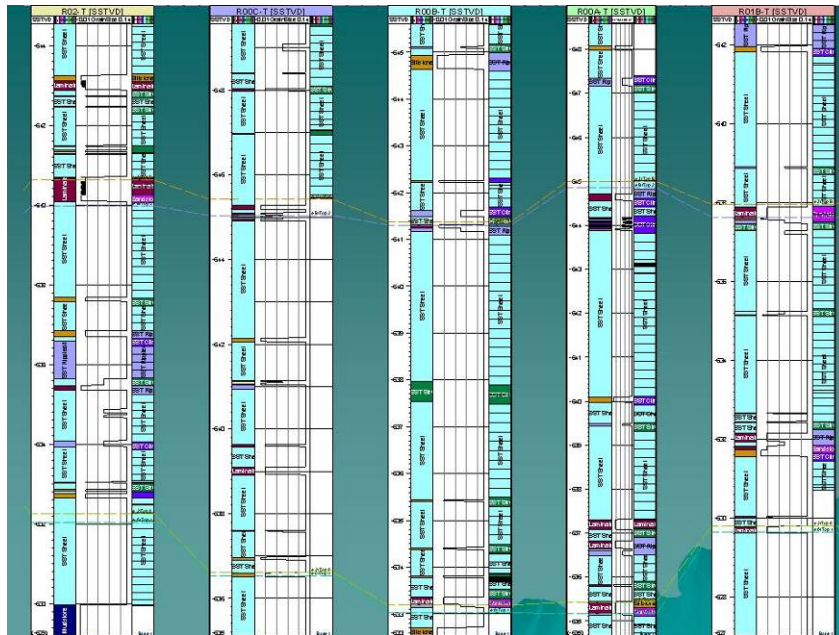
	X	Y	Z	Z - Thickness	Base 3/Top B	Thickness	Z - Thickness	Base B/Top 2	Thickness	Z - Thickness	Base 2/Top A	Thickness
R00A-T	399360	6373789	649	645	Base 3/Top B	4	644.85	Base B/Top 2	0.15	635.43	Base 2/Top A	9.42
R00B-T	399319	6373788	644	641.38	Base 3/Top B	4.62	641.31	Base B/Top 2	0.07	633.19	Base 2/Top A	8.12
R00C-T	399356	6373839	603	658.42	Base 3/Top B	4.58	658.04	Base B/Top 2	0.38	649.62	Base 2/Top A	8.42
R01A-T	399461	6373834	641	637.26	Base 3/Top B	3.74	636.55	Base B/Top 2	0.71	629.59	Base 2/Top A	6.96
R01B-T	399413	6373810	649	637.95	Base 3/Top B	5.05	637.63	Base B/Top 2	0.32	629.81	Base 2/Top A	7.82
R02-T	399363	6373957	646	640.62	Base 3/Top B	4.38	639.97	Base B/Top 2	0.85	632.26	Base 2/Top A	7.71
R03-T	399485	6373960	646	639.68	Base 3/Top B	5.32	639.21	Base B/Top 2	0.47	636.11	Base 2/Top A	3.1
R04-T	399406	6374250	625	659.16	Base 3/Top B	5.84	658.56	Base B/Top 2	0.6	655.23	Base 2/Top A	3.33
R05A-T	399305	6374070	656	651.69	Base 3/Top B	4.31	651.16	Base B/Top 2	0.53	643.33	Base 2/Top A	7.83
R05B-T	399363	6374071	649	643.78	Base 3/Top B	5.22	643.7	Base B/Top 2	0.08	637.98	Base 2/Top A	5.72
R06-T	399398	6374267	671	665.18	Base 3/Top B	5.82	665.16	Base B/Top 2	0.02	661.01	Base 2/Top A	4.15
R07-T	399120	6374219	656	649.38	Base 3/Top B	6.62	649.2	Base B/Top 2	0.18	644.24	Base 2/Top A	4.96
R08-T	399071	6374194	668	661.56	Base 3/Top B	6.44	661.52	Base B/Top 2	0.04	657.07	Base 2/Top A	4.45
R09-T	398945	6374123	668	653.4	Base 3/Top B	6.6	653.34	Base B/Top 2	0.06	650.24	Base 2/Top A	3.1
R10-T	398799	6374055	663	656.84	Base 3/Top B	6.16	656.77	Base B/Top 2	0.07	653.88	Base 2/Top A	2.89
R11-T	398687	6373980	669	658.66	Base 3/Top B	6.34	658.58	Base B/Top 2	0.08	655.79	Base 2/Top A	2.79
R12-T	398577	6373981	667	661.53	Base 3/Top B	5.47	661.49	Base B/Top 2	0.04	658.51	Base 2/Top A	2.98
R13-T	398427	6373891	675	669.51	Base 3/Top B	5.49	669.47	Base B/Top 2	0.04	665.68	Base 2/Top A	3.79
R14-T	398468	6373977	673	667.695	Base 3/Top B	5.305	667.675	Base B/Top 2	0.02	662.395	Base 2/Top A	5.28
R15-T	398597	6374072	666	660.26	Base 3/Top B	5.74	660.22	Base B/Top 2	0.04	657.04	Base 2/Top A	3.18
R16-T	398670	6374131	658	651.32	Base 3/Top B	6.88	651.28	Base B/Top 2	0.04	648.43	Base 2/Top A	2.85
R17-T	398755	6374221	665	662.53	Base 3/Top B	4.47	662.49	Base B/Top 2	0.04	660	Base 2/Top A	2.49
R18-T	398892	6374249	663	658.48	Base 3/Top B	3.52	658.36	Base B/Top 2	0.12	655.79	Base 2/Top A	2.57
R19-T	398497	6374265	666	660.74	Base 3/Top B	5.26	660.69	Base B/Top 2	0.05	656.82	Base 2/Top A	3.87
R20-T	398521	6374348	668	664.6	Base 3/Top B	4.4	664.56	Base B/Top 2	0.04	659.79	Base 2/Top A	4.77
R21-T	398500	6374440	678	665.28	Base 3/Top B	4.72	665.21	Base B/Top 2	0.07	661.24	Base 2/Top A	3.97
R22-T	398780	6374535	688	675.26	Base 3/Top B	4.74	675.16	Base B/Top 2	0.1	671.23	Base 2/Top A	3.93
R23-T	398846	6374635	668	664.49	Base 3/Top B	4.51	664.43	Base B/Top 2	0.06	660.34	Base 2/Top A	4.09
R24-T	399472	6374454	668	654.61	Base 3/Top B	5.39	654.49	Base B/Top 2	0.12	650.15	Base 2/Top A	4.34
R25-T	399547	6374507	657	652.28	Base 3/Top B	4.72	651.99	Base B/Top 2	0.29	647.54	Base 2/Top A	4.45
R26-T	399593	6374607	653	647.87	Base 3/Top B	5.13	647.79	Base B/Top 2	0.08	643.99	Base 2/Top A	3.8
R27-T	399666	6374653	651	648.8	Base 3/Top B	4.2	648.52	Base B/Top 2	0.28	644.45	Base 2/Top A	4.07











## Conclusions

- ◆ Iterative process
- ◆ Official Petrel training needed
- ◆ Data not suitable?
- ◆ Hand-in: 1 September 2008
- ◆ Questions?
- ◆ Thank you

## Appendix C

Isopach maps using the Kriging algorithm and convergent interpolation with polygon A (A and B on Figure 101 to Figure 105) and convergent interpolation with polygon B (C and D on Figure 101 to Figure 105).

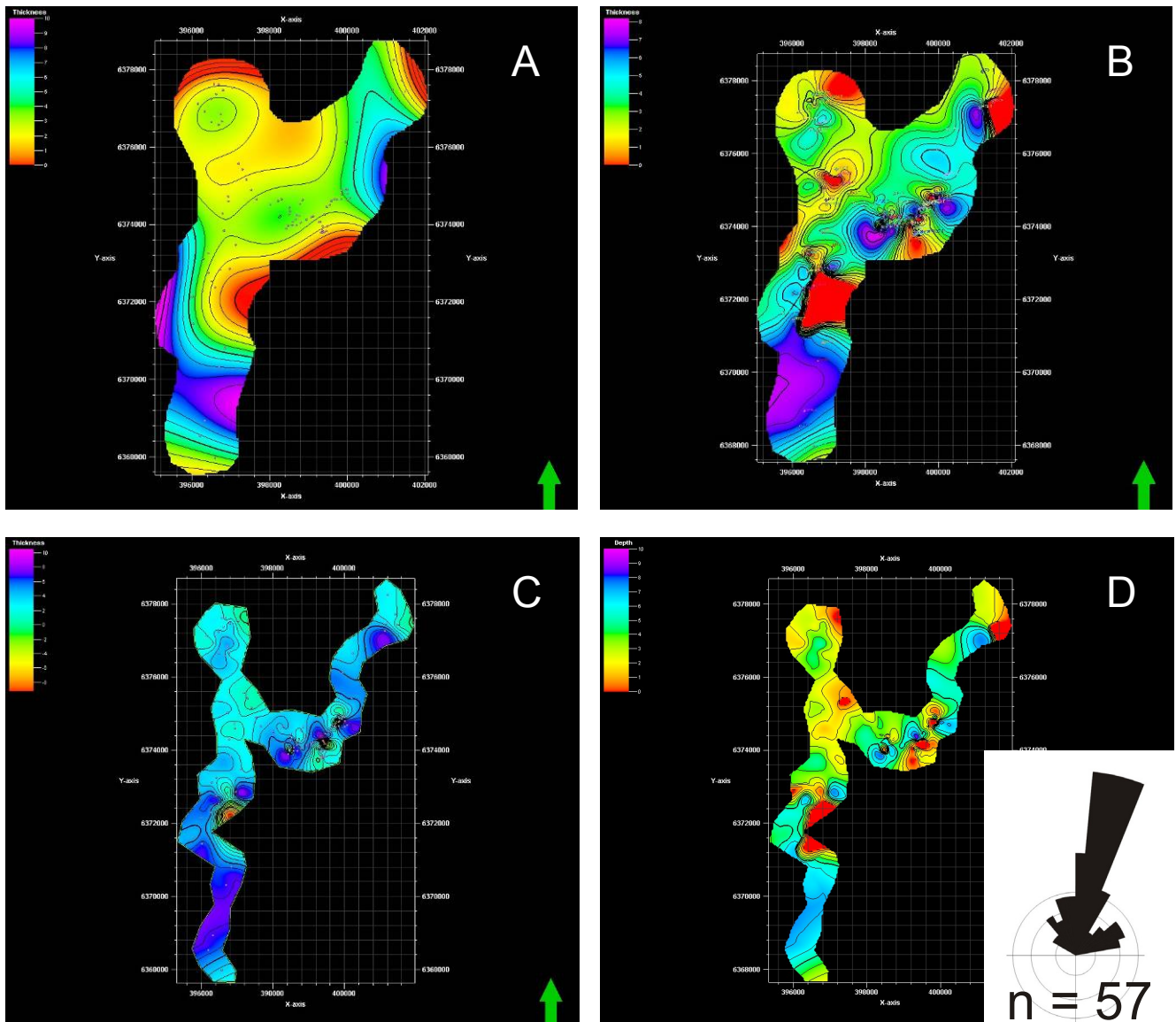
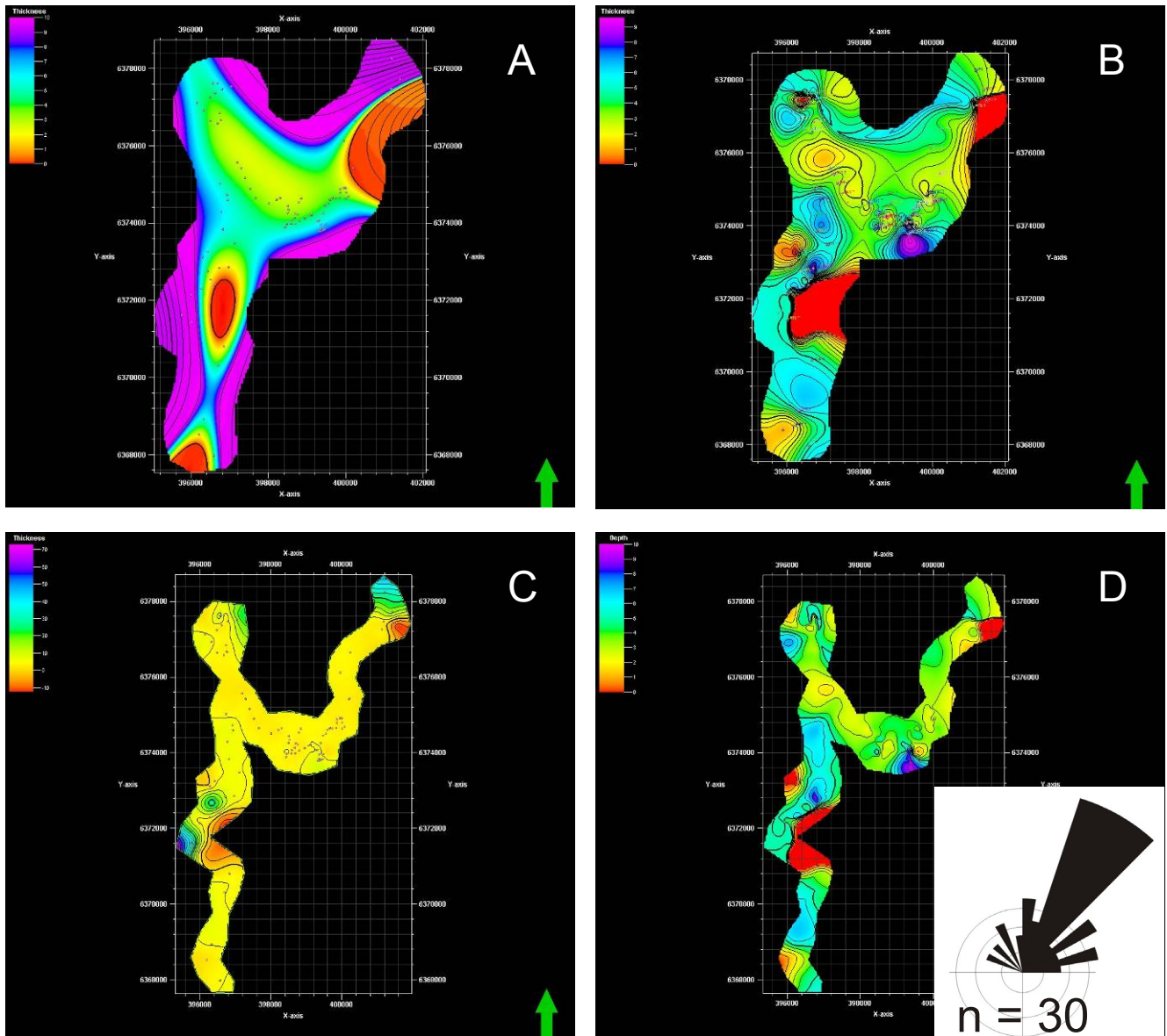


Figure 101: Isopach maps for sandstone-lobe element 1 using Kriging interpolation (A) and convergent interpolation (B) with polygon A, convergent interpolation with polygon B at a range of 50 metres (C), and convergent interpolation with polygon B at a range of 5 metres (D).





**Figure 102: Isopach maps for sandstone-lobe element 2 using Kriging interpolation (A) and convergent interpolation (B) with polygon A, convergent interpolation with polygon B at a range of 50 metres (C), and convergent interpolation with polygon B at a range of 5 metres (D).**

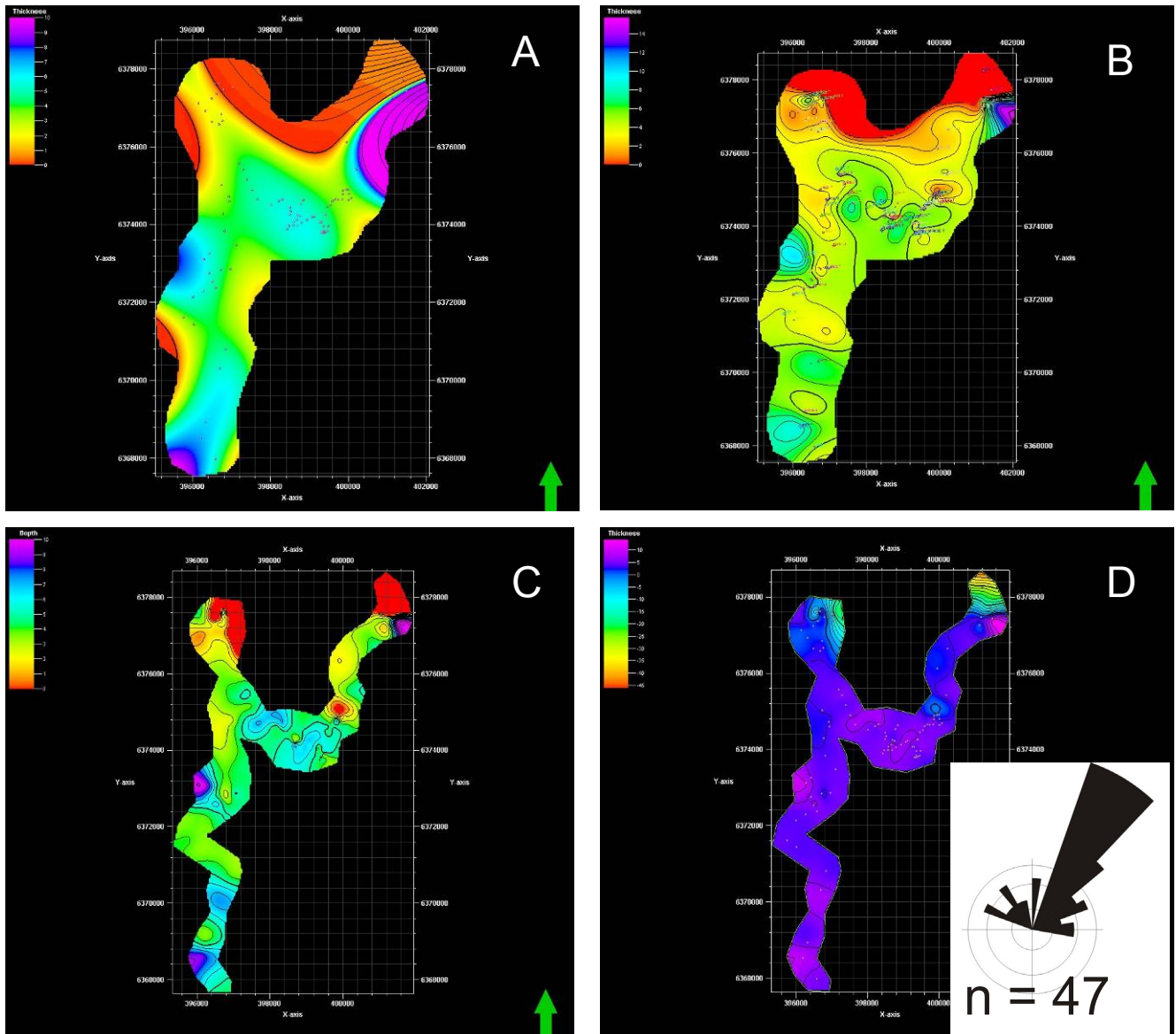
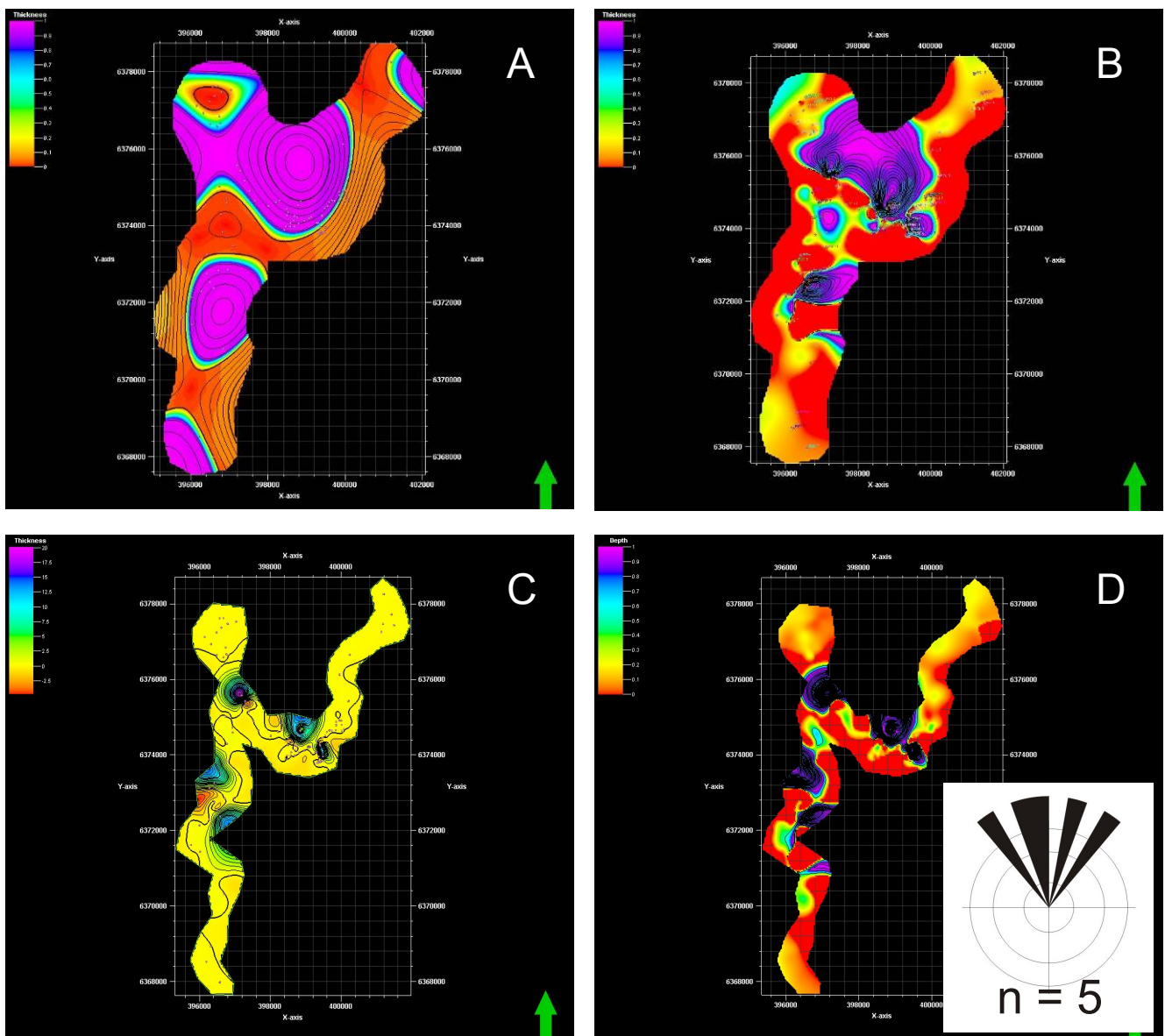


Figure 103: Isopach maps for sandstone-lobe element 3 using Kriging interpolation (A) and convergent interpolation (B) with polygon A, convergent interpolation with polygon B at a range of 50 metres (C), and convergent interpolation with polygon B at a range of 5 metres (D).



**Figure 104: Isopach maps for siltstone intra-lobe element A using Kriging interpolation (A) and convergent interpolation (B) with polygon A, and convergent interpolation with polygon B at a range of 50 metres (C), and convergent interpolation with polygon B at a range of 5 metres (D).**



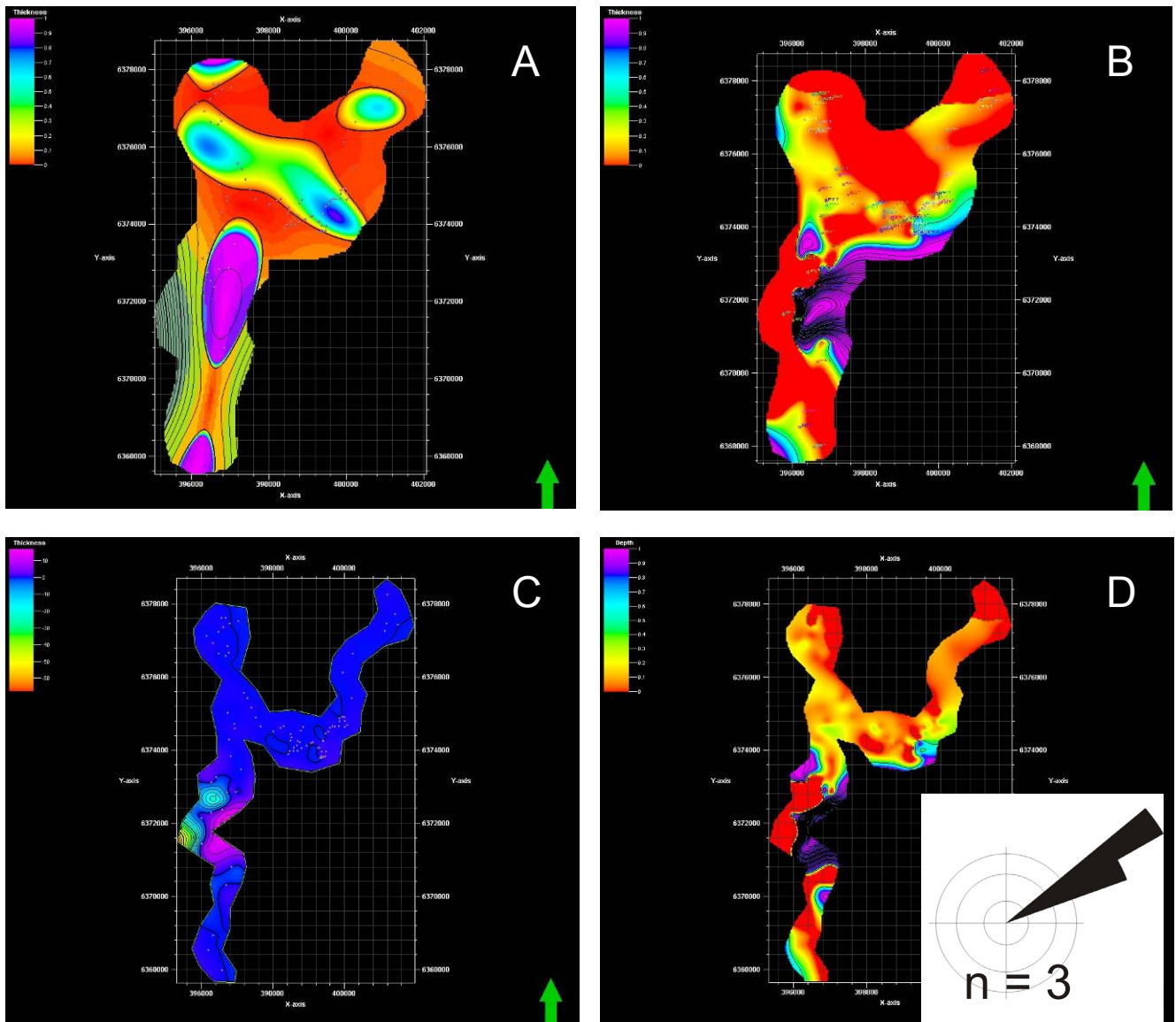


Figure 105: Isopach maps for siltstone intra-lobe element B using Kriging interpolation (A) and convergent interpolation (B) with polygon A, convergent interpolation with polygon B at a range of 50 metres (C), and convergent interpolation with polygon B at a range of 5 metres (D).